TURKGEO

TURKISH JOURNAL OF GEOSCIENCES

e-ISSN 2717-7696

OPEN ACCESS

dergipark.org.tr/tr/pub/turkgeo
turkgeosciences@gmail.com

TURKGEO, June/2022
Volume: 3 - Issue: 1

TURKGEO
TURKISH JOURNAL OF GEOSCIENCES

About The Journal

Turkish Journal of Geosciences is a multi-disciplinary open-access journal aimed to publish peer-reviewed original research and review articles covering all aspects of geosciences. The journal includes a wide scope of information on scientific and technical advances in all areas related to geosciences and indexed in international indices and databases that publish studies on earth sciences.

Aim and Scope

TURKGEO Journal has the following aim and scopes;

Aim of TURKGEO

- TURKGEO aims to promote the theory and practice from the integration of instruments, methodologies, and technologies and their respective uses in the environmental and other natural sciences.
- TURKGEO aims to provide a widely accessible discussion environment that will strengthen and accelerate the exchange of knowledge and experience among scientists, researchers, engineers and other implementers involved in the subject directly or indirectly.

Scope of TURKGEO

- Earth and Environmental Sciences Applications
- Geographic Information Systems
- Remote Sensing
- Photogrammetry
- Geostatistics
- GPS/GNSS
- RADAR/SAR/LIDAR and Laser Scanning
- Spatial Data Infrastructure
- Spatial Decision Support Systems
- Climate Change
- Geology
- Geomorphology
- Hydrogeology
- Geophysics
- Hydrology and Water Resources
- Oceanography

Publishing Frequency 2 issues per year (June-December)

ISSN 2717-7696

WEB https://dergipark.org.tr/tr/pub/turkgeo

Contact sefa.bilgilioglu@gmail.com / osmanorhan44@gmail.com

TURKGEO
TURKISH JOURNAL OF GEOSCIENCES

EDITOR

Assist. Prof. Dr. Süleyman Sefa BİLGİLİOĞLU
Aksaray University, Faculty of Engineering, Department of Geomatics Engineering /Aksaray/Turkey

ASSOCIATE EDITOR

Assist. Prof. Dr. Osman ORHAN
Mersin University, Institute of Science, Remote Sensing and GIS /Mersin /Turkey

Dr. Cemil GEZGİN
Aksaray University, Faculty of Engineering, Department of Geomatics Engineering /Aksaray/Turkey

SECTION EDITORS

Assoc. Prof. Dr. Emine BAŞTÜRK, Aksaray University
Assist. Prof. Dr. Bahattin GÜLLÜ, Aksaray University
Dr. Mehmet MESUTOĞLU, Konya Technical University
Dr. Mustafa Haydar TERZİ, Aksaray University

EDITORIAL BOARD

Prof. Dr. Abdurrahman EYMEN, Erciyes University
Prof. Dr. Alper BABA, Izmir Institute of Technology
Prof. Dr. C. Serdar BAYARI, Hacettepe University
Prof. Dr. Fatih İŞCAN, Konya Technical University
Prof. Dr. Fatih POYRAZ, Cumhuriyet University
Prof. Dr. Fevzi KARSLI, Karadeniz Technical University
Prof. Dr. Füsun BALIK ŞANLI, Yildiz Technical University
Prof. Dr. Hakan KARABÖRK, Konya Technical University
Prof. Dr. Hediye ERDOĞAN, Aksaray University
Prof. Dr. Himmet KARAMAN, Istanbul Technical University
Prof. Dr. İbrahim TİRYAKİOĞLU, Afyon Kocatepe University
Prof. Dr. Mehmet ÇELİK, Ankara University
Prof. Dr. Murat YAKAR, Mersin University
Prof. Dr. Mustafa YANALAK, Istanbul Technical University
Prof. Dr. Nebiye MUSAOĞLU, Istanbul Technical University
Prof. Dr. Niyazi ARSLAN, Cukurova University
Prof. Dr. Orhan AKYILMAZ, Istanbul Technical University
Prof. Dr. Reha Metin ALKAN, Istanbul Technical University
Prof. Dr. Tolga ÇAN, Cukurova University
Assoc. Prof. Dr. Ahmet MERT, Isparta University of Applied Sciences
Assoc. Prof. Dr. Emine BAŞTÜRK, Aksaray University
Assoc. Prof. Dr. Hakan YAVAŞOĞLU, Istanbul Technical University
Assoc. Prof. Dr. Hüseyin KARAKUŞ, Dumlupinar University
Assoc. Prof. Dr. Mustafa EL-RAWY, Shaqra University
Assoc. Prof. Dr. Sefa YALVAÇ, Gumushane University
Assoc. Prof. Dr. Selçuk ALEMDAĞ, Gumushane University
Assoc. Prof. Dr. Serkan DOĞANALP, Konya Technical University
Assoc. Prof. Dr. Tekin SUSAM, Gazi Osman Pasa University
Assoc. Prof. Dr. Uğur AVDAN, Eskisehir Technical University
Assoc. Prof. Dr. Zaide DURAN, Istanbul Technical University
Assist. Prof. Dr. Ahmet ÇİLEK, Cukurova University
Assist. Prof. Dr. Aydan YAMAN, Aksaray University
Assist. Prof. Dr. Bahattin GÜLLÜ, Aksaray University
Assist. Prof. Dr. Can İBAN, Mersin University
Assist. Prof. Dr. Erkan YILMAZER, Aksaray University
Assist. Prof. Dr. Esra GÜRBÜZ, Aksaray University
Assist. Prof. Dr. Kamil KARATAŞ, Aksaray University
Assist. Prof. Dr. Nizar POLAT, Harran University
Assist. Prof. Dr. Özlem GÜLLÜ, Aksaray University
Assist. Prof. Dr. Resul ÇÖMERT, Gumushane University
Assist. Prof. Dr. Senem TEKİN, Adıyaman University
Assist. Prof. Dr. Zehra YİGİT AVDAN, Eskisehir Technical University
Dr. Burak Ömer SARAÇOĞLU
Dr. Fabiana CALO, CNR IREA
Dr. Homayoun MOGHIMI, Payame Noor University
Dr. Kaan KALKAN, TUBITAK-UZAY Space Technologies Research Institute
Dr. Mert MUTLU, Aksaray University
Dr. Müge ÜNAL ÇİLEK, Cukurova University
Dr. Syed Mobasher AFTAB, University of Balochistan

ADVISORY BOARD

Prof. Dr. Bahadır AKTUĞ, Ankara University
Prof. Dr. Dursun Zafer ŞEKER, Istanbul Technical University
Prof. Dr. Hacı Murat YILMAZ, Aksaray University
Prof. Dr. Haluk ÖZENER, Bogazici University
Prof. Dr. Hatim ELHATİP, Aksaray University
Prof. Dr. Mustafa AFŞİN, Aksaray University
Prof. Dr. Mustafa IŞIK, Aksaray University
Prof. Dr. Yusuf Kağan KADIOĞLU, Ankara University

TECHNICAL STAFF

Ahmet Tarık TORUN, Aksaray University
Burhan Baha BİLGİLİOĞLU, Gumushane University
Halil İbrahim GÜNDÜZ, Aksaray University
Ozan ÖZTÜRK, ISTANBUL Technical University

Turkish Journal of Geosciences

Volume 3
Issue 1 *June, 2022*

Contents

Research Articles;

TURKGEO
TURKISH JOURNAL OF GEOSCIENCES

***ISSN:** 2717-7696*
Research Article
Vol; 3, Issue; 1, pp. 1-11, 2022
DOI: 10.48053/turkgeo.1056460
Journal homepage:
https://dergipark.org.tr/en/pub/turkgeo

Worldwide crime map applications and usage tendency

Musa Atar*[1], Hacı Murat Yılmaz [1]

[1]Aksaray University, Faculty of Engineering, Department of Geomatics Engineering, Aksaray, Turkey

Keywords
Web-based crime map
GIS
Crime analysis
Crime prevention
Criminology

ABSTRACT

In the dynamic structure of the 21st century, the fight against crime is of increasing interest to the whole society. Law enforcement agencies use crime maps in order to analyze all components of the crime and see them in a single window to develop various scientific strategies. Crime maps that have been used actively for the last 70 years have been given different capabilities with the recent developments in geographic information systems (GIS). In this way, effective crime analyzes can be made, crime prevention tactics and strategies can be developed. Crime information systems, which make it easier to see the events at the desired scale and make quick decisions, are actively used by every law enforcement unit. In some developed countries, crime maps are available to citizens. In our country, a study based on the general framework of a web-based crime information system was carried out with the survey method, which included expectations from the crime map on an international scale. The survey conducted with military personnel of NATO members concluded that a significant majority of respondents were concerned with crime maps and believed that crime maps should be made available to all citizens.

1. INTRODUCTION

The phenomenon of crime is seen as a threat that continues its existence with the history of humanity throughout the world due to its universal feature. Even if it is not possible to reduce this threat to zero, reducing the number and effects of crimes can increase the sense of security, starting from small-scale law enforcement units and extending to large-scale countries (Kanlı and Kaplan, 2018).

In every country, there are organizations that are overseen by the states, that follow up and try to prevent crimes. These organizations want to be able to see the developing situations in a single window. They do this to the extent that their technology allows, and they do some analysis and develop a strategy. Computer technology plays an important role in determining appropriate strategies.

In recent years, with the rapid progress of smart technologies, the concept of smart city has gained a great reputation and a more holistic approach has been adopted for the improvement of urban services in many cities (Başkaya et al., 2020). For example, in the centers that control the tracking of the patrol, it can guide the patrol vehicles or personnel in a healthy way by following the vehicle tracking system and similar applications by using GPS and map location information (Arık, 2019).

The progress of law enforcement in this direction will enable both a more proactive approach and a more appropriate and efficient use of law enforcement agencies. This will mean using resources more efficiently, providing safer settlements and a more prosperous life for citizens (Alkan and Karamanoğlu, 2020).

Crime maps are generally used in the public security system. Although the local academic circles do not draw enough attention to the issue of making these maps public, the fact that the crime map can be studied includes the participation of the citizens in the criminal administration and the inclusion of the effects of the society on this administration in a wide range. Crime maps have been published in foreign countries for nearly two decades. Countries such as England and America have rich application areas. In the United States, the crime reports website collaborates with more than 1,800 law enforcement agencies. American citizens can directly check the

---

* **Corresponding Author**

*(musaatar@yahoo.com) ORCID ID 0000–0001–9847-4877
(hmuraty@gmail.com) ORCID ID 0000-0002-9725-5792

Cite this article

Atar, M., & Yılmaz H.M. (2022). Worldwide crime map applications and usage tendency. Turkish Journal of Geosciences 3(1), 1-11.

Received: 17/01/2022; Accepted: 16/03/2022

number, location, time, type and other information of crimes in various regions and time zones, and can even view identification information, including photos of the suspect in sexual crimes (Yong, 2015).

2. USE OF WEB-BASED CRIME MAPS

It is possible to say that there are 3 main user classes of crime maps in western societies (Rich, 1995). In the first group, there are judicial units, and we can describe them as law enforcement, courts, prison and institutions within the correctional mechanism. Institutions within the prison and correctional mechanisms make analyzes by comparing the addresses of the parolees and the risk areas where they can commit crimes. Another study on this subject is to monitor these people with the GPS system, to determine where they are going on the map and to keep them under control. The second group is non-governmental organizations that take part in the community-supported security model approach. Non-governmental organizations use crime maps in order to be effective in the activities they carry out for the prevention of crime and to analyze the results of their work visually, and direct their work through the analyzes made in this direction. Crime maps and crime information have been made available to the public via the internet by many police agencies in the United States, and it is therefore desirable for the public to have information about crime in their area and to support law enforcement in their work (Wartell, 2001). The third group that uses crime maps is commissions and special task groups working on crime-related issues. These commissions and groups use crime maps to evaluate and direct their work on the map.

Today, with the advancement of technology, real-time reporting of crime incidents has now become possible using smartphones. Although different tools and techniques are used to examine and interpret crime issues, the use of Geographic Information System (GIS) via mobile application is not widespread enough yet (Maghanoy, 2017). In our country, crime information systems are actively used by all three law enforcement agencies. Police, Gendarmerie and Coast Guard agencies have GIS-supported information systems that show the crimes committed as well as preventive measures. In addition, the Security and Emergency Coordination Center (GAMER), a new formation aiming to direct law enforcement, and 112 emergency aid systems a3re GIS-based and work on notification management. As the response teams are integrated with these systems, more effective operations can be carried out. All these systems can only be used by law enforcement via the intranet network, and a web-based crime information system has not been implemented yet.

2.1. Web-Based Information Systems Application

It will be extremely important to obtain real-time updates on where crime is, as well as intelligence information showing where crime may occur in the future (Wartell, 2011). In addition to the use of crime maps by law enforcement, these maps have also been made available to citizens in several developed countries. It can be said that the number of projects benefiting from GIS in the USA for the prevention of crime is increasing. Web-based crime maps are presented with various crime statistics in order to increase public awareness of crime on the internet. It is seen that these applications, which attract the attention of citizens, have an impact on crime rates in terms of the advantages they provide and the results obtained (Kanlı and Kaplan, 2018). In 2014, IOS proposed the use of crime mapping system-based multisourcing in cloud architecture in the operating system. Consisting of a server and processor running in the cloud, users entering the website through the application are intended to interact with criminal content. With the mobile application, it has been made possible to meet the entered incident report and crime map on a single screen. In this way, users can view and interpret the crime that occurs on digital crime maps (Phiri and Lubobyai, 2020; Figure 1). By noticing the crimes near the users and developing measures against crime, it can be evaluated within the framework of preventive law enforcement activities.

Figure 1. Example of crime application (Url-1)

Application examples regarding the use of crime information systems supported by crime maps worldwide as of 2019 are presented below. In Greece, a Google Maps-based crime map for the city of Athens has been put into use (Figure 2). Maps, which contain limited information for the use of citizens, include date and address information as well as crimetypes.

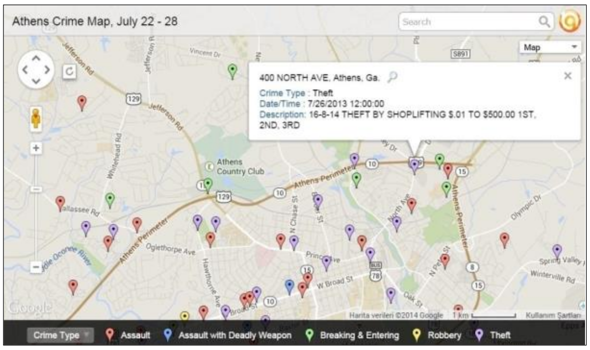

400 NORTH AVE, Athens, Ga.
Crime Type : Theft
Date/Time : 7/26/2013 12:00:00
Description: 16-8-14 THEFT BY SHOPLIFTING $.01 TO $500.00 1ST, 2ND, 3RD

Figure 2. Athens City crime map application (Url-2)

The crime map of the city of Los Angeles was created with the Open Street map infrastructure. By publishing the crime types monthly, the increase and decrease rates of a certain period can be followed (Figure 3).

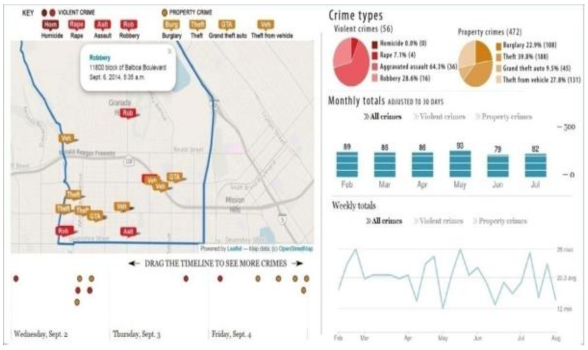

Figure 3. Application of the City of Los Angeles crime map (Url-3)

The Chicago crime map is built on the base map of the city. The crime map, which deals with all types of crimes in detail, also provides convenience to the user with address, zip code, region and known point search tools. The results are presented in the form of points and point clouds (Dalan, 2015; Figure 4).

Figure 4. Chicago crime map application

On the San Francisco city crime map, the user can select the base map from different alternatives such as Bing, Google maps or ESRI. All crime types can be investigated at a known point or address, and can also be converted into reports in .csv, .json, .pdf, .rss, .xls, xlsx and .xml formats (Url-1;Figure 5).

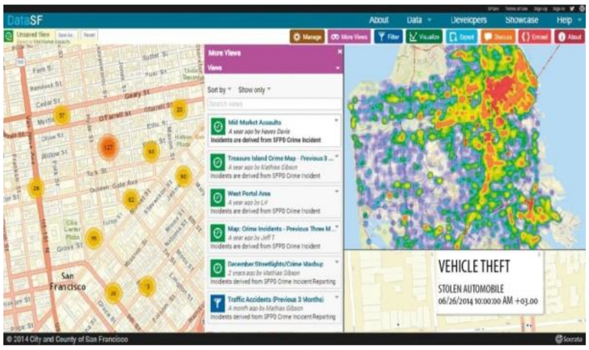

VEHICLE THEFT
STOLEN AUTOMOBILE
06/26/2014 10:00:00 AM +03.00

Figure 5. San Francisco City crime map application

The web-based crime information system called Crime Reports provides Google maps-based crime maps throughout the USA and Canada. Unlike the others, the site, which reports weekly and monthly periods, can also send updates to users (Dalan, 2015; Figure 6).

Theft
1 Block - 10 BLOCK OF THOMAS CIRCLE NW
Identifier:
14137385
Occurred On:
09 Sep 2014 @ 12:07:00 pm
Narrative
THEFT/OTHER-OTHERS
Agency:
Washington DC
Send to friend

Figure 6. USA and Canada crime map application

In the UK, transport police have prepared crime maps to show crimes that occur on trains and stations. The crimes and crime rates at the selected stations can be seen graphically (Dalan, 2015; Figure 7).

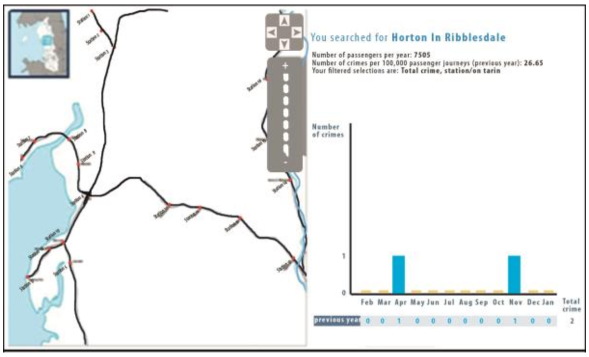
You searched for **Horton In Ribblesdale**

Number of passengers per year: **7505**
Number of crimes per 100,000 passenger journeys (previous year): **26.65**
Your filtered selections are: **Total crime, station/on tarin**

Figure 7. UK Transport police crime map application

The Crime Mapping site presents crimes and law enforcement agencies across the United States to users using ESRI-based maps. The events that occurred are listed by selecting the region or known law enforcement unit to be viewed. Users can get printouts of statistical information (Dalan, 2015; Figure 8).

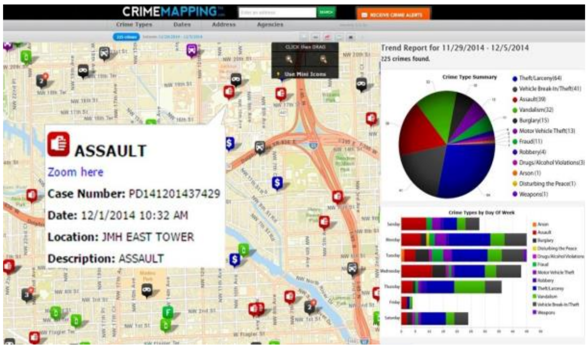

ASSAULT
Zoom here
Case Number: PD141201437429
Date: 12/1/2014 10:32 AM
Location: JMH EAST TOWER
Description: ASSAULT

Trend Report for 11/29/2014 - 12/5/2014
225 crimes found.

Figure 8. UK Transport police crime map application

London crime map presents crimes committed in the city center using maps based on Open Street maps. The amount of crime in a selected region or a marked area can be displayed. In addition, the crimes of the desired date are among the system outputs (Dalan, 2015; Figure 9).

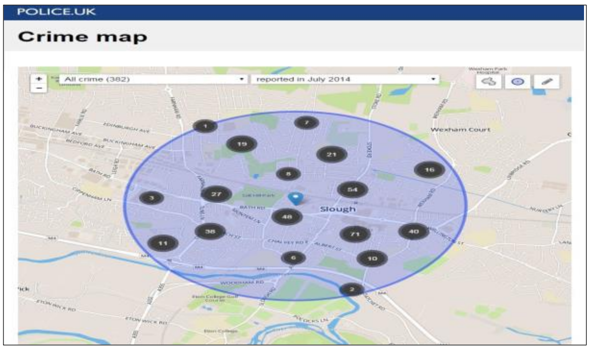

Figure 9. London crime map application

Oakland crime map offers maps based on Open Street map where all crime types can be viewed. In the system where information has been included since 2007, location, date, time and day information of each event is included (Dalan, 2015; Figure 10).

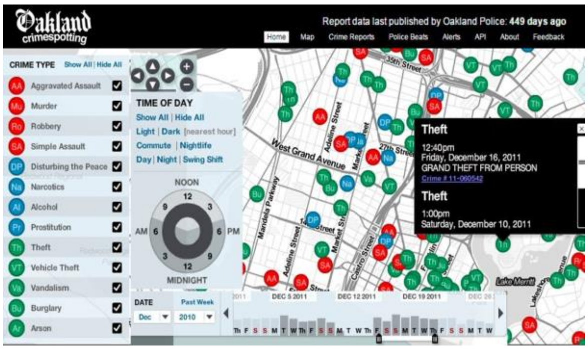

Theft
12:40pm
Friday, December 16, 2011
GRAND THEFT FROM PERSON
Crime # 11-060542

Theft
1:00pm
Saturday, December 10, 2011

Figure 10. Oakland crime map application

With the security map application in Korea, risky areas are presented to users (Figure 11).

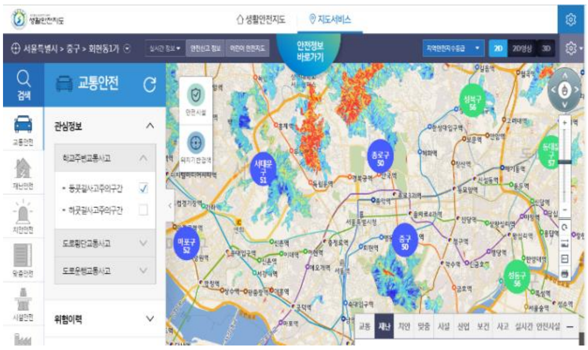

Figure 11. Korea security map application (Url-3).

Crime map for Tokyo city of Japan is published and image is provided for a limited area (Figure 12).


Tokyo Büyükşehir Emniyet Müdürlüğü ana sayfası
Japonca | İngilizce

この地図は、身近な犯罪の発生状況を地域に密着した形で地図上に表示することにより、安全で安心して暮らせるまちの実現のための防犯情報として役立てていただくことを目的としています。

Kasaba ilçe birimi
Tokyo'daki her bir şehrin suç özetini görebilirsiniz.

Şüpheli kişi bilgisi
Şüpheli kişi bilgilerini Tokyo'nun tamamında görebilirsiniz.

Belediye birimi
Belediye biriminin suç özetini Tokyo'da görebilirsiniz.

Smartphone sitesi burada
Lütfen QR kodunu okuyun.
(Bazı modeller desteklemiyor)

Figure 12. Tokyo city crime map application (Url-4)

With the refugee migrant crime map application, Germany publishes the crimes committed by refugees and immigrants in the country other than its own citizens through a web-based crime information system (Figure 13).

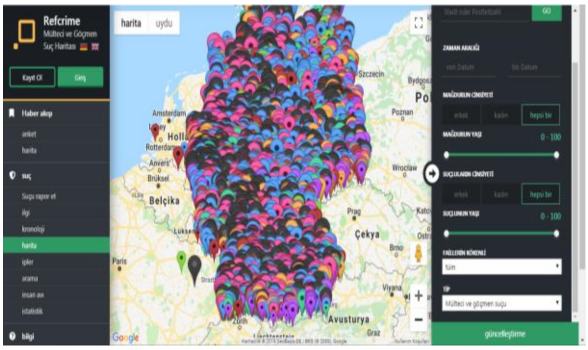

Figure 13. Crimes committed by refugees and immigrants (Url-5)

All necessary statistics about traffic accidents are published on official websites with maps (Url-6) in which the crimes committed throughout the country are shown thematically (Figure 14). The places where the accidents are concentrated on the roads are shown on the map with two-year data sets. (Alkan and Karamanoğlu, 2020).

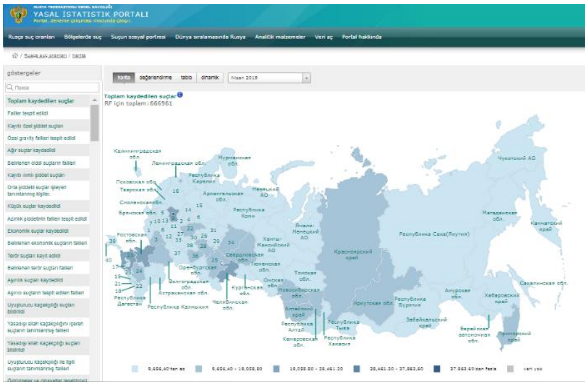

Figure 14. Russia crime map application

There is no web-based crime map application in our country yet. Closed-circuit crime information systems, which are used only for the purpose of facilitating the management of statistics and helping the law enforcement personnel in developing law enforcement strategies, contain crime maps (Url-6).

3. SURVEY STUDY ON THE USE OF CRIME MAP

Table 1. Descriptive feature

Groups	**Frequency (n)**	**Percent (%)**
Age Groups		
30 and below	30	23,1
31-40	52	40,0
41 and older	48	36,9
Countries		
USA	10	7,7
Germany	6	4,6
Denmark	7	5,4
Holland	8	6,2
England	22	16,9
Italy	7	5,4
Mongolia	2	1,5
Poland	13	10,0
Romania	8	6,2
Turkey	43	33,1
New Zeland	4	3,1
Country Groups		
Turkey	43	33,1
ABD & England	32	24,6
Other NATO Countries	55	42,3
Ranks		
NCO Sergeant	5	3,8
NCO Staff Sergeant	14	10,8
Sergeant Major	23	17,7
Lieutenant	8	6,2
First Lieutenant	11	8,5
Captain	16	12,3
Major	34	26,2
Lieutenant Colonel	12	9,2
Colonel	5	3,8
General	2	1,5
Rank Groups		
NCO	42	32,3
Officer	35	26,9
Senior Officer	53	40,8

In order to reflect the purpose and how the crime maps are used around the world, the table that emerged (Table 1) as a result of the survey that measures the tendency of using a comprehensive crime map with the members of the armed forces in NATO countries who are familiar with the crime issue has been presented as a report below. With this study, which includes countries from different geographical regions such as the USA, England, New Zealand and Mongolia, the majority of them are from European countries, it has been tried to measure the perception of crime map in various parts of the world.

3.1.1. Statistical Analysis of Data

The data obtained in the research were analyzed using the SPSS 22 (Statistical Package for Social Sciences) for Windows program. Number and percentage were used as descriptive statistical methods in the evaluation of the data. K-square analysis was used to compare grouped variables.

3.1.2. Findings and Comments

In order to solve the research problem, the findings and comments based on the findings obtained as a result of the analysis of the data collected through the questionnaire from the participants of the research are as follows;

Participants are evenly distributed according to age. It consists of countries in different geographies such as the USA, European countries and Mongolia and New Zealand, most of which are Turkey.

According to country groups, 43 (33.1%) are in Turkey, 32 (24.6%) are in the USA and England, who are already using the web-based crime information system, and 55 (42.3%) are in their country. disintegrates as other NATO countries that do not use the system. According to rank groups, 42 (32.3%) non-commissioned officers, 35 (26.9%) officers and 53 (40.8%) senior officers.

Table 2. Distribution of trends in crime map

Groups	Frequency (n)	Percent (%)
Usage of Crime Map in Your Country		
Yes, national law enforcement publishes	19	14,6
Yes, juidicial units publish	11	8,5
Yes, but not publicly available	38	29,2
No not used	9	6,9
I dont know	53	40,8
Which Regions to Examine When Examining the Crime Map*		
Near my house	81	62,3
Near my workspace	39	30,0
Near the schools	34	26,2
The whole city	73	56,2
The whole country	29	22,3
Which Crimes to Examine When Examining a Crime Map*		
Sexual crimes	59	45,4
Material crimes	86	66,2
Crimes to person	81	62,3
Drug crimes	65	50,0
Terror crimes	69	53,1
Crime Map Review Request		
Yes I am interested in	78	60,0
Yes, I'll take a look	40	30,8
No, I'm not interested in	12	9,2
For what purpose do we want to examine crime maps*		
For my family safety	92	70,8
Because I wonder what's happining around me	85	65,4
To buy property	42	32,3
To warn others	15	11,5
Should crime maps be made public		
Yes	81	62,3
Partly, not for every crime	37	28,5
Law enforcement should know	12	9,2
Reporting a Crime Status		
If I see, yes	91	70,0
Yes, if they don't get me involved with the formalities	14	10,8
I don't care	12	9,2
By type of crime	13	10,0
How Do You Feel When You See a Crime Nearby on the Crime Map		
I feel better because I have knowledge, I take precautions	88	67,7
I worry	26	20,0
Affects the value of the property	16	12,3
How Crime Maps Will Affect Crime Rate		
Will definitely fall	38	29,2
Makes it fall a little	48	36,9
It has no affect	40	30,8
It allows to increase	4	3,1

*Multiple selected items

It is understood that the participants have an awareness level of 60% regarding the use of crime maps in their country. While examining the Crime Map, 78 (60.0%) of them wanted to examine the crime map on a web-based platform, and they mostly wanted to see the crime map around their homes and then the crime distribution in the whole city. In order to maintain their security, it is seen that a significant part of them show interest in the crime map out of curiosity (Table 2).

The vast majority agree with the view that crime maps should be made available to citizens. Participants who understood the purpose of using crime maps stated that they were inclined to report a crime by 70% and would report the crime if they saw it while it was being committed.

When I see a nearby crime on the crime map, 88 (67.7%) feel better because I have knowledge, I take precautions, 26 (20.0%) worry, 16 (12.3%) where I live found negative effects on its value.

It is seen that the crime maps believe that 66% of them will decrease the crime rates, 30.8% will not have any effect, and 3.2% will increase it.

Table 3. Distribution of trends in crime map by age groups

		30 & below		31-40		41 & older		P
		n	%	n	%	N	%	
Status of using a crime map in your country	Yes, national law enforcement publishes	7	%23,3	5	%9,6	7	%14,6	X2=23,661 p=0,003
	Yes, juidicial units publish	2	%6,7	2	%3,8	7	%14,6	
	Yes, but not publicly available	1	%3,3	16	%30,8	21	%43,8	
	No not used	3	%10,0	4	%7,7	2	%4,2	
	I do not know	17	%56,7	25	%48,1	11	%22,9	
Crime map review request	Yes I am interested	16	%53,3	31	%59,6	31	%64,6	X2=4,016 p=0,404
	Yes, I'll take a look	13	%43,3	15	%28,8	12	%25,0	
	No, I'm not interested	1	%3,3	6	%11,5	5	%10,4	
Should crime maps be made public	Yes	22	%73,3	30	%57,7	29	%60,4	X2=2,329 p=0,675
	Partly, not for every crime	6	%20,0	16	%30,8	15	%31,2	
	Law enforcement should know	2	%6,7	6	%11,5	4	%8,3	
Crime reporting status	If I see, yes	19	%63,3	36	%69,2	36	%75,0	X2=1,821 p=0,935
	Yes, if they don't get me involved with the formalities	4	%13,3	6	%11,5	4	%8,3	
	I don't care	4	%13,3	4	%7,7	4	%8,3	
	By type of crime	3	%10,0	6	%11,5	4	%8,3	
How he feels when he sees a nearby crime on the crime map	I feel better because I have knowledge, I take precautions	18	%60,0	34	%65,4	36	%75,0	X2=14,535 p=0,006
	I worry	3	%10,0	15	%28,8	8	%16,7	
	Affects the value of the property	9	%30,0	3	%5,8	4	%8,3	
How crime maps will affect crime rate	Will definitely fall	5	%16,7	15	%28,8	18	%37,5	X2=15,468 p=0,017
	Makes it fall a little	10	%33,3	22	%42,3	16	%33,3	
	It has no affect	15	%50,0	15	%28,8	10	%20,8	X2=15,468 p=0,017
	It allows to increase	0	%0,0	0	%0,0	4	%8,3	

A significant relationship was found between the use of Crime Map in their country and age groups (X2=23,661; p=0.003<0.05; Table 3). There was no significant relationship between the Request for Crime Map Review and age groups (X2=4.016; p=0.404>0.05). There was no significant relationship between the Opinion of Making Crime Maps for Citizen Use and age groups (X2=2.329; p=0.675>0.05). There was no significant relationship between Reporting a Crime and age groups (X2=1.821; p=0.935>0.05).

A significant relationship was found between the age groups and how they felt when they saw a nearby crime on the crime map (X2=14.535; p=0.006<0.05). A significant relationship was found between How Crime Maps Affect the Crime Rate and age groups (X2=15.468; p=0.017<0.05).

Table 4. Distribution of trends in crime map by country groups

		Turkey		USA and UK		Other NATO Count.		p
		n	%	n	%	n	%	
Status of using a crime map in your country	Yes, national law publishes	0	%0	9	%28,1	10	%18,2	X^2=72,805 p=0,000
	Yes, forensic units publish	0	%0	10	%31,2	1	%1,8	
	Yes, but not publicly available	26	%60,5	1	%3,1	11	%20,0	
	No not used	0	%0,0	0	%0,0	9	%16,4	
	I do not know	17	%39,5	12	%37,5	24	%43,6	
Crime map review request	Yes I am interested in	34	%79,1	13	%40,6	31	%56,4	X^2=14,853 p=0,005
	Yes, I'll take a look	9	%20,9	15	%46,9	16	%29,1	
	No, I'm not interested in	0	%0,0	4	%12,5	8	%14,5	
Should crime maps be made public	Yes.	20	%46,5	25	%78,1	36	%65,5	X^2=13,338 p=0,010
	Partly, not for every crime	19	%44,2	7	%21,9	11	%20,0	
	It would be enough if only law knew	4	%9,3	0	%0,0	8	%14,5	
Crime reporting status	If I see, yes	30	%69,8	26	%81,2	35	%63,6	X^2=12,641 p=0,049
	Yes, if they don't get me involved with the formalities	8	%18,6	2	%6,2	4	%7,3	
	I don't care	3	%7	0	%0	9	%16,4	
	By type of crime	2	%4,7	4	%12,5	7	%12,7	
How he feels when he sees a nearby crime on the crime map	I feel better because I have knowledge, I take precautions	28	%65,1	25	%78,1	35	%63,6	X^2=12,372 p=0,015
	I worry	11	%25,6	0	%0	15	%27,3	
	Affects the value of the property	4	%9,3	7	%21,9	5	%9,1	
How crime maps will affect crime rate	Will definitely fall	24	%55,8	1	%3,1	13	%23,6	X^2=37,985 p=0,000
	Makes it fall a little	11	%25,6	10	%31,2	27	%49,1	
	It has no affect	6	%14,0	20	%62,5	14	%25,5	
	It allows to increase	2	%4,7	1	%3,1	1	%1,8	

A significant relationship was found between the use of a crime map in their country and country groups (X2=72.805; p=0.000<0.05; Table 4). In the USA and England group, the rate of national law enforcement publications is higher than the Turkey group. In the USA and UK group, the rate of publishing yes forensic units is higher than in the Turkey group. In the Turkey group, yes, but not available to the citizens, the rate is higher than the other NATO countries group. In the group of other NATO countries, the rate of no use is higher than in the group of Turkey. In the group of other NATO countries, ignorance is higher than in the US and UK group.

A significant relationship was found between Crime Map Review Request and country groups (X2=14.853; p=0.005<0.05). In the Turkey group, the rate of the desire to examine the crime map is higher than the USA and England groups. In the USA and England group, yes, I look at it from time to time, is higher than the Turkey group. In the group of other NATO countries, the rate of "no, I am not interested" is higher than the group of Turkey.

A significant relationship was found between the Opinion of Making Crime Maps for Citizen Use and country groups (X2=13.338; p=0.010<0.05). The opinion that crime maps should be made available to citizens in the USA and England group is higher than that of the Turkey group. In the Turkey group, the rate, in part, not for all crimes, is higher than the group of other NATO countries. In the Turkey group, the rate of opinion, if only the law enforcement knew, would be sufficient compared to the USA and England groups.

A significant relationship was found between Reporting Crime and country groups (X2=12.641; p=0.049<0.05). If the case of reporting a crime in the USA and England group is in front of my eyes, the rate of being yes is higher than the group of other NATO countries. In the group of other NATO countries, if they do not involve me in formalities, the yes rate is higher than the group of Turkey. The rate of none of my concern is higher in the Turkey group than in the USA and UK groups. The rate of variation according to crime is higher in the Turkey group than in the USA and UK groups.

A significant correlation was found between the country groups and how they felt when they saw a nearby crime on the crime map (X2=12.372; p=0.015<0.05). The rate of being able to feel better and take precautions is higher in the USA and UK group, as I have information about how they feel when they see a crime close to them on the crime map, compared to the other NATO countries group. In the group of other NATO countries, the rate of worry is higher than in the USA and UK group. In the Turkey group, the rate of negative effects on the value of the place where I live is higher than in the USA and UK groups.

A significant relationship was found between How Crime Maps Affect the Crime Rate and country groups (X2=37,985; p=0.000<0.05). Regarding how the crime maps will affect the crime rate in the Turkey group, the rate of definitely lowering is higher than the other NATO countries group. In the group of other NATO countries, the rate that allows it to fall slightly is higher than the group of Turkey.

In the USA and England group, the rate of no effect is higher than the Turkey group. In the Turkey group, the rate of increase is higher than the other NATO countries group.

Table 5. Distribution of tendencies for crime map by rank groups

		NCO		**Officer**		**Major&up**		**NCO**
		n	**%**	**n**	**%**	**n**	**%**	
Status of using a crime map in your country	Yes, national law publishes	%7,1	9	3	%7,1	9	%18,2	X^2=21,951 p=0,005
	Yes, forensic units publish	%4,8	1	2	%4,8	1	%1,8	
	Yes, but not publicly available	%28,6	4	12	%28,6	4	%20,0	
	No not used	%7,1	3	3	%7,1	3	%16,4	
	I do not know	%52,4	18	22	%52,4	18	%43,6	
Crime map review request	Yes I am interested in	%57,1	15	24	%57,1	15	%56,4	X^2=12,695 p=0,013
	Yes, I'll take a look	%26,2	16	11	%26,2	16	%29,1	
	No, I'm not interested in	%16,7	4	7	%16,7	4	%14,5	
Should crime maps be made public	Yes.	%59,5	21	25	%59,5	21	%65,5	X^2=4,886 p=0,299
	Partly, not for every crime	%35,7	8	15	%35,7	8	%20,0	
	It would be enough if only law knew	%4,8	6	2	%4,8	6	%14,5	
Crime reporting status	If I see, yes	%59,5	27	25	%59,5	27	%63,6	X^2=7,988 p=0,239
	Yes, if they don't get me involved with the formalities	%11,9	3	5	%11,9	3	%7,3	
	I don't care	%19,0	1	8	%19,0	1	%16,4	
	By type of crime	%9,5	4	4	%9,5	4	%12,7	
How he feels when he sees a nearby crime on the crime map	I feel better because I have knowledge, I take precautions	%61,9	19	26	%61,9	19	%63,6	X^2=10,639 p=0,031
	I worry	%28,6	8	12	%28,6	8	%27,3	
	Affects the value of the property	%9,5	8	4	%9,5	8	%9,1	
How crime maps will affect crime rate	Will definitely fall	%33,3	5	14	%33,3	5	%23,6	X^2=10,314 p=0,112
	Makes it fall a little	%35,7	13	15	%35,7	13	%49,1	
	It has no affect	%26,2	17	11	%26,2	17	%25,5	
	It allows to increase	%4,8	0	2	%4,8	0	%1,8	

A significant relationship was found between the Crime Map Review Request and rank groups (X2=12.695; p=0.013<0.05; Table 5). In the senior officer group, the rate of wanting to examine the crime map is higher than the officer group. In the officer group, yes, I look at the rate is higher than the senior officer group. In the non-commissioned officer group, the rate of no interest is higher than that of the senior officer group.

There was no significant relationship between the Opinion of Making Crime Maps for Citizen Use and rank groups (X2=4.886; p=0.299>0.05). There was no significant relationship between Reporting a Crime and rank groups (X2=7,988; p=0.239>0.05).

A significant relationship was found between the rank groups and how they felt when they saw a nearby crime on the crime map (X2=10.639; p=0.031<0.05). The rate of being able to feel better and take precautions is higher in the senior officer group than in the officer group, because I have information about how they feel when they see a crime near them on the crime map. The rate of being worried is higher in the non-commissioned officer group than in the senior officer group. In the non-commissioned officer group, the rate of negative effects on the value of the place where I live is higher than the officer group.

There was no significant relationship between How Crime Maps Affect the Crime Rate and rank groups (X2=10.314; p=0.112>0.05).

4. RESULTS

Digital crime maps, which are very useful for law enforcement, serve especially for law enforcement chiefs in recognizing the region and developing precautions as a result of a quick analysis. Discussions on making it available to citizens continue. Despite the view that reporting every crime to the citizen will bring anxiety and insecurity rather than benefit, according to many opinions, transparent law enforcement, transparent justice system and citizens with increased awareness mean a safer society in the long run. After this study, it is seen that crime maps are not available to citizens in many NATO countries, and crime maps are actively used by law enforcement in many of them. However, almost all the participants who participated in the survey stated that they were interested in the crime map, that they wanted to examine it and that they thought it would be useful.

When the security need desired by the society is not met as desired, other needs will not emerge as needs. In order for people to continue their social life, they must first be sure that their own safety of life and property is ensured (Sarı and Özgür, 2019). It can be said that mapping the crimes that occur with GIS is important for the implementation of both "Social Crime Prevention" and "Spatial Crime Prevention" strategies (Kanlı and Kaplan, 2018).

In the twenty-first century, where the use of GIS-supported web-based crime maps is rapidly increasing, it is considered that internet users will show more interest in crime maps and thus contribute to the fight against crime, and that the individual awareness created will have a positive effect on the decrease in crime rates.

Acknowledgement

This article was produced from Musa ATAR’s PhD. thesis.

Author Contributions

Musa Atar: Methodology, Software, Validation, Formal analysis, Writing-Original Draft, Visualization. **Hacı Murat Yılmaz:** Supervision, Writing-Original Draft.

Conflicts of Interest

The authors declare no conflict of interest.

REFERENCES

Alkan, N., & Karamanoğlu, Y.E. (2020). Öngörüye dayalı kolluk temelinde önleyici kolluk: Rusya Federasyonu’ndan örnekler. *Güvenlik Bilimleri Dergisi*, 9(2), 387-418 (in Turkish).

Arık, G. (2019). A technology acceptance model suggestion for public order services and the effect of case-based training on technology acceptance (PhD thesis). Hacettepe University, Ankara, Turkey (in Turkish).

Başkaya, O., Ağaçsapan, B., & Çabuk, A. (2020). Akıllı şehirler kapsamında yapay zekâ teknikleri kullanarak etkin ulaşım planlarının oluşturulması üzerine bir model önerisi. *GSI Journals Serie C: Advancements in Information Sciences and Technologies*, 3(1), 1-21.

Dalan, Ö. (2015). Intelligent geographical ınformation system for criminology (PhD thesis). Dokuz Eylül University, İzmir, Turkey.

Phiri, J., & Lubobyai, C.S. (2020). Crime mapping model based on cloud and spatial data: a case study of Zambia police service. *International Journal of Advanced Computer Science and Applications*, 11(1), 251-265.

Kanlı İ.B., & Kaplan, B. (2018). Kentsel güvenliğin sürdürülebilirliğinde ileri teknolojilerin kullanılması: Coğrafi Bilgi Sistemleri. *TESAM Akademi Dergisi*, 143-186.

Maghanoy, J.A.W. (2017). Crime mapping report mobile application using GIS. *IEEE 2nd International Conference on Signal and Image Processing (ICSIP)*, 247-251.

Rich, T.F. (1995). The use of computerized mapping in crime control and prevention programs, 2, 2. US Department of Justice, Office of Justice Programs, National Institute of Justice.

Sarı, G., & Özgür, E. (2019). Kamu alanında güvenlik ve emniyet algısı. *13. Uluslararası Kamu Yönetimi Sempozyumu*, Gaziantep Üniversitesi.

Wartell, J. (2011). Independent Adviser on Public Safety, GIS for Proactive Policing and Crime Analysis, Presentation at the Technologies for Critical Infrastructure Protection Conference, National Harbor.

Wartell, J. (2001). Privacy in the information age: a guide for sharing crime maps and spatial data. US Department of Justice, Office of Justice Programs, National Institute of Justice.

Yong, S. (2015). Disclosure of crime map., http://www.iolaw.org.cn/showNews.aspx?id=50993 (last accessed 18 June 2021)

Url-1: https://kknews.cc/zh-hk/news/9j6ve8q.html (last accessed 15 Nov 2021)

Url-2: https://www.redandblack.com/cops/maps/athens-crime-map-july-22---28/article_c35efb04-f874-11e2-9163-0019bb30f31a.html (last accessed 15 Nov 2021)

Url-3: http://www.safemap.go.kr/main/smap.do?flag=2 (last accessed 27 Dec 2021)

Url-4: http://www2.wagmap.jp/jouhomap-sp/) (last accessed 21 Dec 2021)

Url-5: https://www.refcrime.info/de/verbrechen/karte (last accessed 27 June 2021)

Url-6: http://crimestat.ru/offenses_map (last accessed 12 Nov 2021)

TURKGEO
TURKISH JOURNAL OF GEOSCIENCES

ISSN: *2717-7696*
Research Article
Vol; 3, Issue; 1, pp. 12-21, 2022
DOI: *10.48053/turkgeo.1028669*
Journal homepage:
https://dergipark.org.tr/en/pub/turkgeo

Dolomitization mechanism in the Chorgali formation, Pakistan: Evidence from field observations, Petrography, Mineralogical, and SEM analysis

Sajjad Khan[*1], **Mehboob Ur Rashid** [1]

[1]*Geoscience Advanced Research Laboratories (GARL), Geological Survey of Pakistan, Shahzad Town, 1461 Islamabad, Pakistan*

Keywords
Dolomitization
Petrographic study
Geochemical characteristics
Chorgali Formation

ABSTRACT

The subject of dolomite formation has always put researchers in the challenge. In this study, the origin of the dolomites of the Chorgali Formation near Chorgali Pass was explored through field observation, petrographic characteristics, mineralogical and geochemical analysis. Analytical analyses used in the present studies include XRD, SEM-EDS, and stable isotopes studies. The dolomites were categorized into three major genetic types based on their textural and structural features showing their distinct origins. These dolomites are named fine crystalline dolomite (Df), medium crystalline dolomite (Dm), and coarse crystalline dolomite (Dc). The analytical approaches linked with field observations and petrographic examinations identified that; the first type of dolomites (i.e., Df) is related to the early stage of diagenesis and contain the presence of mineral dolomite (40%), gypsum (27%), quartz (17%) and albite (16%) and are low stochiometric low ordered in character as recognized by XRD results. The SEM-EDS analysis identified low Mg, Ca, O, Na, Si, and Fe concentrations. Further, the stable isotopes (δ18O) values for Df (i.e., -5.95 to -396‰V-PDB) are less depleted. Moreover, Dm and Dc revealed 100% mineral dolomite and are stochiometric ordered dolomites. High concentrations of Mg, Ca and O are observed in Dm and Dc respectively. Stable isotopes (δ18O) result in exhibiting highly depleted values for Dm (-7.947‰V-PDB) and Dc (-9.227 to -8.302‰V-PDB) showing its formation with the elevated temperature at depth. In addition, δ13C values of Df, Dm, and Dc lie in the range of the original marine signature of Eocene times.

1. INTRODUCTION

The study area lies in Survey of Pakistan (SOP) toposheet no. 43-C/11 at Latitude 33° 27' 05″ N and Longitude 72° 41' 02″ E (Figure 1). The rocks exposed in the study area are ranging in age from Eocambrian to Pleistocene (Jaswal et al., 1997). The rocks of Eocene age include Margala Hill Limestone, Chorgali, Kuldana formations, whereas Murree Formation represents Miocene age. According to Shah, (2009) and Shah and Khan, (2016) the formation is mainly contained of dolomite, dolomitic limestone, and shale. It is well known that the Chorgali Formation is performing as a reservoir in many oil fields (Kadri, 1995; Benchilla et al., 2002a). Previous work is mainly focused on the outcrop-based sedimentology and depositional environment of the Chorgali Formation (Mujtaba et al., 1989; Jurgan and Abbas, 1991; Mujtaba, 2001; Awais et al., 2019). The present study deliberates inclusive investigations of the dolomitization evolution mechanism in the Chorgali Formation near Chorgali Pass Pakistan.

---

* **Corresponding Author**

*(pkpkgeo@gmail.com) ORCID ID 0000-0003-2730-0997
(mehboobgeo89@gmail.com) ORCID ID 0000-0003-2555-239X

Received: 26/11/2021; Accepted: 07/04/2022

Cite this article

Khan, S., & Rashid M.U. (2022). Dolomitization Mechanism in the Chorgali Formation, Pakistan: Evidence from Field observations, Petrography, Mineralogical, and SEM analysis 3(1), 12-21.

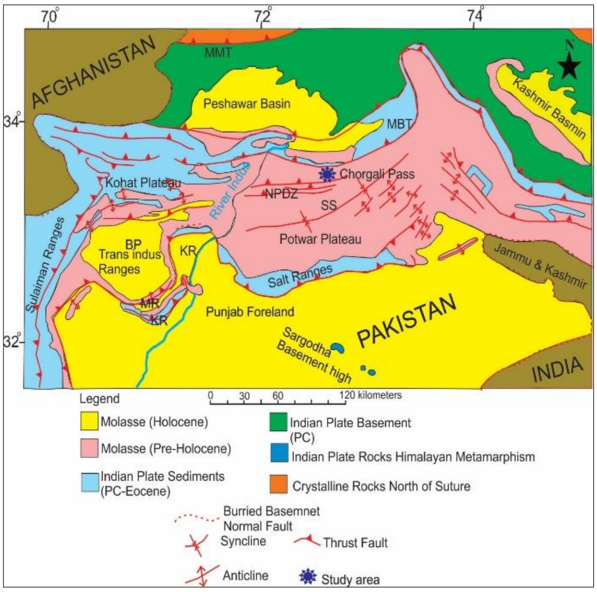

Figure 1. Geo-Tectonic map of Kohat-Potwar area showing the location of the study area (modified after Kazmi and Rana, 1982). Abbreviations used are; SS= Soan Syncline, NPDZ= North Potwar Deformed Zone, MBT= Main Boundary Thrust, MMT=Main Mantle Thrust, KR= Kishor Range, MR= Marwat Range, and BP= Bannu Promontory

2. GENERAL TECTONIC CONTEXT

The research site is being a portion of the Indian Plate. Previous work revealed that the Indian Plate has traveled 9000 kilometers during its tectonic evolution after detachment from its position in the Gondwana, its consecutive departure from other continents of Gondwana, its frequent disintegration, its movement in the north direction, and its sequential crash with KIA and with Asia (Chatterjee, 1992; Chatterjee and Scotese, 1999, 2010). Furthermore, the Indian Plate represents distinct and highly complex tectonic antiquities (Chatterjee et al., 2013). During its northward movements, the Indian plate experienced unexpected acceleration from Late Cretaceous to Early Eocene, about 20 cm/year, and then histrionically reduced to 5 cm/year during its collision with Eurasian Plate (McKenzie and Sclater, 1971; Patriat and Achache, 1984; Lee and Lawver, 1995). The crash (i.e., happened around 67±2 Ma) between the Indian Plate and Eurasian Plate is considered the intense tectonic incident of the Cenozoic and is responsible for the uplift of the Himalayan-Tibetan Plateau (Powell et al., 1988; Powell and Conaghan, 1973).

The study area lies in the area of the Northern Potwar Deformed Zone of the Indian Plate, where extensive complex structural and tectonic features are present (Figure 1; Jaswal et al., 1997). Multipart and tight folds, which are trending east-west and are overturned to the south at sheared by step-angle faults are present in the area (Baker, 1987). Furthermore, the studied area is highly tectonically disturbed with seven episodes of fracturing were identified showing the complex deformation past that is characteristic of a fold-and-thrust belt (Benchilla et al., 2002b). Main Boundary Thrust (MBT) lies in the north and Soan Syncline exists south of the area (Figure 1). Furthermore, the studied section can be accessed from all sides of the country by roads, approximately lies 55 km in the south-west of the main capital Islamabad and 190 km from Peshawar (Figure 1).

3. MATERIAL AND METHODS

Forty-one representative samples were taken from 150-meter-thick studied sites during field studies (Figure 1). Dolomite samples were separated by applying pre-microscopic methods (etching, staining, peeling, etc.,). Petrographic thin sections were prepared including alizarin red S and K-ferricyanide analysis and studied under a microscope for the identifications of various diagenetic phases. Thin sections preparation, Petrography, XRD analysis, and SEM studies were executed at Geoscience Advance Research Laboratories, Geological Survey of Pakistan Islamabad. Polarizing microscope (OPTIPHOT2-POL) with an attached camera (Moticam 2000) were used for the identification of diagenetic phases. A powdered sample of 2-5 grams was taken in a specified XRD sample holder and prepared for XRD analysis. The XRD analyses were carried out by Panalytical X'Pert Pro Diffractometer (XRD) at 45 kV and 40 mA with CuKα radiations scanning speed at 0.05°/s. The XRD patterns were identified by using X pert High Score Plus software. SEM Model JEOL JSM 6610LV with EDS (OXFORD X-MAX 20 mm2) is used in the present study. Moreover, during sample preparations, carbon coating is well applied all around the samples to avoid charging the samples under the SEM.

For measuring carbon and oxygen stable isotopic composition of various diagenetic phases micro sampled were obtained by using a dentist's micro-drill. Bulk rock analyses were carried out at PINSTECH (Pakistan Institute of Nuclear Science and Technology), Islamabad. During this process, the carbonate powders were reacted with 100% phosphoric acid (density >1Æ9; Wachter and Hayes, 1985) at 75°C in an online carbonate preparation line (Carbo-Kiel – single sample acid bath) connected to a Thermo Finnigan 252 mass-spectrometer (Thermo Electron Corp., Waltham, MA, USA). All values are reported in per million relatives to Vienna Pee Dee belemnite standard (V-PDB) by assigning a δ13C value of +1Æ95& and a δ18O value of)2Æ20& to National Bureau of Standards (NBS) 19. Oxygen isotopic compositions of dolomites were corrected using the fractionation factors given by Rosenbaum and Sheppard, (1986). Reproducibility based on a replicate analysis of laboratory standards is better than ±0Æ02& for δ13C and ±0Æ03& for δ18O.

4. FIELD OBSERVATIONS

In the studied section the Chorgali Formation is mainly comprised of two main units. The lower unit exhibits the presence of dolomite, dolomitic limestone, and shale, whereas the upper unit contains one thick bed of dark grey color limestone and a bed of nodular argillaceous limestone almost near the top. The shale is greenish-grey, red occasionally variegated, and calcareous. Some grit beds are also intercalated. Well preserved cyanobacterial mat, lamination, mud-cracks, and horizontal burrows have also been observed. Anhydrite nodules are also noted during field observations (Figure 2a-e).

Figure 2. Field observations of dolomites of Eocene Chorgali Formation, near Chorgali Pass; (a) General view of the dolomites of Eocene Chorgali Formation, near Chorgali Pass (b) Dolomite sample exhibiting well preserved cyanobacterial mat (c) Dolomite sample showing well-developed lamination, mud-cracks and horizontal burrows (d) Irregular laminations observed in dolomites (e) The presence of anhydrite nodules (white color) in dolomites of Chorgali Formation

5. PETROGRAPHIC STUDY

5.1. Fine crystalline dolomite (Df)

According to Sibley and Gregg, (1987) classification scheme, fine crystalline dolomites (Df) are 5-50 µm in size, planar-s, light grey to medium grey color dolomites and are mostly comprised of partially dolomitized fossiliferous micrite with sparse, randomly distributed, very fine-grained detrital quartz grains are present (Figure 3a). Bioclasts include sparse ostracod and some unidentified very small-sized fossil fragments. Fine to very finely crystalline dolomite crystals are common and randomly distributed in the micritic matrix. A few well-developed, medium-sized, dolomite rhombs are noticed with cloudy centers and comparatively clear rims. A few, fine sand-sized, intraclasts are also present. Randomly distributed dolomicritic intraclasts are common and represent disintegrated algal mats (Figure 3b). Although fabric destructive dolomitization has completely destroyed the original fabric information, a few intraclasts ghosts are present. Open micro molds and micro vugs are common and randomly distributed. Locally developed microfractures are noticed filled with anhydrite (Figure 3c). Anhydrite nodules show the phenomenon of chicken wire features, indicating growth by displacement. Very finely crystalline, well-developed, pyrite-looking crystals are locally common within the groundmass of dolomite and anhydrite laths (Figure 3d).

5.2. Medium crystalline dolomite (Dm)

Dm is 50-200µm, medium to dark grey, locally laminated dolomites. Dolomite crystals are medium crystalline, equigranular, and subhedral (Figure 3e;

Sibley and Gregg, 1987). Furthermore, intercrystalline spaces are filled with cryptocrystalline carbonate. Most of the dolomite crystals have light-brown cloudy centers with clear rims. Dolomitization has completely destroyed the fabric information of the precursor sediments.

5.3. Coarse crystalline dolomite (Dc)

These consist of 200μm -2 mm-sized, medium gray, coarse crystalline euhedral to subhedral dolomites that occur generally as infilling of fractures (Figure 3f-g; Sibley and Gregg, 1987). Dc is locally stylolites and fractures associated. Filled and partially open fractures and microfractures are locally common. Pyritization is also associated. Light gray dolomite (collapse breccia). Ghosts of intraclasts and fecal pellets are randomly scattered in a groundmass of finely crystalline dolomite. Dolomite crystals have mostly cloudy centers and clear rims. Intercrystalline and vuggy porosity are locally common. Some of the pores are partially filled with natural solid bitumen. Open microfractures and a few microstylolites are present.

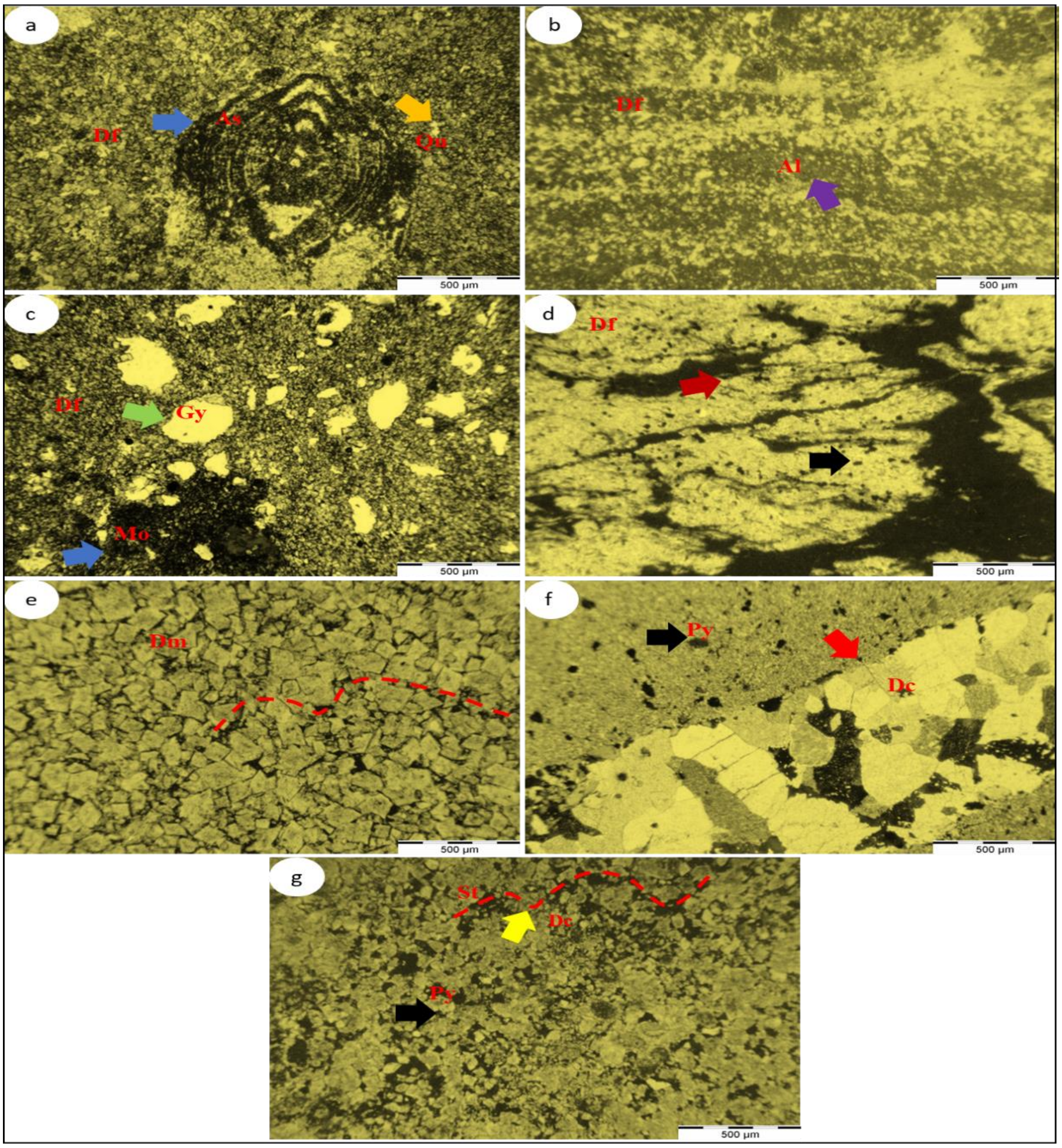

Figure 3. Petrographic characteristics of dolomites of Chorgali Formation; (a) Photomicrograph exhibiting fine crystalline dolomites (Df), the blue arrow shows the presence of dolomitized bioclast (i.e., Assilina) whereas blue arrow represents fine quartz grains (b) Fine crystalline dolomites (Df), purple arrow shows ghost of the algal mat (c) Fine crystalline dolomites (Df) with open molds as blue arrow and presence of gypsum anhydrite as green arrow (d) Fine crystalline dolomites (Df) with chicken wire features as brown arrow and pyrite existence as a black arrow (e) Photomicrograph exhibiting medium crystalline dolomite i.e., Dm with stylolite seems (f) Photomicrographs showing coarse crystalline dolomite (Dc) as a red arrow, pyrite represented by black arrow (g) Coarse crystalline dolomite (Dc) as a red arrow, pyrite represented by the black arrow, yellow arrow shows stylolite seems. Abbreviations; Df=fine crystalline dolomites, As=Bioclast (Assilina), Qu=Quartz, Al =Algal mat, Gy=Gypsum, Mo=Open mould, Dm=Medium crystalline dolomite, Py=Pyrite, Dc=Coarse crystalline dolomite, St=Stylolite

6. XRD ANALYSIS

XRD studies of representative samples were carried out. Df exhibited the presence of dolomite (40%), gypsum (27%), quartz (17%), and albite (16%) respectively (Figure 4a). In Dm and Dc, the existence of dolomite (100%) is observed (Figure 4b-c). Besides this, the mol % Ca Vs I(d105)/I (d110) plot showed that Df is low stochiometric low ordered dolomites, whereas Dm and Dc are near stochiometric ordered dolomites (Figure 5 and Table 1).

Table 1. XRD results of analyzed samples

Site	Stage	d_{104}	d_{015}	d_{110}	$I(d_{015})/I(d_{110})$	mol % Ca
Chorgali - pass	D. I	2.871	2.531	2.401	1.054	45.000
	D. I	2.869	2.531	2.402	1.054	44.334
	D. I	2.872	2.532	2.402	1.054	45.334
	D. I	2.870	2.530	2.401	1.054	44.667
	D. II	2.880	2.535	2.402	1.055	48.000
	D. III	2.881	2.536	2.402	1.056	48.334
	D. III	2.882	2.536	2.401	1.056	48.667

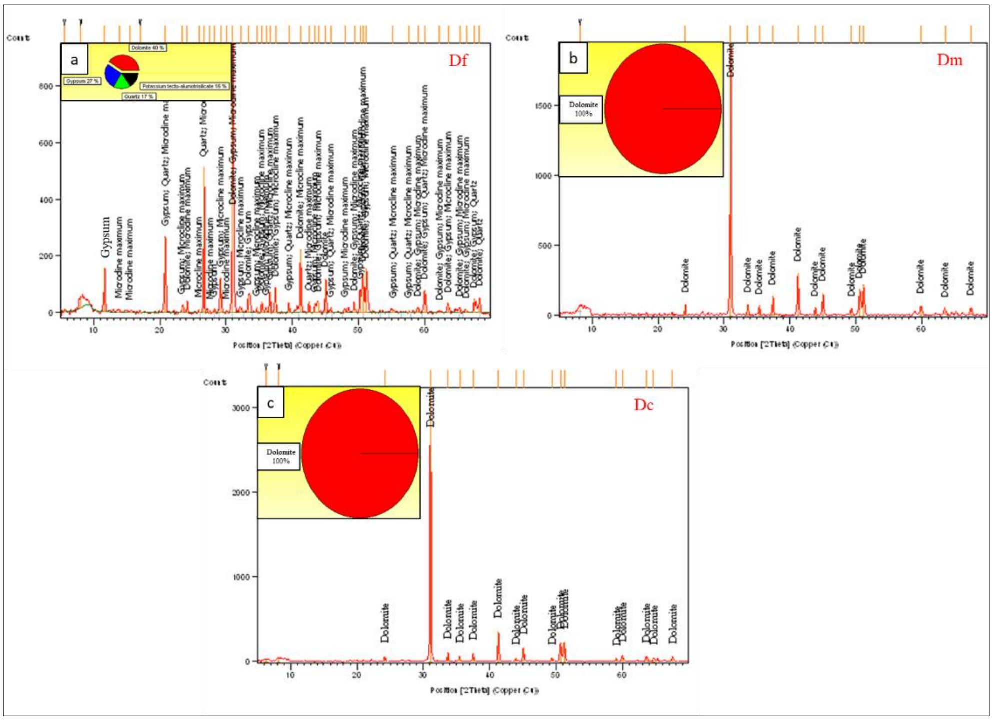

Figure 4. XRD results of the dolomites in Eocene Chorgali Formation; (a) XRD pattern showing mineralogical description with quantification of Df, (b) XRD pattern showing mineralogical description with quantification of Dm and, (c) XRD pattern showing mineralogical description with quantification of Dc. Abbreviations; Df=Fine crystalline dolomites, Dm= Medium crystalline dolomite, Dc= Coarse crystalline dolomite

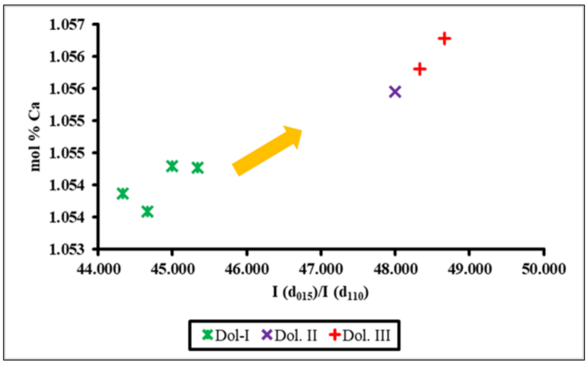

Figure 5. Mol % Ca vs I $(d_{015})/I(d_{110})$ plot of various phases of Eocene Chorgali dolomites

7. SEM-EDS ANALYSIS

In the SEM-EDS studies, Df showed the presence of Mg, Ca, O, Na, Si, and Fe concentrations (Figure 6a). The highest concentrations of Mg, Ca and O are observed in Dm and Dc respectively (Figure 6b-c).

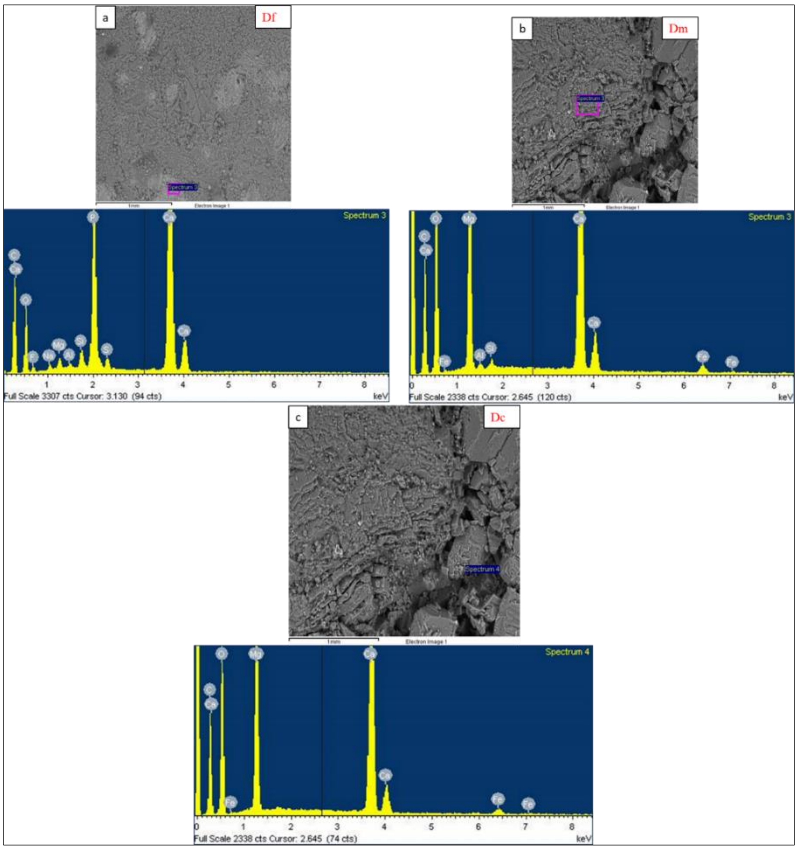

Figure 6. Scanning electron microscope (SEM) results of selected samples from identified dolomite phases; (a) detailed SEM results of Fine crystalline dolomites (Df), (b) SEM results of Medium crystalline dolomite (Dm) and, (c) SEM results of Coarse crystalline dolomite (Dc)

8. STABLE ISOTOPES ANALYSIS

Stable isotopes (δ18O and δ13C) values for Df are -5.95 to -396 and δ -0.85 to 2 respectively (Figure 7 and Table 2). In Dm δ13C and δ18O are -7.947 and -0.104 respectively, whereas Dc revealed δ18O (-9.227 to -8.302) and δ13C (-0.928 to 1.337) values (Figure 7 and Table 2).

Table 2. Isotopes results of analyzed samples

Section	Stage	$\delta^{18}O$	$\delta^{13}C$
Chorgali - Pass	Df	-3.96	-0.96
	Df	-5.95	-0.085
	Df	-3.96	2.96
	Df	-3.96	-0.96
	Dm	-7.947	-0.104
	Dc	-8.302	-0.928
	Dc	-9.227	1.337

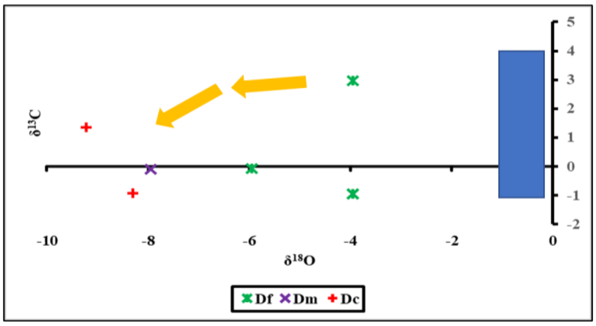

Figure 7. δ18O Vs δ13C plot of various phases of Eocene Chorgali dolomites. The blue rectangle represents the marine signatures of Eocene Limestone

9. Discussions

During field investigations, the presence of well-preserved cyanobacterial mat, lamination, mud-cracks, and horizontal burrows are observed along with the dolomites of the Chorgali Formation (Figure 2a-e). The presence of anhydrite nodules with chicken is also associated with these dolomites (Figure 2e). Cyanobacterial mat, lamination, mud-cracks, horizontal burrows, and gypsum/anhydrite nodules are typical features of inter-and supra-tidal settings and are found in dolomites formed in tropical and arid conditions (Gasparrini et al., 2003;

Warren 2000, 2006). In such arid conditions, increased rates of evaporation in lagoons produce denser and more saline waters (with respect to seawater), promoting dolomitization as Mg becomes highly concentrated in the brines and the kinetic constraints of dolomitization alleviated. Thus, hypersaline fluids, usually produced by high rates of evaporation, resulting in the precipitation of dolomites along with gypsum and anhydrite (Mckenzie, 1981). During petrographic examinations, fine crystalline dolomite (Df) exhibited small crystal size and planar intercrystalline boundaries with fabric retentive character are the possibilities of the dolomites formed in supratidal and intertidal realms in the early stage of diagenesis near-surface low-temperature conditions (Figure 3a-d; Saller, 1984; Gregg and Sibley, 1984; Land, 1985; Sibley and Gregg, 1987; Mitchell et al., 1987; Gregg and Shelton, 1990; Rahimi et al., 2016). According to Shah, (2009) the epeirogenesis experienced resultant emergence in various areas of Pakistan, and this caused unconformities of varying magnitude. These early-stage diagenetic processes can be possibly related to Middle-Late Eocene unconformities. The XRD studies showed the existence of dolomite, gypsum, quartz, and albite in Df (Figure 4). Based on XRD data Df is identified as low stochiometric low ordered dolomites (Figure 5). Furthermore, SEM analysis accredited low concentrations of Mg, Ca, O, Na, Si, and Fe in these dolomites (Figure 6). Stable isotopes (C & O) exhibited slightly depleted values for Df (Figure 7).

Based on field observation, microscopic examinations linked with XRD, SEM-EDS, and Isotopes analysis fabric retentive dolomites (Df) can be interpreted to be of early diagenetic origin. Furthermore, the similarity between Chorgali shallowing upward sequence and Persian Gulf sabkha sequence suggests that the formation of these early diagenetic Chorgali dolomites was similar to that of Holocene dolomite in the Persian Gulf; where the sediments are being dolomitized by evaporated seawater (Illing et al., 1965; Mckenzie, 1981; Patterson and Kinsman, 1982).

The microscopic examinations revealed that medium crystalline dolomites (Dm) are fabric destructive in character and with stylolite seems, which predominantly occupy the lower portion of the sequence (Figure 2e) and their formation possibly occurs at slighter depth after the formation of Df (Mountjoy et al., 1999; Duggan et al., 2001; Fabricius et al., 2007). The XRD results showed that it contains 100% mineral dolomite and is nearly stochiometric ordered dolomite (Figure 4a-c and Figure 5). Furthermore, SEM-EDS analysis identified strong concentration peaks of Mg in Dm (Figure 6). Stable Isotopes values (δ18O) of these dolomites are highly depleted than Df reflecting its formation in a higher temperature at depth (Figure 7).

The late diagenetic fracture and void filling dolomite cement (Dc) with curved surfaces and undulatory extinction under cross-polarized light probably formed as fluids moved along paths of increased permeability created by burrows, fractures, and stylolites (Figure 3f-g; Zenger, 1983; Amthor and Friedman, 1991). Petrographic characteristics combined with XRD data, SEM-EDS analysis, and stable isotopes results identified that these dolomites are formed at great depth with elevated temperature after the deposition of thick sedimentary cover above (Figure. 4-7; Guo et al., 2016; Feng et al., 2017). Pyritization marks the end of diagenesis (Figure 8).

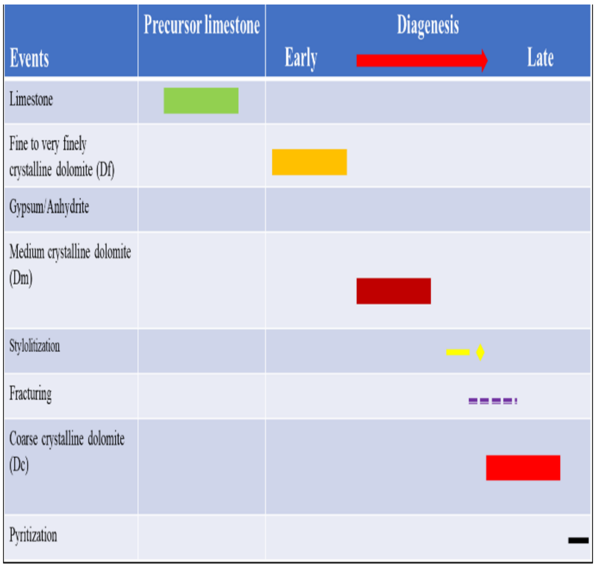

Figure 8. Paragenetic sequence of different types of the dolomite of Eocene Chorgali Formation

10. CONCLUSION

Based on detailed field observations and microscopic examinations along with XRD analysis, SEM results, and Isotopic data of representatives taken from the dolomites of the studied formation mentioned below conclusion can be made;

During field studies the presence of well-preserved cyanobacterial mat, lamination, mud-cracks, horizontal burrows, and anhydrite nodules with chicken wire structures were observed in the dolomites of Chorgali Formation

The petrographic studies observed relics of the pre-existing textures with the presence of gypsum flakes in Df. Moreover, Dm is destructive in character with the presence of stylolites, whereas Dc is fractures associated. Based on Petrographic characteristics three types of dolomites are identified which contain Df (fine crystalline dolomite), D. II (medium crystalline dolomite), and Dc (coarse crystalline dolomite).

XRD study revealed Df as non-stoichiometric low ordered dolomite, while Dm and Dc are stochiometric ordered dolomites.

SEM results showed a low concentration of Mg, Ca, O, Na, Si, and Fe in Df, and High concentrations of Mg, Ca, and O are observed in Dm and Dc.

Stable isotopes data exhibits slight depletion δ18O values for Df, whereas Dm and are highly depleted representing the elevated temperature at depth. Further, δ13C values of Df, Dm, and Dc lie in the marine signatures range.

The above studies revealed that fine crystalline dolomites (Df) are formed near-surface conditions during the early stage of diagenesis, whereas medium crystalline dolomite (Dm) and coarse crystalline dolomite (Dc) are formed at depth with elevated temperature.

Acknowledgement

The author is grateful to Geoscience Advance Research Laboratories, Geological Survey of Pakistan Islamabad, and PINTECH for providing access to Laboratory facilities.

Author Contributions

Sajjad Khan: Conceptualization, Methodology, Software, Data curation, Writing-Original draft preparation. **Mehboob ur Rashid**: Visualization Supervision, Writing-Reviewing and Editing.

Conflicts of Interest

The authors declare no conflict of interest.

References

Amthor, J.E., & Friedman, G.M. (1991). Dolomite-rock textures and secondary porosity development in Ellenburger Group carbonates (Lower Ordovician), west Texas and southeastern New Mexico. *Sedimentology*, 38(2), 343-362.

Awais, M., Hanif, M., Khan, M.Y., Jan, I.U., & Ishaq, M. (2019). Relating petrophysical parameters to petrographic interpretations in carbonates of the Chorgali Formation, Potwar Plateau, Pakistan. *Carbonates and Evaporites*, 34(3), 581-595.

Baker, D.M. (1987). Balanced Structural Cross-section of Central Salt Range and Potwar Plateau of Pakistan, shortening and overthrust deformation, (MS Thesis), Oregon State University, Corvallis.

Benchilla, L., Swennen, R., Akhtar, K., & Roure, F. (2002a). Sedimentology and diagenesis of the Chorgali Formation in the Potwar Plateau and Salt Range, Himalayan foothills (N-Pakistan). AAPG Search and Discovery Article, *AAPG Hedberg Conference*, May 14-18, 2002, Palermo - Mondello, Sicily, Italy

Benchilla, L., Swennen, R., Roure, F., Akhtar, K., & Jaswal, T.M. (2002b). Fluid circulation and diagenesis of carbonate reservoirs in foreland fold-and-thrust belts: a case study of the Salt Range-Potwar Basin (N-Pakistan). *American Association of Petroleum Geologists Annual Meeting*, Houston.

Chatterjee, S., & Scotese, C.R. (1999). The breakup of Gondwana and the evolution and biogeography of Indian plate. *Proceedings-Indian National Science Academy*, 65(3), 397-426.

Chatterjee, S., & Scotese, C.R. (2010). The wandering Indian plate and its changing biogeography during the Late Cretaceous-Early Tertiary period. In New Aspects of Mesozoic Biogeography Springer, Berlin, Heidelberg.

Chatterjee, S. (1992). A kinematic model for the evolution of the Indian plate since the Late Jurassic. *New Concepts in Global Tectonics*, 33-62.

Chatterjee, S., Goswami, A., & Scotese, C.R. (2013). The longest voyage: Tectonic, magmatic, and paleoclimatic evolution of the Indian plate during its northward flight from Gondwana to Asia. *Gondwana Research*, 23(1), 238-267.

Duggan, J.P., Mountjoy, E.W., & Stasiuk, L.D., (2001). Fault-controlled dolomitization at Swan Hills Simonette oil field (Devonian), deep basin west-central Alberta, Canada. *Sedimentology*, 48(2), 310-323.

Fabricius I.L., & Borre M.K. (2007). Stylolites, porosity, depositional texture, and silicates in chalk facies sediments. Ontong Java Plateau-Gorm and Tyra fields, North Sea. *Sedimentology* 54, 183– 205.

Feng, M., Wu, P., Qiang, Z., Liu, X., Duan, Y., & Xia, M. (2017). Hydrothermal dolomite reservoir in the Precambrian Dengying Formation of central Sichuan Basin, Southwestern China, *Marina and Petroleum Geology*, 82, 206-219.

Gasparrini, M., Bakker, R.J., Bechstadt, T., & Boni, M. (2003). Hot dolomites in a Variscan foreland belt: hydrothermal flow in the Cantabrian Zone (NW Spain). *Journal of Geochemical Exploration,* 78, 501-507.

Gregg, J.M., & Shelton, K.L. (1990). Dolomitization and dolomite neomorphism in the back reef facies of the Bonneterre and Davis formations (Cambrian), Southeastern Missouri. *Journal of Sedimentary Research*, 60(4), 549-562.

Gregg, J.M., & Sibley, D.F. (1984). Epigenetic dolomitization and the origin of xenotopic dolomite texture. *Journal of Sedimentary Research*, 54(3), 908-931.

Guo, C., Chen, D., Qing, H., Dong, S., Li, G., Wang, D., Qian, Y., & Liu, C. (2016). Multiple dolomitization and later hydrothermal alteration on the Upper Cambrian-Lower Ordovician carbonates in the northern Tarim Basin. China. *Marine and Petroleum Geology*, 72, 295-316.

Illing, L.V, Wells, A.J., & Taylor, L. (1965) Penecontemporaneous dolomite in the Persian Gulf. In Pray, L.C., and Murray, R. C. (eds) Dolomitization and Limestone diagenesis, SEPM Spec. Publication, 13, 89-111.

Jaswal, T.M., Lillie, R.J., & Lawrence, R.D. (1997). Structure and evolution of the northern Potwar deformed zone, Pakistan. *Advancing the World of Petroleum Geosciences*, 81(2), 308-328.

Jurgan, H. & Abbas, G. (1991). On the Chorgali Formation at the type locality. *Pakistan Journal of Hydrocarbon Research,* 3(1), 35-45.

Kadri, I.B. (1995). Petroleum geology of Pakistan. Pakistan Petroleum Limited, Karachi. Ferozsons (pvt) Limited, 275.

Kazmi, A.H., & Rana, R.A., (1982). Tectonic Map of Pakistan, Geological Survey of Pakistan, Quetta, p1.

Land, L.S. (1985). The origin of massive dolomite. Journal of Geological Education, 33(2), 112-125.

Lee, T.Y. & Lawver, L.A. (1995). Cenozoic plate reconstruction of Southeast Asia. *Tectonophysics*, 251(1-4), 85-138.

McKenzie, D., & Sclater, J.G. (1971). The evolution of the Indian Ocean since the Late Cretaceous. *Geophysical Journal International*, 24(5), 437-528.

McKenzie, J.A. (1981). Holocene dolomitization of calcium carbonate sediments from the coastal sabkhas of Abu Dhabi, UAE: a stable isotope study. *The Journal of Geology*, 89(2), 185-198.

Mitchell, J.T., Land, L.S. & Miser, D.E. (1987). Modern marine dolomite cement in a north Jamaican fringing reef. *Geology*, 15(6), 557-560.

Mountjoy, E.W., Machel, H.G., Green, D., Duggan, J., & Williams-Jones, A.E., 1999. Devonian matrix dolomites and deep burial carbonate cements: a comparison between the Rimbey Meadowbrook reef trend and the deep basin of west-central Alberta. *Bulletin of Canadian Petroleum Geology*, 47, 487–509.

Mujtaba, M. (2001). Depositional and diagenetic environments of carbonates of Chorgali Formations (Early Eocene) Salt Range-Potwar Plateau, Pakistan. (Ph.D. Thesis) University of Punjab.

Mujtaba, M., Jurgan, H., & Abbas, G. (1989). Depositional environment and porosity development in Lower Eocene Limestone Formation of Surghar Range. Pakistan, HDIP International Report (unpublished), Salt Range and Potwar Basin.

Patriat P., & Achache, J. (1984). India-Eurasia collision chronology has implications for crustal shortening and driving mechanism of plates. *Nature*, 311(5987), 615-621.

Patterson, R.J., & Kinsman, D.J.J. (1982). Formation of diagenetic dolomite in coastal sabkha along Arabian (Persian) Gulf. *American Association Petroleum Geologist*, 66(1), 28-43.

Powell, C.M. & Conaghan, P.J. (1973). Plate tectonics and the Himalayas. *Earth and Planetary Science Letters*, 20(1), 1-12.

Powell, C.M., Roots, S.R., & Veevers, J.J. (1988). Pre-breakup continental extension in East Gondwanaland and the early opening of the eastern Indian Ocean. *Tectonophysics*, 155(1-4), 261-283.

Rahimi, A., Adabi, M.H., Aghanabati, A., Majidifard, M. R., & Jamali, A.M. (2016). Dolomitization mechanism based on petrography and geochemistry in the Shotori Formation (Middle Triassic), Central Iran. *Open Journal of Geology*, 6(9), 1149-1168.

Rosenbaum, J., & Sheppard, S.M.F. (1986). An isotopic study of siderites, dolomites and ankerites at high temperatures. *Geochimica et cosmochimica acta*, 50(6), 1147-1150.

Saller, A.H. (1984). Petrologic and geochemical constraints on the origin of subsurface dolomite, Enewetak Atoll: An example of dolomitization by normal seawater. *Geology*, 12(4), 217-220.

Shah, S.I., & Khan, I. (2016). Lexicon of the Stratigraphy of Pakistan. Geological Survey of Pakistan, Memoir 23.

Shah, S.M.I. (2009). Stratigraphy of Pakistan, Geological Survey of Pakistan, Memoir 22.

Sibley, D.F., & Gregg, J.M. (1987). Classification of dolomite rock textures. *Journal of sedimentary Research*, 57(6), 967-975.

Wachter, E.A., & Hayes, J.M. (1985). Exchange of oxygen isotopes in carbon dioxide-phosporic acid systems. *Chemical Geology: Isotope Geoscience Section*, 52(3-4), 365-374.

Warren, J.K. (2000). Dolomite: occurrence, evolution and economically important association. *Earth Science Reviews*, 52, 1-81.

Warren, J.K. (2006). Evaporites: sediments, resources and hydrocarbons. Springer Science & Business Media.

Zenger D.H. (1983). Burial dolomitization in the Lost Burro Formation (Devonian), East-Central California, and the significance of the diagenetic dolomitization. *Geology*, 11(9), 519-522.

TURKGEO
TURKISH JOURNAL OF GEOSCIENCES

ISSN: *2717-7696*
Research Article
Vol; 3, Issue; 1, pp. 22-29, 2022
DOI: *10.48053/turkgeo.1114813*
Journal homepage:
https://dergipark.org.tr/en/pub/turkgeo

Investigation of the effects of different flight parameters on the accuracy of DEM generated using UAV systems

Elif Bulut* [1], **Ferruh Yılmaztürk** [1]

[1]*Aksaray University, Faculty of Engineering, Department of Geomatics Engineering, Aksaray, Turkey*

Keywords
UAV
Orthomosaic
DEM
Rolling Shutter

ABSTRACT

Unmanned Aerial Vehicles (UAVs), can be controlled automatically or with the help of a remote control system, provide high spatial and temporal resolution images in addition to its advantages in terms of cost and time. Due to these features, UAV's have been widely used in studies such as map production, 3D modeling and volume calculation in recent years. In this study, it is aimed to investigate the effects of different flight parameters on the accuracy of Orthomosaic and DEM produced with UAV Systems. In addition, the rolling shutter effect and the use of pre-calibrated and automatic camera calibration parameters were also tested. For this purpose, a total of seven UAV flights were carried out at different heights, overlap ratios, angles and grids at a mining area located within the borders of Aksaray province. Agisoft MetaShape and Pix4D Mapper, which are widely used commercial software, were used to process the UAV images. In this study, 27 points were established and 3D coordinates of these points were measured using GNSS technique. 15 of these points were used as reference points and the remaining 12 points were used as check points. Accuracy analysis was performed by comparing the produced Orthomosaics and DEMs with the check points in the study area. CloudCompare and ArcGIS software were used in the comparison of the products as a result of the evaluation of the images. It is concluded that the Orthomosaics produced using 45^0 angle and DEMs with 60^0 angle has higher accuracy than the others. Point clouds and DEMs' produced using automatic and pre-calibrated camera calibration parameters show that the pre-calibrated images provide higher accuracy. Also, it is seen that when the rolling shutter effect is modeled, the horizontal and vertical accuracy is increased in all three flights with different flight parameters in this study.

1. INTRODUCTION

Unmanned Aerial Vehicle (UAV), whose usage area has become more and more widespread in recent years; It is an aircraft that does not physically have a pilot or a passenger, can only carry measurement equipment such as a camera, laser scanning device, video camera, GNSS (Global Navigation Satellite System) and completes its flight automatically or remotely (Döner et al., 2014). Today, UAV platforms have become an important data source that allows inspection, surveillance and analysis for different disciplines and different application areas in photogrammetric data production (Psirofonia et al., 2017; Makineci and Karasaka, 2021). The use of UAVs for civilian purposes, which were primarily developed for military purposes, has been after the Second World War with the development of technology, and the first and most important regulation of air transportation was signed as a result of the Chicago Conference in 1944 and includes regulations related to civil aviation (Coşkun, 2020). In Turkey, legal regulations regarding UAVs were prepared by the General Directorate of Civil Aviation on February 22, 2016 (SHT-FCL, 2019).

With the developing photogrammetric sensor, platform and remote sensing technologies, UAV has become an increasingly common platform, as it provides low cost, high spatial and temporal resolution opportunities compared to conventional aerial photogrammetry (Akay and Özcan 2017; Şasi

---

* **Corresponding Author**

*(elifbuluut06@gmail.com) ORCID ID 0000-0002-4870-4395
(yilmazturk@aksaray.edu.tr) ORCID ID 0000-0002-8347-664X

Cite this article

Bulut E., & Yılmaztürk F. (2022). Investigation of the effects of different flight parameters on the accuracy of DEM generated using UAV systems. Turkish Journal of Geosciences 3(1), 22-29.

Received: 10/05/2022; Accepted: 23/05/2022

and Yakar 2018). Today, although UAVs usage for military, security and intelligence purposes still continues, since they can be easily used for civilian purposes and to reach up-to-date data fast and more economical way, they make important contributions to disciplines such as geomatic, mining, geology, civil and environmental engineering, and are also widely used for scientific purposes. UAVs; used in many technical areas such as in cartography (Orthomosaic production, digital terrain model (DTM), digital elevation model (DEM), excavation-filling calculations, area-volume calculations, etc.), observing environmental change, monitoring of weather conditions, observation of coast and coastline, detection of mining areas, agricultural applications (land classification, soil analysis, determination of crop productivity), monitoring of natural disasters, archaeological studies, architecture and landscape studies, 3D city modeling, city silhouettes and hobby areas such as creating movies, filming and sports activities (Çömert et al., 2012; Coşkun, 2020; Makineci et al., 2020a; Makineci et al., 2021).

Three-dimensional object/surface model of the ground, DEM and orthomosaics produced by UAVs are used in various studies (Ozcan and Akay, 2018; Ulvi and Toprak, 2016). The development in the field of photogrammetry led to the emergence and development of the concept of 'Digital Photogrammetry' in the early 1990s as a continuation of analog and analytical photogrammetry. In this process, vector contour lines and DEMs with higher quality and resolutions have replaced the contour lines on the printed topographic maps. DEM, which is defined as the digital representation of topography, is a suitable structure to show the constantly changing topographic surface of the earth (Gündoğdu, 2003). The fact that three-dimensional models, DEMs and orthomosaics that can be obtained quickly from UAVs are a general data source for hydrological, geomorphological and other three-dimensional applications and the widespread use of digital topographic data reveals the importance of these data (Moore et al., 1991; Thomson et al., 2001; Makineci and Karabörk, 2016; Karabörk et al., 2021).

As DEMs are a stand-alone product, DEMs produced are also used in geodetic and photogrammetric data collection, editing and correction, Orthomosaic production, and topographic map production (Erdoğan and Toz, 2009). With the produced DEM data, volumetric change analyzes can be evaluated in terms of temporal and spatial, in addition, length and area calculations of the surface and temporal change analyzes can be performed with high accuracy with orthomosaics and three-dimensional object/surface model data (Moore et al., 1993; Eltner et al., 2017; Rusnák et al.,2018; Akay et al., 2021).

Within the scope of this study, it is aimed to determine the effects of flight heights, camera angles, overlap ratios and grid sizes on the accuracy of orthomosaics and DEMs produced by UAV photogrammetry. In addition to that, the effect of rolling shutter and pre-calibrated camera calibration parameters were tested in different flights within the scope of this study.

2. MATERIAL and METHOD

2.1 Study area

Within the scope of this study, an open mine of approximately 15 hectares was selected as a study area in the town of Ortaköy, Hacımahmutuşağı (E:38^{o} 44', B:33^{o} 56'), located approximately 40 km northeast of Aksaray city (Figure 1). The determined area is a marble area and there are cut and filling sections. In the area chosen as the study area, the elevation values vary between 1409 m and 1444 m, and the height differences are approximately 35 meters.

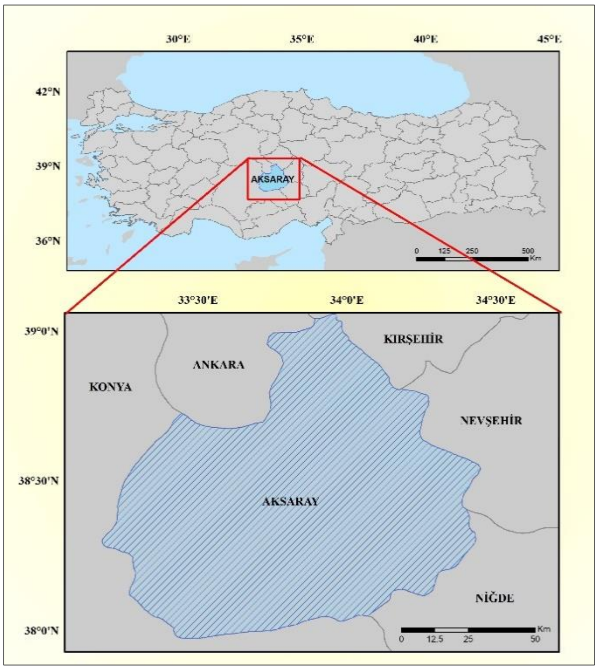

Figure 1. Study area

The absence of wooded areas and high voltage lines in the study area provided convenience in UAV measurements. In the marble field selected as the study area, there are 662812.5 m^3 filling area, 69511.14 m^3 splitting area, 9107,322 m^2 stock area, 17103 m^2 factory area and 173.171 m^2 construction site.

2.2 Establishment of Ground Control Point (GCP)

GCPs homogeneously distributed over the work area are needed in order to calculate the interior and exterior directions of the photographs taken by the UAV, to test the accuracy of the outputs to be produced, and to define them in a reference system. GCPs are established in areas where the topography changes rapidly (>50m), with a maximum distance of 250 m between the points. Twenty-seven GCPs established in the study area were measured using a dual frequency CHC-I80 GNSS receiver with Network-RTK method in ITRF96 datum in UTM 33-3 coordinate system. In addition, twelve points selected homogeneously from twenty-seven GCPs were used as check points in the image processing steps.

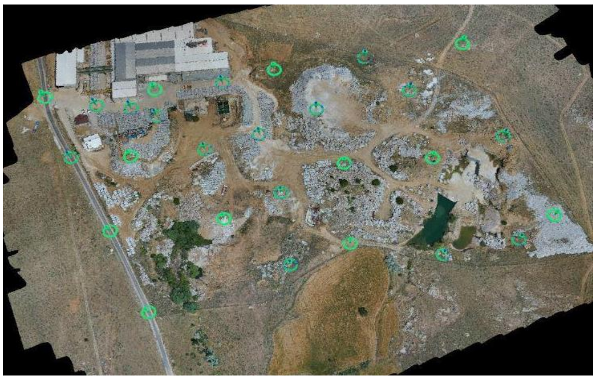

Figure 2. Location of the GCPs in the study area

In order to increase the visibility in the photographs obtained by using the UAV, the control points were prepared as a light and 20 × 20 cm square on a dark background and a rectangle with a width of 20 cm and a length of 40 cm, 20 cm away from the square (Figure 3). GCPs have been installed in open areas and care has been taken to ensure that there are no obstacles such as buildings or trees within this cone of vision.

Figure 3. Example of the GCPs established in the study area

2.3 UAV Flights

Within the scope of the study, Mavic II UAV was used for point cloud, DEM and orthomosaic production by performing UAV flights with different altitude, angle, overlap ratios, single and double grid (DG).

During the preparation stage before the flight, the settings of the camera integrated into the UAV were made, the path to be followed by the UAV within the working area boundaries was determined, and the images of the working area were obtained by performing the flights according to the previously determined flight plans. In addition, all flights in the study area were completed on the same day to minimize the sunlight effect (Öztürk et al., 2017; Akay et al., 2021). The properties of the images taken at different angles, heights and overlap ratios of the study area are shown in the Table 1.

Table 1. Flight parameters and number of images used in the study

Flight No.	Altitude (m)	Overlap ratio	Angle (°)	Num. of images
1	120	%80 %60	90	123
2	100	%90 %70	90	456
3	100	%80 %60	90	171
4	100	%80 %60 (DG)	90	527
5	100	%80 %60	45	400
6	100	%80 %60	60	236
7	Free flight			169

As a result of 7 UAV flights carried out with different parameters in the study area, approximately 2,000 images were taken.

2.4. Image processing and validation

There is many software for photogrammetric evaluation of high resolution images obtained from UAVs. However, evaluating a large number of images obtained using UAVs with classical photogrammetric approach software is a time-consuming and difficult task. For this reason, as a result of the developing technology, more advanced software has been used in recent years. In the process of UAV images, using the Structure from Motion (SfM) algorithm, high resolution point clouds, DEMs and orthomosaics are produced from consecutive serial photographs (Akay et al., 2021). Classic photogrammetry techniques require high-precision 3D position and orientation parameters of the camera and GCPs in order to create a geometric model. However, in SfM algorithm, model geometry, camera position and orientation parameters are solved simultaneously and automatically (Atak, 2018).

The SfM method ensures that the photos obtained with UAVs are matched according to the characteristics of the objects in the photos by arranging the camera parameters and their positions. First of all, a low-density point cloud is produced with the objects matched in the photographs, and dense point cloud is produced by compacting the points in the less-dense point cloud data. Mesh, DEM and orthomosaic productions are performed on the dense point cloud, respectively (Snavely et al., 2008). In this study, Pix4D Mapper and Agisoft Metashape software were used to evaluate the obtained images and produce point clouds, orthomosaics and DEMs. During the preliminary evaluation processes, camera calibration and external orientation parameters are calculated using the SfM algorithm, and these orientation parameters were used as input parameters in the production of the outputs. In addition, Cloud Compare and ArcGIS software were used for the compare the generated photogrammetric products with GNSS points.

Camera calibration is more common today due to the widespread use of digital cameras and their use in the field of computer vision along with photogrammetry. In the past decades, while all of the calibration process steps were done manually, many process steps such as creating the calibration field and calculations are done automatically with the advanced software used today. The accuracy of camera calibration directly affects the process of extracting accurate information from photographs and producing reliable 3D models. For this reason, it is aimed to be done with the highest possible accuracy (Özdemir ve Duran, 2017). In this study, in addition to investigating the effect of different flight parameters of the produced photogrammetric outputs, in order to determine the effect of camera calibration parameters on the produced point cloud and DEM, first of all, the images of Flight 3 (Table 1) were evaluated in Agisoft MetaShape software and the camera calibration parameters were obtained automatically. Afterwards, camera calibration parameters were determined as a result of photogrammetric triangulation using images of flights at different heights (120m, 100m and free flight) and then, these calibration parameters were used as pre-calibrated values.

In the validation step, horizontal and vertical root mean square error (RMSE) of the orthomosaics and DEMs' calculated using Equation 1 and 2 given below as;

$$\mu_{xy} = \sqrt{\frac{\mu_x^2+\mu_y^2}{2}} \qquad (1)$$

$$\mu_z = \sqrt{\frac{\sum \Delta z_i^2}{n_z}} \qquad (2)$$

Where, Δz is the difference between reference coordinates of check points and calculated coordinates of check points, n_z is the number of check points used. Adjustment results of the flights obtained through Pix4d Mapper quality reports.

In point cloud comparison, CloudCompare and coordinates of the GNSS points was used to obtain mean distances and standard deviations (std.) between products. First of all, the point cloud to be compared and the point file or other model to be compared with this point cloud are imported into the software regarding the same coordinate frame. After both data are imported, first the approximate distances and then the signed distance and standard deviation values can be calculated over the software interface. As a result of these steps, histograms and bars reflects the difference between products can be produced according to the user's request.

In the DEM comparison, ArcGIS' "raster calculator" tool was used to extract elevation values from DEMs and match all these values with GNSS points. After that, vertical rms values of DEMs' are calculated using Equation 2.

In particular, cameras that are integrated with commercial UAVs and cannot be separated are generally low-cost and low-power sensors are used. These cameras cause a disadvantage called rolling shutter. This effect distorts the images of moving objects, causing the entire image not to be perceived at the same time (Ait-Aider, et al., 2006). The effect in question increases even more when the UAV is exposed to more vibration, so it is not suitable to fly especially in heavy wind conditions. The rolling shutter effect is a compelling reason for creating 3D models of moving objects. Even if the displayed object or area is stationary, the fact that the UAV is in motion still causes this effect (Vautherin, et al., 2016). However, the latest developments in the SfM software used allow to obtain sufficient accuracy with these cameras by modeling this effect (Raczynski, 2017). Therefore, in order to reveal the impact of the rolling shutter effect on the images, this effect was tested using flights with different heights and grid ratios within the scope of this study (Table 4).

3. RESULTS and DISCUSSION

The orthomosaics and adjustment results of the quality reports, obtained as a result of the evaluation process of the study using Pix4d Mapper were compared with the coordinates of 12 check points measured using GNSS technique, and their horizontal and vertical accuracies were obtained (Table 2). Then, "raster calculator" tool of ArcGIS software was used to calculate the differences of the DEMs' and 12 check points measured with GNSS and results of these analysis is also given in Table 2. In addition to the 7 flights were performed in the study area within the context of this study, 60^0 and 90^0 angled flights with 100 m and 80x60 overlapping ratio were combined together and re-evaluated. The results from this re-created flight obtained as a result of the accuracy analysis in both horizontal and vertical components with rms values are presented in Table 2. Also, point clouds that produced from images with different flight parameters processed in Pix4D Mapper software were compared using CloudCompare with the coordinate values obtained from 1300 points measured using Network-RTK GNSS technique in the study area (Table 3).

Table 2. Position accuracy of photogrammetric products produced using different flight parameters

Flight Parameters				**Orthomosaic (cm)**	**Adjustment results**			**DEM (cm)**
FN	Altitude (m)	Overlap (%)	Angle (°)	RMS XY	RMS X	RMS Y	RMS Z	RMS Z
1	100	80x60	90	2.30	1.63	2.83	4.60	5.30
2	100	80x60 DG	90	2.03	1.69	2.32	4.39	5.84
3	100	80x60	45	1.52	1.68	1.32	3.06	5.27
4	100	80x60	60	1.82	1.38	2.17	3.93	3.87
5	100	90x70	90	1.49	1.33	1.61	4.14	5.42
6	120	80x60	90	1.94	1.23	2.45	3.24	5.86
7	100	80x60	60-90	1.67	1.63	1.69	3.45	4.84

When the Table 2 is examined, it is seen that the orthomosaics produced from using 90x70 overlap ratio gives the best results in orthomosaics. Also, results of the flight of 45^0 angle are close to 90x70 overlap ratio results with only a difference about 3 mm. In Table 2, values in the quality report of the adjustment results of the flights indicate that, flight 3 with the 45^0 angle images used while processing has higher accuracy than the others in both Y and Z component. When the rms values obtained by comparing the DEMs with the 12 check points are examined in Table 2, it is seen that unlike the orthomosaic and quality reports, the DEM produced from photographs 60^0 angle flight, gives better results than the DEM produced from photographs taken at a 45^0 and 60^0-90^0 angle and other flight parameters.

When the results obtained from this study are compared with similar studies in the literature, in Öztürk et al., (2017), orthomosaics produced from photos taken at a 45^0 angle were found to have higher accuracy. In this respect, the results obtained from the two studies are in agreement. When the accuracy values of the DEM are examined, it is seen that the accuracy decreases as the flight altitude increases and more accurate results are obtained as the overlap ratio decreases. In addition, the results obtained from this study are compatible with the results obtained from other studies (Mesas-Carrascosa et al., 2016; Akay et al., 2019; Şenkal, 2018) evaluated according to height and overlap ratio.

Table 3. Accuracy comparison of the point clouds with different flight parameters

Flight Parameters				**Point clouds (cm)**
FN	Height (m)	Overlap (%)	Angle (°)	Mean distances
1	100	80x60	90	8.40
2	100	80x60 DG	90	5.91
3	100	80x60	45	5.20
4	100	80x60	60	7.13
5	100	90x70	90	5.93
6	120	80x60	90	7.11
7	100	80x60	60-90	9.33

When the mean distances of the point clouds given in Table 3 are examined, it is seen that the point cloud produced from the photographs with an angle of 45^0 has higher accuracy than others. Considering only the overlap ratios, it is seen that the 90x70 overlap ratio gives the best results in point clouds. When only the height parameter was changed, it was concluded that the point cloud produced from the photographs taken from 120 m had higher accuracy. When the all accuracy values obtained as a result of single and double grid flights are examined, it is seen that double grid gives significantly better results in point clouds. When all parameters are evaluated together, it is seen that the point cloud produced from photographs with an angle of 45^0 gives the best result.

To reveal the influence of the camera calibration parameters on photogrammetric products such as point cloud and DEM, images obtained from Flights 2, 6 in Table 2 and free flight were combined together and evaluated using Agisoft MetaShape software (Kılınç-Kazar et al., 2022; Sağdıç et al., 2022). Using the images of these flight, camera calibration parameters, the focal length (f) and the calibrated focal length (c) were calculated and these values were fixed during the re-evaluation of the 1st flight and comparisons were made on the generated point cloud and DEM. Point clouds and DEMs' produced using automatic and pre-calibrated camera calibration parameters were compared with the 1300 points measured using the GNSS technique, and the calculated distances and rms values between them were shown in Table 4.

Table 4. Comparison of the camera calibration parameters

	Point Cloud		DEM
Calibration parameters	Mean Distance (cm)	std. deviation (cm)	rms (cm)
Automatic	8.40	12.60	5.3
Pre-calibrated	7.70	12.60	3.4

When mean distances and rms values that given in Table 4 is examined, it is seen that the differences in automatic calibration and pre-calibrated values reaching 1 cm. For this reason, it is clearly seen that in both point cloud and DEM gives better result when the images are pre-calibrated. Therefore, like other studies in the literature (Raczynski, 2017; Özdemir and Duran, 2017; Makineci et al., 2020b) performing pre-calibration before producing 3D models and other photogrammetric products is necessary.

A rolling shutter camera is used in the UAV used in this study. For this reason, images are obtained row by row and the entire image is not recorded at the same time. Therefore, this effect needs to be modeled. In Table 5, the results obtained when the rolling shutter effect of 3 flights, whose flight parameters are given below, is modeled and not modeled using Agisoft MetaShape.

Table 5. Results of the rolling shutter effect

Flight Param.	Model	X error (cm)	Y error (cm)	Z error (cm)	Total (cm)	Image (pix)	rms Z in DEM (cm)
100m 80x60	Without rs	2.61	1.92	6.70	7.44	0.81	5.30
	With rs	1.99	2.03	6.18	6.80	0.81	4.36
120 m 80x60	Without rs	3.29	2.83	6.22	7.59	0.52	5.86
	With rs	3.27	2.82	6.22	7.57	0.52	2.28
100m DG	Without rs	3.17	1.81	4.60	5.88	0.80	5.84
	With rs	2.07	1.55	4.49	5.18	0.70	5.41

Error values given in Table 5 are examined, it is seen that the errors of the check points decrease when the rolling shutter effect is modeled in all 3 flights. Although there are no significant changes in the horizontal and vertical directions in the images taken from a height of 120 meters, it is seen that this effect reaches values up to 1 cm in the x component and 0.5 cm in the vertical direction in the flights using 100 meters' height, 80x60 overlapping ratio and double grid. When the height component rms of DEMs' are examined that given in Table 5, it is seen that modelling the rolling shutter effect has a positive effect on the results.

4. CONCLUSIONS

In this study, firstly, photogrammetric products (Orthomosaic and DEM) generated by using images obtained with different height, angle and overlap ratios in a mining area in Aksaray province were compared in terms of accuracy. As a result of the comparisons made by considering different parameters, it was seen that, in orthomosaics, images taken at an angle of 45^0 were more accurate, and in DEMs, images evaluated with 60^0 angle flight give the best results. It is thought that the reason for this is that the sun's rays are suitable with the photo angle and that more data is produced in the outputs produced using the oblique shooting angle compared to the vertical image shooting angle. When the overlap ratios and grid sizes are compared with each other, it was seen that the orthomosaics, produced from the larger overlap ratio and double grid were more accurate than the others, while the situation is the opposite for DEMs.

Also, point clouds that produced from images with different flight parameters were compared with the coordinate values obtained from 1300 points measured using Network-RTK GNSS technique in the study area and it is seen that the point cloud produced from photographs with an angle of 45^0 gives the best result when all parameters are evaluated together.

In addition, within the scope of the study, the effect of camera calibration parameters on photogrammetric products such as point cloud and DEM was investigated. According to the findings of this study, it is clearly seen that better results are obtained in both point cloud and DEM when pre-calibration is performed on the images obtained using UAV systems.

Also, an another investigation was carried out to determine the effects of rolling shutter camera-based errors on different flight parameters due to the fact that the UAV used in the study has a rolling shutter camera. According to the findings of this study, it was observed that better results were obtained when the rolling shutter effect was modeled in all flights with different flight heights and grid sizes. For this reason, according to the results obtained from this study, it was concluded that this effect should be modeled in studies performed with UAV systems that using mostly rolling shutter cameras.

Acknowledgement

This article was produced from Elif BULUT's master's thesis.

Author Contributions

Elif Bulut: Conceptualization, Data curation, Methodology, Software, Writing-Original draft preparation. **Ferruh Yilmaztürk:** Supervision, Methodology, Writing, Reviewing and Editing.

Conflicts of Interest

The authors declare no conflict of interest.

REFERENCES

Ait-Aider, O., Andreff, N., Lavest, J.M., & Martinet, P. (2006). Simultaneous object pose and velocity computation using a single view from a rolling shutter camera. In European Conference on Computer Vision, Springer, Berlin, Heidelberg.

Akay S.S., & Ozcan O. (2017). Volumetric Comparison of Uav-Based Point Clouds Generated from Various Softwares*. International Symposium on GIS Applications in Geography and Geosciences*, Çanakkale, Turkey.

Akay, S. S., Özcan, O., Şanlı, F. B., Bayram, B., & Görüm, T. (2019). İHA görüntülerinden üretilen verilerin doğruluk değerlendirmesi, *10. Türkiye Ulusal Fotogrametri ve Uzaktan Algılama Birliği Teknik Sempozyumu*, TUFUAB 2019, 106-110.

Akay, S.S., Ozcan, O., Şanlı, F.B., Bayram, B., & Görüm, T. (2021). Assessing the spatial accuracy of UAV-derived products based on variation of flight altitudes. *Turkish Journal of Engineering*, *5*(1), 35-40.

Atak, H. (2018). Producing orthophoto maps using unmanned air vehicles and accuracy analysis (MSc thesis). Gebze Technical University, Kocaeli, Turkey (in Turkish).

Çömert, R., Avdan, U., & Şenkal, E. (2012). İnsansız Hava Araçlarının Kullanım Alanları ve Gelecekteki Beklentileri. *IV. Uzaktan Algılama ve Coğrafi Bilgi Sistemleri Sempozyumu*, Zonguldak.

Coşkun, E. (2020). Mapping production using unmanned aerial vehicles: Case of Altinordu district of Ordu (MSc thesis). Çukurova University, Adana, Turkey (in Turkish).

Döner, F., Özdemir, S., & Ceylan, M. (2014). İnsansız Hava Aracı Sistemlerinin Veri Toplama Ve Haritalama Çalışmalarında Kullanımı. *Uzaktan Algılama–Cbs Sempozyumu*, 14-17.

Eltner, A., Kaiser, A., Abellan, A., & Schindewolf, M. (2017). Time Lapse Structure-From-Motion Photogrammetry for Continuous Geomorphic Monitoring. *Earth Surface Processes and Landforms*, 42(14), 2240–2253.

Erdoğan, M., & Toz, G. (2009). Sayısal Yükseklik Modeli (Sym) Doğruluk ve Üretim Maliyetleri. *Türkiye Ulusal Fotogrametri ve Uzaktan Algılama Birliği Sempozyumu* TUFUAB 2009.

Gündoğdu, K.S. (2003). Sayısal Yükseklik Modellerinin Arazi Boy Kesitlerinin Çıkarılmasında Kullanımı, *Uludağ Üniversitesi Ziraat Fakültesi Dergisi*, 17, 149-157.

Karabörk, H., Makineci, H.B., Orhan, O. & Karakus, P. (2021). Accuracy assessment of DEMs derived from multiple SAR data using the InSAR technique. *Arabian Journal for Science and Engineering*, 46(6), 5755-5765.

Kılınç-Kazar, G., Karabörk, H., & Makineci, H.B. (2022). Evaluation of Test Field-based Calibration and Self-calibration Models of UAV Integrated Compact Cameras. *Journal of the Indian Society of Remote Sensing*, 50(1), 13-23.

Makineci H.B., & Karasaka L. (2021). Investigation of 3D models acquired with UAV oblique images. *Turkish Journal of Geosciences*, 2(2), 13-20.

Makineci, H.B., & Karabörk, H. (2016). Evaluation digital elevation model generated by synthetic aperture radar data. *International Archives of the Photogrammetry, Remote Sensing and Spatial Information Sciences*, 1, 57-62.

Makineci, H.B., Karabörk, H., & Durdu, A. (2020a). The Performance Evaluation of Image Matching Techniques within UAV Images. *Turkish Journal of Geosciences*, 1(1), 8-14.

Makineci, H.B., Karabörk, H., & Durdu, A. (2021). ANN estimation model for photogrammetry-based UAV flight planning optimisation. *International Journal of Remote Sensing*, 1-23.

Makineci, H.B., Karasaka, L., & Şahin, D. (2020b). Fotogrametrik Amaçlı Kamera Kalibrasyonu Yazılımlarının Kullanımı Üzerine Bir Araştırma. *Türkiye Fotogrametri Dergisi*, 2(1), 14-21.

Mesas-Carrascosa, F.J., Notario García, M.D., Meroño de Larriva, J.E., & García-Ferrer, A. (2016). An analysis of the influence of flight parameters in the generation of unmanned aerial vehicle (UAV) orthomosaicks to survey archaeological areas. *Sensors*, 16(11), 1838.

Moore, I.D., Gessler, P.E., Nielsen, G.A.E., & Peterson, G.A. (1993). Soil attribute prediction using terrain analysis. *Soil science society of america journal*, 57(2), 443-452.

Moore, I.D., Grayson, & R.B., Ladson, A.R. (1991). Digital Terrain Modeling: a Review of Hydrological, *Geomorphological and Biological Applications, Hydrological Processes*, 5 (1), 3-30.

Ozcan, O., & Akay, S.S. (2018). Modeling Morphodynamic Processes in Meandering Rivers with UAV-Based Measurements. *International Geoscience and Remote Sensing Symposium*, Valencia, Spain.

Özdemir, E., & Duran, Z. (2017). Sık Kullanılan Kamera Kalibrasyonu Yazılımlarının Karşılaştırılması. *Afyon Kocatepe Üniversitesi Fen ve Mühendislik Bilimleri Dergisi*, 17(4), 1-11.

Öztürk, O., Bilgilioğlu, B. B., Çelik, M. F., Bilgilioğlu, S. S., & Uluğ, R., (2017). İnsanız Hava Aracı (İHA) Görüntüleri İle Ortofoto Üretiminde Yükseklik

Ve Kamera Açısının Doğruluğa Etkisinin Araştırılması. *Geomatik*, *2*(3), 135-142.

Psirofonia, P., Samaritakis, V., Eliopoulos, P., & Potamitis, I. (2017). Use of Unmanned Aerial Vehicles for Agricultural Applications with Emphasis on Crop Protection: Three Novel Case-studies. *International Journal of Agricultural Science and Technology*, 5(1), 30-39.

Raczynski, R.J. (2017). Accuracy analysis of products obtained from UAV-borne photogrammetry influenced by various flight parameters (MSc thesis, NTNU).

Rusnák, M., Sládek, J., Kidová, A., & Lehotský, M. (2018). Template for high-resolution river landscape mapping using UAV technology. *Measurement*, *115*, 139-151.

Sağdıç, Z. S., Makineci, H.B., & Karabörk, H. (2022). Defining The Relationship Between The Diameters of The Points Used in 2D Test Platforms and The Parameters Obtained from Camera Calibration. *International Journal of Environment and Geoinformatics*, 9(3), 108-117.

Şasi, A., & Yakar, M. (2018). Photogrammetric modelling of Hasbey Dar'ülhuffaz (Masjid) using an unmanned aerial vehicle. *International Journal of Engineering and Geosciences*, 3(1), 006-011.

Şenkal, E. (2018). Accucary analysis of the orthophotos and digital surface models which are produced from images obtained by unmanned aerial vehicle (PhD thesis). Eskişehir Technical University, Eskişehir, Turkey (in Turkish).

SHT-FCL, 2019. http://web.shgm.gov.tr/documents/sivilhavacilik/files/mevzuat/sektorel/talimatlar/2019/SHT-FCL_rev02.pdf

Snavely, N., Seitz, S.M., & Szeliski, R. (2008). Modeling the world from internet photo collections. *International journal of computer vision*, *80*(2), 189-210.

Thompson, J.A., Bell, J.C., & Butler, C.A. (2001). Digital elevation model resolution: effects on terrain attribute calculation and quantitative soil-landscape modeling. *Geoderma*, 100(1-2), 67-89.

Ulvi, A., & Toprak, A.S. (2016). Investigation of ThreeDimensional Modelling Availability Taken Photograph of the Unmanned Aerial Vehicle; Sample of Kanlidivane Church. *International Journal of Engineering and Geosciences*, 1(1), 1-7.

Vautherin, J., Rutishauser, S., Schneider-Zapp, K., Choi, H. F., Chovancova, V., Glass, A., & Strecha, C. (2016). Photogrammetric accuracy and modeling of rolling shutter cameras. *ISPRS Annals of Photogrammetry, Remote Sensing & Spatial Information Sciences*, 3(3).

ISSN: 2717-7696
Research Article
Vol; 3, Issue; 1, pp. 30-38, 2022
DOI: 10.48053/turkgeo.1118373
Journal homepage:
https://dergipark.org.tr/en/pub/turkgeo

Evaluating the performance of algorithms in estimating the Chl-a concentration of Lake Bafa

Elif Kirtiloglu[*1], **Hakan Karabork** [2]

[1]Konya Technical University, Graduate Education Institute, Konya, Turkiye
[2]Konya Technical University, Faculty of Engineering and Natural Sciences, Geomatic Engineering, Konya, Turkiye

Keywords
Chlorophyll-a
Inland water bodies
Cyanobacteria
Water quality
Sentinel 2
Remote Sensing

ABSTRACT

Monitoring and estimating pigment concentrations in water bodies have a critical role in early intervention or investigation of causes for prevention. Remote sensing data are the most effective alternative due to its advantages as effortless, requiring less labor, and displaying large areas in a single frame. Analyzing and estimating Chlorophyll-a (Chl-a) concentrations constitute the most important research topics in water bodies because all phytoplankton contain Chl-a. In this study, we evaluated the performance of algorithms in estimating the Chl-a concentration of Lake Bafa based on Sentinel 2 bands which are simulated from in-situ reflectance data. We used 1/R665xR705, 1/R665-1/R705, (1/R665-1/R705) x R740, R705/(R560+R665), so called M09, G09-2B, G09-3B, K07, respectively and Normalized Difference Chlorophyll Index (NDCI) algorithms for evaluation. Water samples and in-situ measurements were collected and obtained in two field campaigns. Bands of Sentinel 2 were then simulated from in-situ reflectance data and used to calibrate and validate models for Chl-a estimation. R^2 values of 0.679, 0.749, 0.395, 0.726, and RMSE values of 0.7 and 1.882, 1.663, 1.737, and 1.818 µg/L have been obtained for M09, G09-2B, G09-3B, K07, and NDCI algorithms, respectively. Sentinel 2 images have been used for map validation. Our results show that M09 and NDCI algorithms performed better in estimating Chl-a compared to the other three algorithms for our data range at Lake Bafa.

1. INTRODUCTION

The estimations of biologists showed that the total biomass of phytoplankton is less than one billion tones in the ocean at any one time. It is less than 1% when compared to all photosynthetic biomass compared to earth plants with a total biomass of 500 billion tons (Falkowski, 2012). However, they are responsible for nearly 50% of global net primary production and are the primary energy source for aquatic ecosystems (Field et al., 1998), and are also of global significance for climate regulation and biogeochemical cycling. All water bodies on Earth contain high numbers of phytoplankton groups which have a great impact on also ecosystem change (Mishra et al., 2013). Cyanobacteria are a variety of bacteria that are included in this group and are the most common species (Ruiz-Verdú et al., 2008) and it is undesirable to increase in lake ecosystems (Mishra et al., 2013). It poses a major threat to water bodies (Paerl et al., 2011).

Although gathering information about their densities and distributions supports risk assessment and management activities (Hunter et al., 2009) and it is also highly associated with monitoring and evaluation of water quality (Shi et al., 2014). Several studies have been conducted using remote sensing techniques as an emerging tool in the inland and coastal waters to monitor the phenomenon of the cyanobacterial blooms focusing on a temperate reservoir (Beck et al., 2017), optically complex waters like oceans (Soja-Woźniak et al., 2017), turbid productive waters (Mishra et al., 2013), inland and near-coastal waters (Matthews and Odermatt, 2015), and inland waters (Kudela et al., 2015). These studies investigate the presence of Chlorophyll-a (Chl-a) and Phycocyanin (PC) pigments for the

---

* **Corresponding Author**

*(elifkiyak@gmail.com) ORCID ID 0000-0002-8449-2588
(hkarabork@ktun.edu.tr) ORCID ID 0000-0001-7387-7004

Received: 18/05/2022; Accepted: 30/05/2022

Cite this article

Kirtilioglu., E., & Karabork H. (2022). Evaluating the Performance of Algorithms in Estimating the Chl-a Concentration of Lake Bafa. Turkish Journal of Geosciences 3(1), 30-38.

monitoring and detection of cyanobacteria (Hunter et al., 2010). Different sensors have used in different studies and appropriate algorithms (Gitelson et al., 2009; Koponen et al., 2007; Mishra and Mishra, 2012; Moses et al., 2019) were developed by considering the cost, temporal, spatial, and spectral resolution. In parallel to technological developments, sensor technologies will provide optimum solutions for the monitoring of cyanobacteria. Analyzing and estimating Chl-a concentrations constitute the most important research topics in water bodies, because all phytoplankton contain Chl-a. To estimate the volume of phytoplankton and biomass, the Chl-a concentration can be used as an indicator (Vinh et al., 2019).

Many lakes in Turkey are under the influence of increasing population, climate change, agriculture and many anthropogenic activities and events. Lake Bafa, the largest lake in the Aegean region and the 15th largest in Turkey, is also under the negative influence of these factors. The main sources of income in the region surrounding the lake are tourism, fishing, animal husbandry and agriculture.

Because of the first Chl-a estimation algorithms have been developed for marine waters (adapted for blue and green regions of electromagnetic spectrum), they are inappropriate for inland waters as it was mentioned in Watanabe et al. (2018). The main reason is that the high colored dissolved organic matter (CDOM) masks the Chl-a absorption. In addition to this, inland waters such as rivers, reservoirs or lakes need higher spatial resolution sensors considering their size. Landsat and MERIS had the most suitable sensors, but they are no longer available today. The other options like Sentinel 2 (S2) should be considered as an alternative.

The main goal of this research was to evaluate the performance of algorithms in estimating the Chl-a concentration of Lake Bafa based on S2 bands which are simulated from in-situ reflectance data. We used 1/R665xR705, 1/R665-1/R705, (1/R665-1/R705) x R740, R705/(R560+R665), so called M09, G09-2B, G09-3B, K07 respectively in this paper and, Normalized Difference Chlorophyll Index (NDCI) algorithms. Water samples and in-situ measurements collected in two field campaigns. Bands of S2 were simulated from in-situ reflectance data and used to calibrate and validate models for Chl-a estimation.

2. MATERIALS AND METHODS

2.1. Study Area

Lake Bafa is an alluvial barrier lake, and it is in the Büyük Menderes River Basin. This basin is one of the largest basins of Turkey and is located within the borders of the Aegean region – the western part of the country. The lake lies between $37^{0}20'$ - $37^{0}34'$ N latitudes and $27^{0}22'$ - $27^{0}33'$ E longitudes. It is surrounded by the Beşparmak Mountains to the north and east, the İlbir Mountains to the south, and the fertile alluvial plains of the Büyük Menderes Delta to the west (Figure 1).

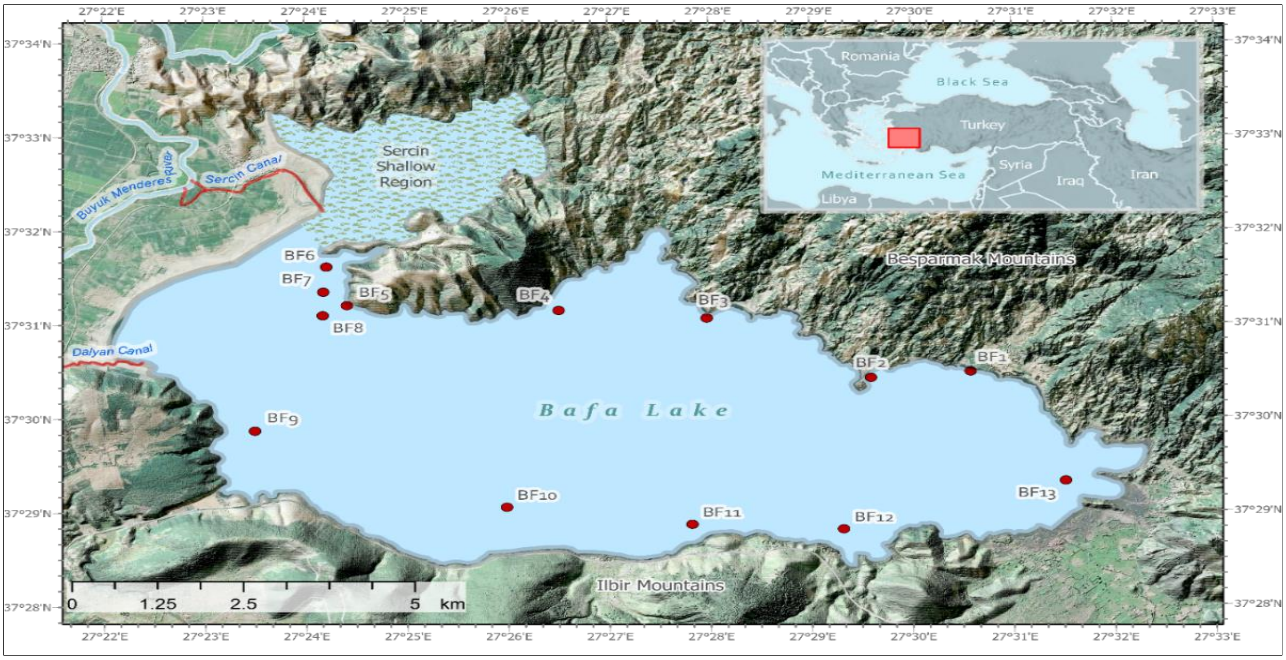

Figure 1. Study area and distribution of in-situ data sample stations in Lake Bafa

The area of the lake is about 6.708 hectares, and its depth varies between 0.5m and 25m. The lake is fed by rains, groundwater, small streams from the mountains, and the Büyük Menderes River. The Turkish General Directorate of State Hydraulic Works (DSI) controls the water level with hydraulic barriers. Water inlets and outlets are controlled by the regulators in the Dalyan and Serçin regions.

2.2. İn-situ data

Two field studies were carried out as two campaigns on 17 July 2018 and 10 September 2019 and water samples collected at 13 fixed stations (labelled as BF1–BF13 in Figure 1). Water samples and corresponding remote sensing reflectance values were tried to be collected from the homogeneously distributed points from the lake surface. Since the Northwest part of the lake (Sercin shallow area, shaded area in Figure 1) is very shallow, the region could not be reached with watercraft and water samples could not be collected.

A total of 26 water samples were collected in this study. They were collected from the lake surface from < 50cm deep and stored in 1-liter sterile plastic bottles, and kept in a cold and dark isolated box until conducting pigment absorption and concentration measurements in the laboratory analyzes for Chl-a. The sum of Chl-a was determined with a spectrophotometer after extraction with hot ethanol (ISO, 1992).

2.3. Calibration of Empirical Models

We evaluated models (empirical algorithms, Table 1) using S2 bands and simulated in-situ reflectance data that was used to calibrate and validate models for Chl-a estimation.

Table 1. Investigated empirical algorithms

Short Name	Algorithms	Reference
M09	$R_{665}^{-1} \times R_{705}$	(Moses et al., 2019)
G09_2B	$R_{665}^{-1} \times R_{705}^{-1}$	(Gitelson et al., 2009)
G09_3B	$(R_{665}^{-1} \times R_{705}^{-1}) \times R_{740}$	(Gitelson et al., 2009)
K07	$R_{705} / (R_{560} + R_{665})$	(Koponen et al., 2007)
NDCI	$(R_{560} - R_{665})/(R_{705} + R_{665})$	(Mishra and Mishra, 2012)

İn-situ remote sensing reflectance spectra was convoluted Sentinel 2 bands using S2 Spectral Response Functions (S2-SRF) v3.0.

2.4. Sentinel 2 Data, Image Processing and Chlorophyll-a Mapping

Sentinel-2 Level-1C (L1C) images were downloaded from Copernicus Open Access Hub for the period of 2018–2019 years. The L1C images are 100x100km ortho images of Top of Atmosphere (TOA) and projected to UTM Zone 35N projection and WGS 1984 datum.

Downloaded images were processed with the ACOLITE atmospheric correction processor. The ACOLITE is a generic processor developed at RBINS for atmospheric correction and processing for coastal and inland water applications. It performs the atmospheric correction by default using the Dark Spectrum Fitting approach.

Images were re-projected to geographic coordinate system with WGS 1984 datum by the Sentinel Application Platform (SNAP) which is developed by Brockmann Consult, SkyWatch, and C-S, a free open toolbox for processing data from the Sentinel missions. Furthermore, SNAP was used for pixel calculation and preparing Chl-a distribution maps.

Although in-situ measurement was planned for the S2 MSI overpass date, the image of 17 July 2018 was under the influence of high sun glint. Thus 19 July 2018, and 10 September 2019 S2 images were used for algorithm validation. There was a cyanobacterium bloom on 24 June 2018, therefore the S2 image of this date was used for map validation.

2.5. Validation

Six of the 20 collected samples were used for validation of the empirical models. The used statistical metrics were the Mean Square Error (MSE, Equation 1); Root Mean Square Error (RMSE, Equation 2); Normalized Root Mean Square Error (NRMSE, Equation 3) Mean Absolute Percentage Error (MAPE, Equation 4) and determination coefficients (R^2).

$$MSE = \frac{1}{n}\sum_{i=1}^{n}(y_a - y_p)^2 \qquad (1)$$

$$RMSE = \sqrt{\frac{1}{n}\sum_{i=1}^{n}(y_a - y_p)^2} \qquad (2)$$

$$\%NRMSE = \left(\frac{RMSE}{y_{max} - y_{min}}\right) * 100 \qquad (3)$$

$$MAPE = \frac{1}{n}\sum_{i=1}^{n}\left|\frac{(y_a - y_p)}{y_a}\right| * 100 \qquad (4)$$

Where, y_{max} is the maximum measured value; y_{min} is the minimum measured value; y_p are predicted values; y_a are measured values, and n is the number of samples.

3. RESULTS AND DISCUSSION

3.1. Laboratory Analysis

The values of the laboratory measurements of Chl-a and measured basic water quality parameters summary statistics are (PH, water temperature, dissolved oxygen) shown in Figure 2 and Table 2. According to analysis results, the Chl-a concentration varies between 4.04 and 8.51 µg/L with a minimum value of 4.04 µg/L at the BF10 station and with maximum values of 8.51 and 8.02 µg/L at the BF8 and BF6 stations respectively.

It can be noticed that the June 2018 data has higher values for all parameters compared to September 2019.

When the Chl-a values were examined, the maximum value was 8.51 (μg/L). In fact, an algal bloom was observed in the Lake in June 2018, however, a sample could not be taken during the algal bloom due to the short duration and the difficulty in obtaining measurement and transportation vehicles rapidly. However, Bafa is a productive lake, and it is possible to reach studies in the literature obtained previous Chl-a values ranging from 0.18 to 200 (μg/L) as 0.2-200 μg/L from Hepsogutlu, (2012), 0.2-200 μg/L from Kesici, (2015), 13.6 μg/L from Kızılkaya et al. (2016), 0.73–32.44 μg/L from Koçak et al. (2017), and 0.18–3.88 μg/L from Ozturk, (2018).

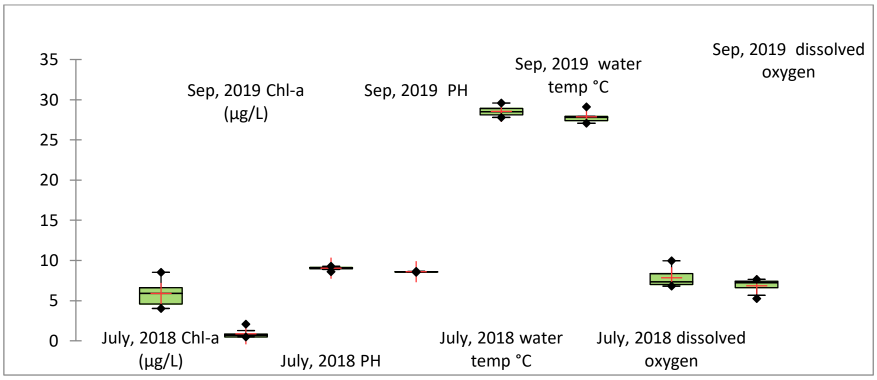

Figure 2. Results of the laboratory analyzes and water quality parameters

Table 2. Summary statistics of the laboratory analyzes and water quality parameters

Statistic	July 2018 Chl-a (μg/L)	Sep 2019 Chl-a (μg/L)	July 2018 PH	Sep 2019 PH	July 2018 water temp °C	Sep 2019 water temp °C	July 2018 dissolved oxygen	Sep, 2019 dissolved oxygen
Minimum	4.040	0.500	8.620	8.530	27.800	27.100	6.800	5.280
Maximum	8.510	2.080	9.300	8.650	29.600	29.100	9.970	7.650
Mean	5.879	0.875	9.042	8.586	28.538	27.885	7.854	6.850
Standard deviation *(n-1)*	1.373	0.518	0.178	0.037	0.571	0.697	1.105	0.761

ASD-FS4 Hi-Res spectroradiometer which has 350-2500 nm wavelength range and 1 nm spectral resolution was used to acquire the in-situ spectral response. A total of 20 reflectance spectra were collected from two campaigns and 13 stations. We couldn't obtain reflectance spectra from 6 stations due to the battery problem of watercraft that have been occurred as an unexpected error during operation. The reflectance values were measured by following Mobley, (1999) protocols early hour in the morning and with a clear sky. The surface reflectance measurements were collected from 10-15 cm above the surface and averaged for each cite (Figure 3). ViewSpec Pro software 5.6 was used for processing.

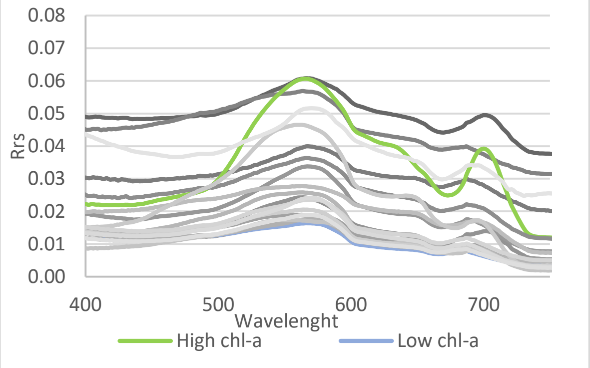

Figure 3. Spectral reflectance averages for 20 measurements

3.2. Chl-a Algorithms

The performance of the five main algorithms used in the literature in Lake Bafa is summarized in the Table 3 and regression graphics in Figure 4.

It should be noticed that the tested models had been evaluated with low relatively narrow and low Chl-a values. Low RMSE values and high %NRMSE values were obtained as expected due to the character of the data set. A significant correlation in all models has been obtained. G09_2B has the highest R^2 value and the fewest error results as M09, G09_2B, K07, NDCI have close R^2 values with 0.679, 0.749, 0.726, 0.700 and RMSE values with 1.882, 1.663, 1.737, 1.818 respectively. The G09_3B model has lower R^2 and higher RMSE values compared to the other four models.

Table 3. Performances of selected Chl-a estimation algorithms

Model	R^2	MSE	RMSE	%NRMSE	MAPE	Empirical Chl-a Alg.
M09	0.679	3.543	1.882	23.498	123.528	y = 16.061 x 10.348
G09_2B	0.749	2.764	1.663	20.755	130.9	y = 0.0959x + 6.0894
G09_3B	0.395	6.664	2.581	32.227	174.148	y = 24.88x + 5.4482
K07	0.726	3.017	1.737	21.686	108.926	y = 32.682x - 6.6527
NDCI	0.7	3.307	1.818	22.701	119.679	y = 30.778x + 6.0008

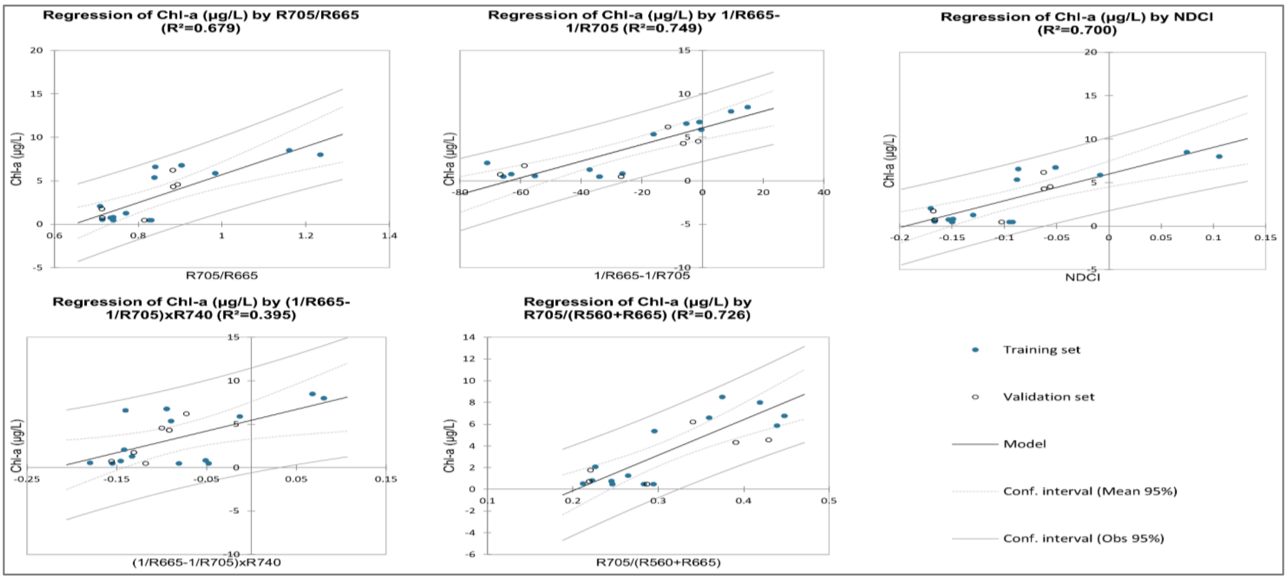

Figure 4. Regression graphics of the five main algorithms used in the literature in Lake Bafa

3.3. Map Validation

We applied the selected algorithms to S2 images to evaluate the applicable range, performance, and validity. The three selected S2 images for map validation were: 19 July 2018, 10 September 2019 and 24 June 2018. First campaign was planned on 17 July 2018 during the S2 overpass, but since the same day S2 image was exposed to the sun glint effect, the S2 image dated 19 July 2018, which covers 50% of the lake was used in the validation.

The distribution of the Chl-a values calculated by the models for the stations and the in-situ Chl-a values are given in Figure 5. As it can be seen from the figure that, all models are successful in predicting the Chl-a trend. To interpret the models and Chl-a estimations, it is necessary to compare the calculated trend for the model with the in-situ Chl-a estimation trend. The vertical axis represents the amount of Chl-a in µg/L unit, while the horizontal one shows station names. So, it is clear from the Figure 5 that, the predictions of BF10 and BF13 stations gave the least accuracies. All models were underestimated Chl-a values at point BF10 and BF13 except only one at BF10 station represented as dark orange line (19072018_G09_2B).

The second campaign was carried out on 10 September 2019. In this campaign, the amount of Chl-a at Lake Bafa is relatively low (Figure 6). All models were overestimated Chl-a values at all points. When both graphs are examined, M09 and NDCI models have significant similarities (light and dark blue lines in both figures) and they have close Chl-a value estimations.

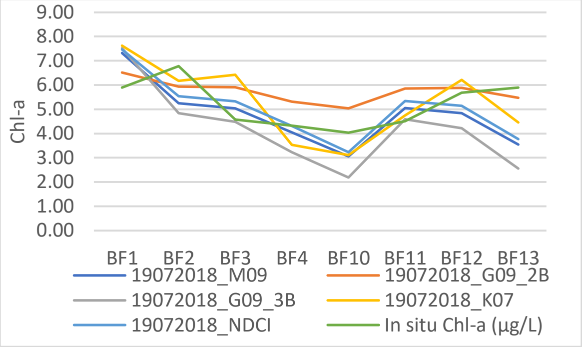

Figure 5. Chl-a values calculated from 19 July 2018 S2 image

Figure7, 8, and 9 are the Chl-a distribution maps which obtained by applying selected algorithms to S2 images. The RGB band combinations of S2 images are B4-B3-B2 respectively. All thematic maps are prepared with colors containing the same Chl-a range values.

We applied the algorithms to the S2 image dated 24 June 2018 to see the performance of the models at high Chl-a values during the algal bloom. As it is seen from the Figure 7 that the G09_2B model, which has the highest R^2 and the least error values, is insufficient to detect the high Chl-a values that occur during algal bloom.

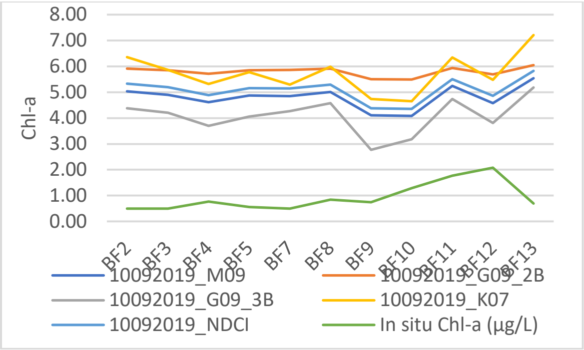

Figure 6. Chl-a values calculated from 10 September 2018 S2 image

The G09_2B model calculated the Chl-a value in the range of 5-10 µg/L in the region where the algae bloom is intense (indicated with a red arrow as region a in Figure 7). The Chl-a value in the same region was calculated as 55-60 µg/L by M09, 115-125 µg/L by G09_3B, 35-40 µg/L by K07, and 25-30 µg/L by NDCI. All models calculated Chl-a values in the b region which is less affected by algal bloom in the range of 5-10 µg/L. It is clear from the thematic maps that models other than G09_2B predict the algal bloom pattern correctly.

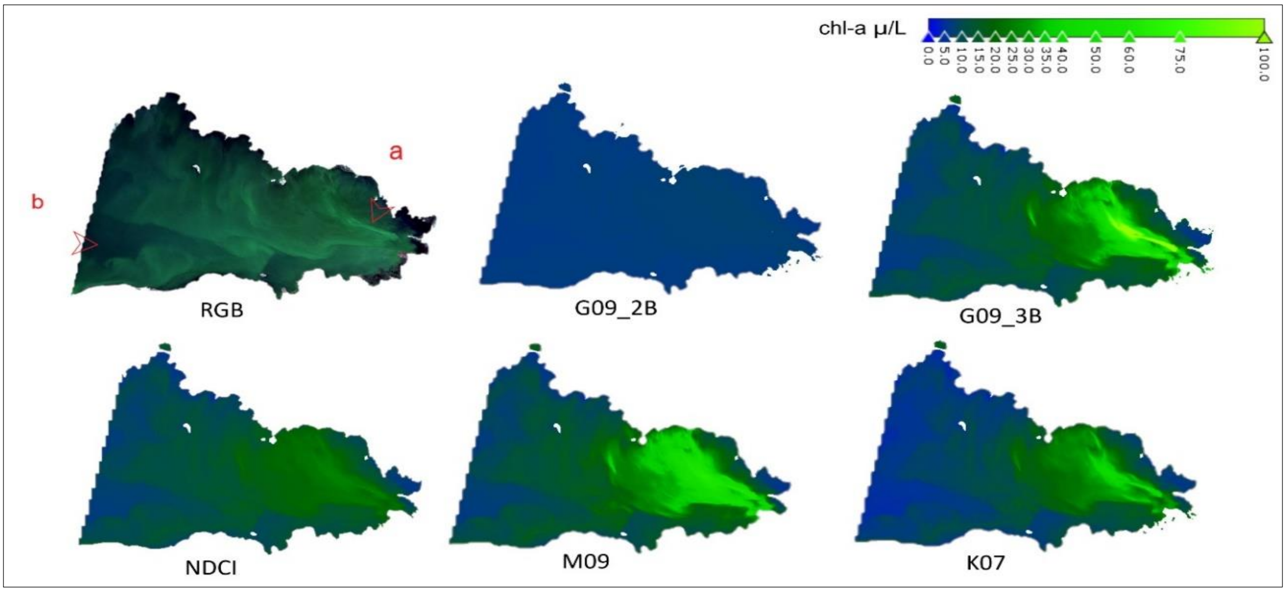

Figure 7. Chl-a distribution maps obtained by applying selected algorithms to S2 images on 24 June 2018

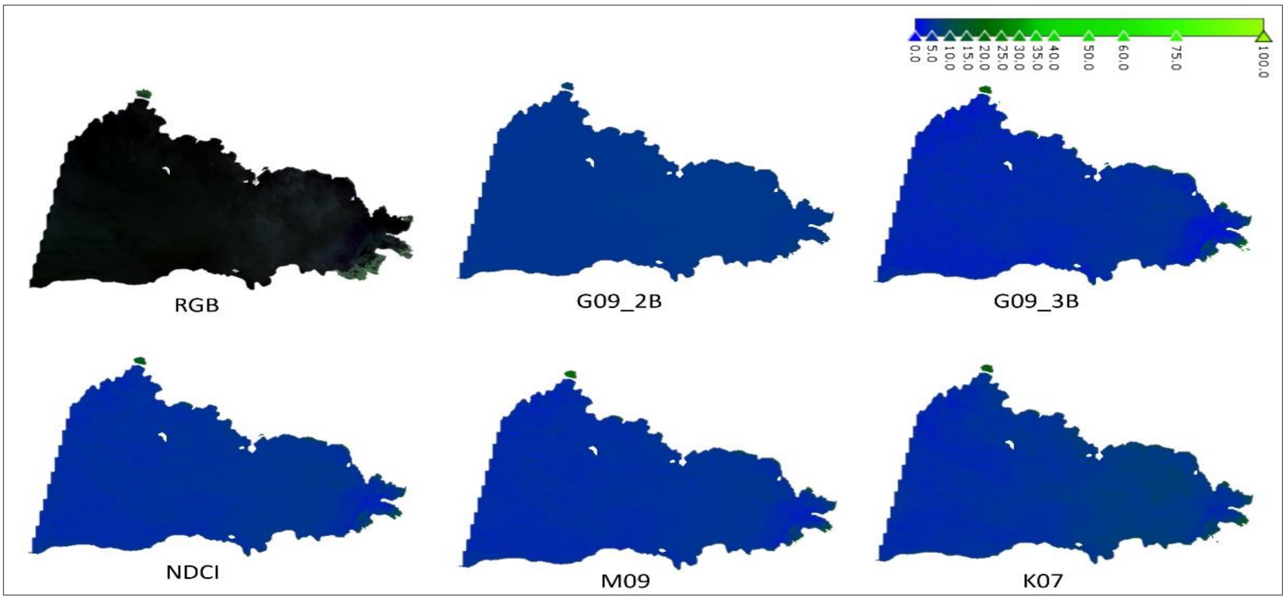

Figure 8. Chl-a distribution maps obtained by applying selected algorithms to S2 images on 19 July 2018

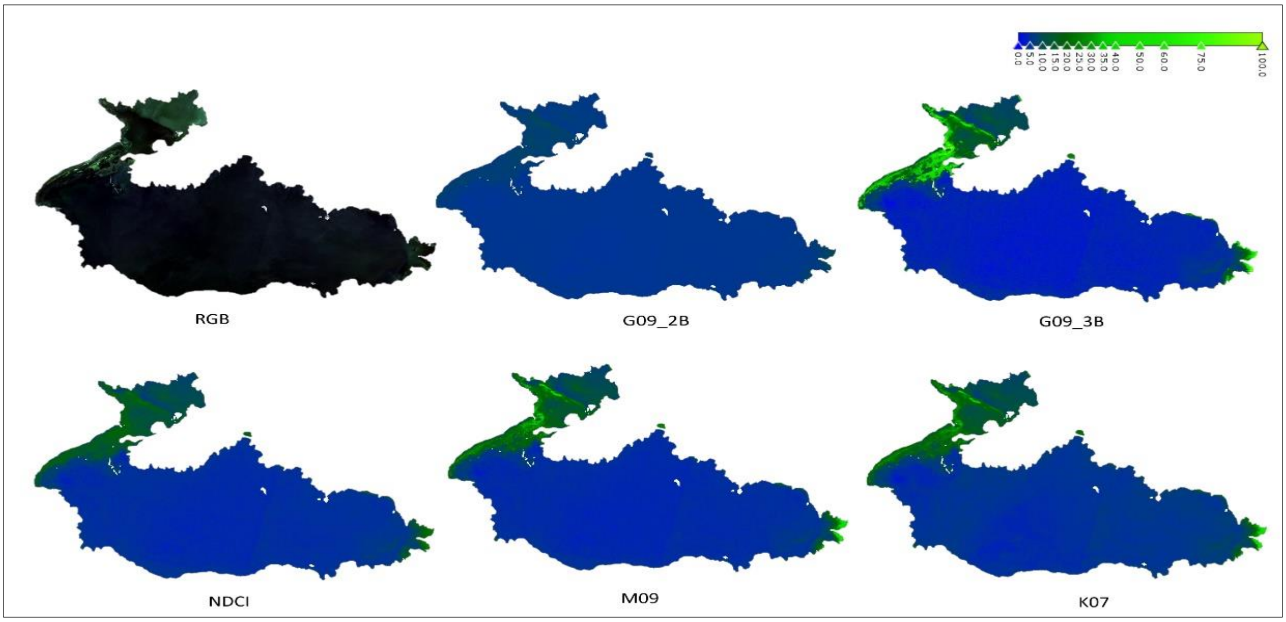

Figure 9. Chl-a distribution maps obtained by applying selected algorithms to S2 images on 10 September 2019

4. CONCLUSIONS

The performance of five commonly used and trending algorithms in estimating the Chl-a concentration in an inland water of Turkey has been investigated in this paper. The selected study area Lake Bafa is a productive lake and has a great potential for the performance test for the Chl-a estimation. 26 water samples constitute the in-situ data part of the study and they have been collected from 13 station points as two field campaigns. 20 reflectance spectra data have also been collected simultaneously and been used for simulating Sentinel 2 bands which constitutes the remotely sensed data part. The tested algorithms were selected according to their frequent use in the literature about estimating Chl-a concentrations in inland and coastal water bodies.

For all algorithms, the R^2, MSE, RMSE, %NRMSE, and MAPE values have been calculated. The R^2 values of M09, G09_2B, G09_3B, K07, and NDCI were calculated as 0.679, 0.749, 0.395, 0.726, and 0.7 respectively, so it can be said that there are significant correlations obtained for all algorithms.

According to analyses and research, although the G09_2B model had the best statistical results, it has failed in map validation process for high Chl-a values. The least correlation values have been calculated for Model G09_3B with the highest error values, and G09_3B and K07 tend to exaggerate the values.

When an algal bloom phenomenon occurs, high Chl-a concentration values may observe in any water body including inland and coastal areas. However, this is a phenomenon that happens only when optimum conditions exist. If the in-situ data collection date matches the algal bloom phenomenon, more information can be gained about the behavior, reliability, and accuracy of the algorithms. During the bloom that took place at the end of June and the beginning of July 2018 at the study area, it was not possible to collect in-situ data. Technical and organizational unexpected problems prevented this optimal match for this research as it is mentioned in previous sections of this paper.

As a conclusion, the M09 and NDCI models have a potential for Chl-a estimation in Lake Bafa since they provide better results. Both models had high R^2 and low error values and have similar results in analyses with S2 images. When the matching S2 image with the algal bloom was examined, both models were very successful in predicting the Chl-a pattern and they gave high concentration estimation values as they compared with the previous studies.

It is highly recommended for the future studies that, the Chl-a values can be estimated with higher accuracy when algorithms are calibrated with a data set containing a wider range of Chl-a values, in other words during the algal bloom phenomenon.

Acknowledgement

This research can be considered as a part of PhD Thesis of Elif Kirtiloglu with the title of "Evaluating Potential and Use of the Planet System in Terms of Detection, Monitoring, and Temporal Analysis of Cyanobacteria with Remote Sensing Techniques", Konya, Turkey, 2022.

This research was also supported by Konya Technical University Scientific Research Project (No 18201069).

Author Contributions

Elif Kirtiloglu: Conceptualization, Methodology, Software, Writing. **Hakan Karabork:** Supervision, Methodology, Writing – Reviewing and Editing.

Conflicts of Interest

The authors declare no conflict of interest.

REFERENCES

Beck, R., Xu, M., Zhan, S., Liu, H., Johansen, R. A., Tong, S., Yang, B., … & Huang, Y. (2017). Comparison of satellite reflectance algorithms for estimating phycocyanin values and cyanobacterial total biovolume in a temperate reservoir using coincident hyperspectral aircraft imagery and dense coincident surface observations. *Remote Sensing*, 9(6), 538.

Falkowski, P. (2012). Ocean Science: the power of plankton. *Nature*, 483, 17–20.

Field, C.B., Behrenfeld, M.J., Randerson, J.T., & Falkowski, P. (1998). Primary production of the biosphere: integrating terrestrial and oceanic components. *Science*, 281(5374), 237-240.

Gitelson, A.A., Gurlin, D., Moses, W.J., & Barrow, T. (2009). A bio-optical algorithm for the remote estimation of the chlorophyll-a concentration in case 2 waters. *Environmental Research Letters*, 4(4), 045003.

Hepsogutlu, D. (2012). Macrobentic Organisms and Physicochemical Parameters of Bafa Lake (MSc Thesis). Dokuz Eylul University, İzmir, Turkey (In Turkish).

Hunter, P.D., Tyler, A.N., Gilvear, D.J., & Willby, N.J. (2009). Using remote sensing to aid the assessment of human health risks from blooms of potentially toxic cyanobacteria. *Environmental science & technology*, 43(7), 2627-2633.

Hunter, P.D., Tyler, A.N., Carvalho, L., Codd, G.A., & Maberly, S.C. (2010). Hyperspectral remote sensing of cyanobacterial pigments as indicators for cell populations and toxins in eutrophic lakes. *Remote Sensing of Environment*, 114(11), 2705-2718.

ISO. (1992). Water quality measurement of biochemical parameters spectrometric determination of the chlorophyll-a concentration. International Organization for Standardization.

Kesici, K. (2015). The Research on the Factors that Causes Toxic Nodularia Spumigena Mertens ex Bornet & Flahault Blooms in Lake Bafa (PhD Thesis). Ege University, İzmir, Turkey (In Turkish).

Kızılkaya, I.T., Demirel, Z., Kesici, K., Kesici, E., & Sukatar, A. (2016). Morphological, Molecular and Toxicologial Characterization of Nodularia spumigena Mertens in Jungens (1822) from Brackishwater Lake Bafa (Turkey). *Sinop Uni J Nat Sci*, 1, 39–52.

Koçak, F., Aydın-Önen, S., Açık, Ş., & Küçüksezgin, F. (2017). Seasonal and spatial changes in water and sediment quality variables in Bafa Lake. *Environmental Earth Sciences*, 76(17), 1-11.

Koponen, S., Attila, J., Pulliainen, J., Kallio, K., Pyhaïahti, T., Lindfors, A., Rasmus, K., & Hallikainen, M. (2007). A case study of airborne and satellite remote sensing of a spring bloom event in the Gulf of Finland. *Continental Shelf Research*, 27(2), 228-244.

Kudela, R.M., Palacios, S.L., Austerberry, D.C., Accorsi, E.K., Guild, L.S., & Torres-Perez, J. (2015). Application of hyperspectral remote sensing to cyanobacterial blooms in inland waters. *Remote Sensing of Environment*, 167, 196–205.

Matthews, M.W., & Odermatt, D. (2015). Improved algorithm for routine monitoring of cyanobacteria and eutrophication in inland and near-coastal waters. *Remote Sensing of Environment*, 156, 374–382.

Mishra, S., & Mishra, D.R. (2012). Normalized difference chlorophyll index: A novel model for remote estimation of chlorophyll-a concentration in turbid productive waters. *Remote Sensing of Environment*, 117, 394–406.

Mishra, S., Mishra, D.R., Lee, Z., & Tucker, C.S. (2013). Quantifying cyanobacterial phycocyanin concentration in turbid productive waters: A quasi-analytical approach. *Remote Sensing of Environment*, 133, 141-151.

Mobley, C.D. (1999). Estimation of the remote-sensing reflectance from above-surface measurements. *Applied Optics*, 38(36), 7442–7455.

Moses, W.J., Saprygin, V., Gerasyuk, V., Povazhnyy, V., Berdnikov, S., & Gitelson, A.A. (2019). Olci-based nir-red models for estimating chlorophyll-a concentration in productive coastal waters - a preliminary evaluation. *Environmental Research Communications*, 1(1) 011002.

Ozturk, Y. (2018). Determination of Population Density and Propagation Map of Mytilaster Marioni (Locard, 1889) (Mollusca; Bivalvia; Mytilidae) in Lake Bafa (MSc thesis). Aydın Adnan Menderes University, Aydın, Turkey (In Turkish).

Paerl, H.W., Hall, N.S., & Calandrino, E.S. (2011). Controlling harmful cyanobacterial blooms in a world experiencing anthropogenic and climatic-induced change. *Science of the total environment*, 409(10), 1739-1745

Ruiz-Verdú, A., Simis, S.G.H., de Hoyos, C., Gons, H.J., & Peña-Martínez, R. (2008). An evaluation of algorithms for the remote sensing of cyanobacterial biomass. *Remote Sensing of Environment*, 112(11), 3996-4008

Shi, K., Zhang, Y., Li, Y., Li, L., Lv, H., & Liu, X. (2014). Remote estimation of cyanobacteria-dominance in inland waters. *Water research*, 68, 217-226.

Soja-Woźniak, M., Craig, S.E., Kratzer, S., Wojtasiewicz, B., Darecki, M., & Jones, C.T. (2017). A novel statistical approach for ocean colour estimation of inherent optical properties and cyanobacteria abundance in optically complex waters. *Remote Sensing*, 9(4), 343.

Vinh, P.Q., Ha, N.T.T., Binh, N.T., Thang, N. N., Oanh, L. T., & Thao, N.T.P. (2019). Developing algorithm for estimating chlorophyll-a concentration in the Thac Ba Reservoir surface water using Landsat 8 Imagery. *Vietnam Journal of Earth Sciences*, 41(1), 10-20.

Watanabe, F., Alcântara, E., Rodrigues, T., Rotta, L., Bernardo, N., & Imai, N. (2018). Remote sensing of the chlorophyll-a based on OLI/Landsat-8 and MSI/Sentinel-2a (Barra Bonita Reservoir, Brazil). *Anais Da Academia Brasileira de Ciencias*, 90(2), 1987–2000.

TURKGEO
TURKISH JOURNAL OF GEOSCIENCES

ISSN: *2717-7696*
Research Article
Vol; 3, Issue; 1, pp. 39-48, 2022
DOI: *10.48053/turkgeo.1112911*
Journal homepage:
https://dergipark.org.tr/en/pub/turkgeo

Geophysical analysis of Thermo-Physical properties of rocks in Ikogosi field for geothermal energy prospect

Samuel Sedara[*1]

[1]*Adekunle Ajasin University, Faculty of Science, Physics Electronics, Ondo State, Nigeria*

Keywords
Low enthalpy
Ikogosi
Heat flow
Heat production
Geothermal energy
Porosity

ABSTRACT

The thermal and physical properties of rock units from Ikogosi Warm Spring (IKGWS) in the Southwestern part of Nigeria were examined in order to characterize and explore its geothermal prospect and to provide an insight into the different thermal properties of rocks of the study area. A total of 40 rock samples made up of granite, quartzite and gneiss series were collected from the outcrops of the study area and analyzed for Thermal conductivity (TC), Radiogenic heat production (RHP), Heat flow (HF), Porosity, Density and surface spring temperature measurements. The RHP values for all samples varied from 1.8 to 3.5μWm^{-3} with an average value of 2.5μWm^{-3} and standard deviation (SD) of 0.4 while the heat flow values varied from 14 to 27mWm^{-2} with an average of 19mWm^{-2} and SD of 3.4. The TC values varied from 2.95 to 4.11 with a mean of 3.49mWK^{-1} with a SD of 0.4 while the porosity values varied from 0.21-1.15 % with a mean of 0.62% with SD of 0.39. The density values varied from 2.68 to 2.85gcm^{-3} with a mean of 2.76gcm^{-3} and SD of 0.067. The surface temperature of the spring varied from 32 to 45°C with a mean of 38.9°C. From these results the average RHP and HF values estimated from all samples was below the 4μWm^{-3} and 100mWm^{-2} recommended value of heat to be considered for economic importance. Thus, the IKGWS geothermal field cannot be explored for power generation but for other geothermal activities and may be classified as a low enthalpy geothermal system (<150°C).

1. INTRODUCTION

There have been so many researches in the Ikogosi warm spring (IKGWS) area in the attempt to understand the general structural pattern and their results pointed to the fact that IKGWS is situated along a trending faults and fractures (Ojo et al. 2011; Abraham et al., 2014). As a follow-up, some research work has also been done to investigate the prospect of geothermal energy exploration and their results indicated potential of the IKGWS for geothermal prospect based on the fact that fractures and faults acts as pathways for the thermal fluid to the subsurface (Abraham and Alile, 2019; Salawu et al., 2021; Sedara, 2020; Sedara and Alabi, 2021). Thus, in a follow up for these geothermal investigations within IKGWS, we have attempted to scale and classify the geothermal potential prospect of the area using combined thermal properties of rocks within the study area.

Geothermal energy is a reliable renewable energy source from within the earth and comparing with other renewable energies, it is fundamentally confined and location specific especially with regions of magmatic occurrences (Huenges and Ledru, 2011). However, the depletion and reduction of energy resources have become more widespread and therefore the necessity to consider and develop geothermal energy resource which has become is now becoming more generally recognized and accepted (Zhu et al., 2021). Several Earth processes are largely dependent on temperature variances within the Earth and estimating these temperatures variations and uncertainties are challenging without considering the evaluation of radiogenic heat production (McKenzie and Priestley, 2016; Liu and Currie, 2016).

Basically, the three main modes of heat energy transfer are conduction, convection, radiation but the radiation and convection are assumed to have a

---

[*] **Corresponding Author**

[*](samuel.sedara@aaua.edu.ng) ORCID ID 0000-0002-2116-1263

Cite this article

Sedara, S. (2022). Geophysical analysis of Thermo-Physical properties of rocks in Ikogosi field for geothermal energy prospect. Turkish Journal of Geosciences 3(1), 39-48.

Received: 15/05/2022; Accepted: 21/06/2022

reasonably slight influence on geothermal energy transfer.

The understanding of the thermal and structural setting of an area involves precise information of radiogenic heat production, heat flow and thermal conductivity of all rock units of the area. A detailed data for all these properties are not only predictable for evaluating the thermal improvement of basement and sedimentary formations (Popov et al., 2016).

Therefore, this research paper mainly investigates the lithological units and their basic heat and physical properties that governed and contributed to the thermal processes. These processes are influenced by thermal conductivity, porosity, density, mineral composition, water content. All these play vital roles in many research fields like hydrothermal resources development, subsurface thermal energy; civil engineering and environmental and geotechnical engineering (Popov et al., 1999; Gao et al., 2015).

A characteristic instance of an area with great geothermal and geodynamic activities conveyed by surface spring manifestation is the Ikogosi warm spring area situated in the southwestern part of Nigeria (Abraham et al., 2014; Olorunfemi et al., 2013). Like some other geothermal regions, geothermal resources around IKGWS are expressed on the outward in the like hot springs which have been ascribed to the manifestation of many faulting systems in the area (Abraham et al., 2014; Adepelumi et al., 2008). The lithological units and their effect on the hot and cold spring manifestations around the IKGWS is yet to be well examined in line with geothermal potential of the area (Figure 1). Likewise, the heat source depth which may perhaps provide evidence for thermal configuration and geodynamic events of the area is not well defined despite the immense manifestation of geothermal resources on the surface (Ozgener and Kocer, 2004; Abubakar et al., 2017; Ozdemir and Palabiyik, 2019; Ozdemir et al., 2021).

The rocks analyzed were mainly from the different sections in the IKGWS area and a total of 40 samples were collected comprising of granite, gneiss and quartzite series. In particular, the samples were analyzed majorly for radiogenic heat production, water content, thermal conductivity, porosity and heat flow content to define the connection between all the properties and their link with geothermal prospect of the area.

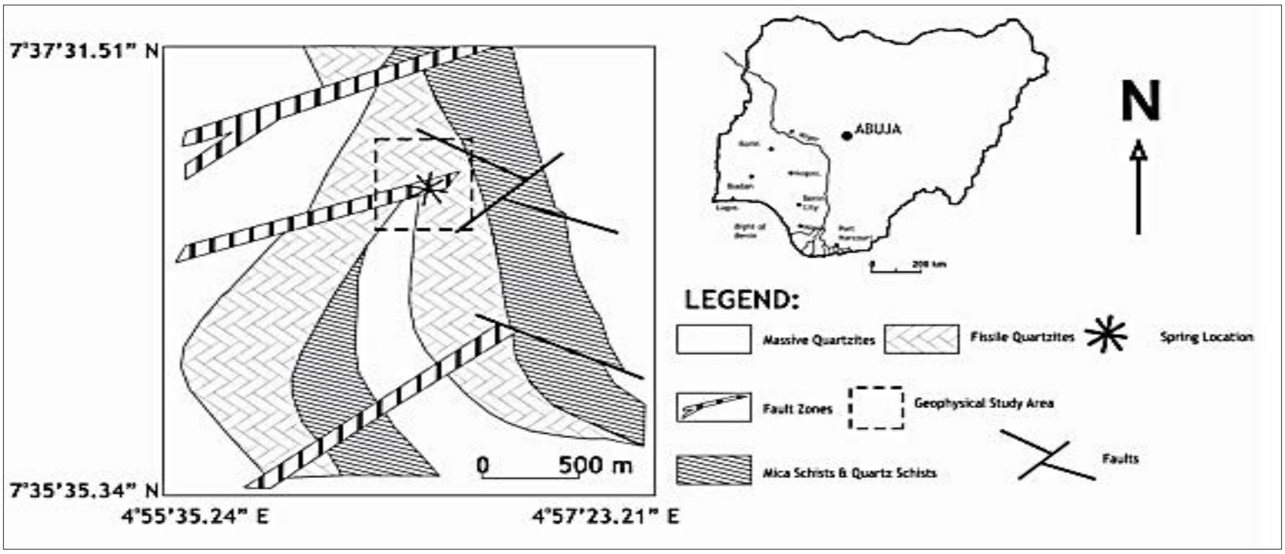

Figure 1. Map of Geology of Ikogosi warm spring area (modified after Adegbuyi et al., 1996)

2. MATERIALS AND METHODS

2.1. The Radiogenic Heat Measurements and Estimations

Radiations (alpha-α, beta-β and gamma-ɣ) from decay of radioactive elements contained in rock units around the study area are of particular interest. The radiations from the decay of radioelements of ^{232}Th, ^{40}K and ^{238}U contained in the outcrop of rock unit in parts per million (ppm) were measured from laboratory analysis of 30 rock samplings of the study area (Figure 2) from NaI Spectrometry. The concentrations of the radioelements (C_{Th}, C_U and C_K) and density, ρ) were measured in a research laboratory and the resulting concentrations were inserted in equation (1) of Birch, (1954) to estimate the radiogenic heat production (HP in μWm^{-3}):

$$HP=\rho*(0.026*C_{Th}+0.097*C_U+0.035*C_K) \quad (1)$$

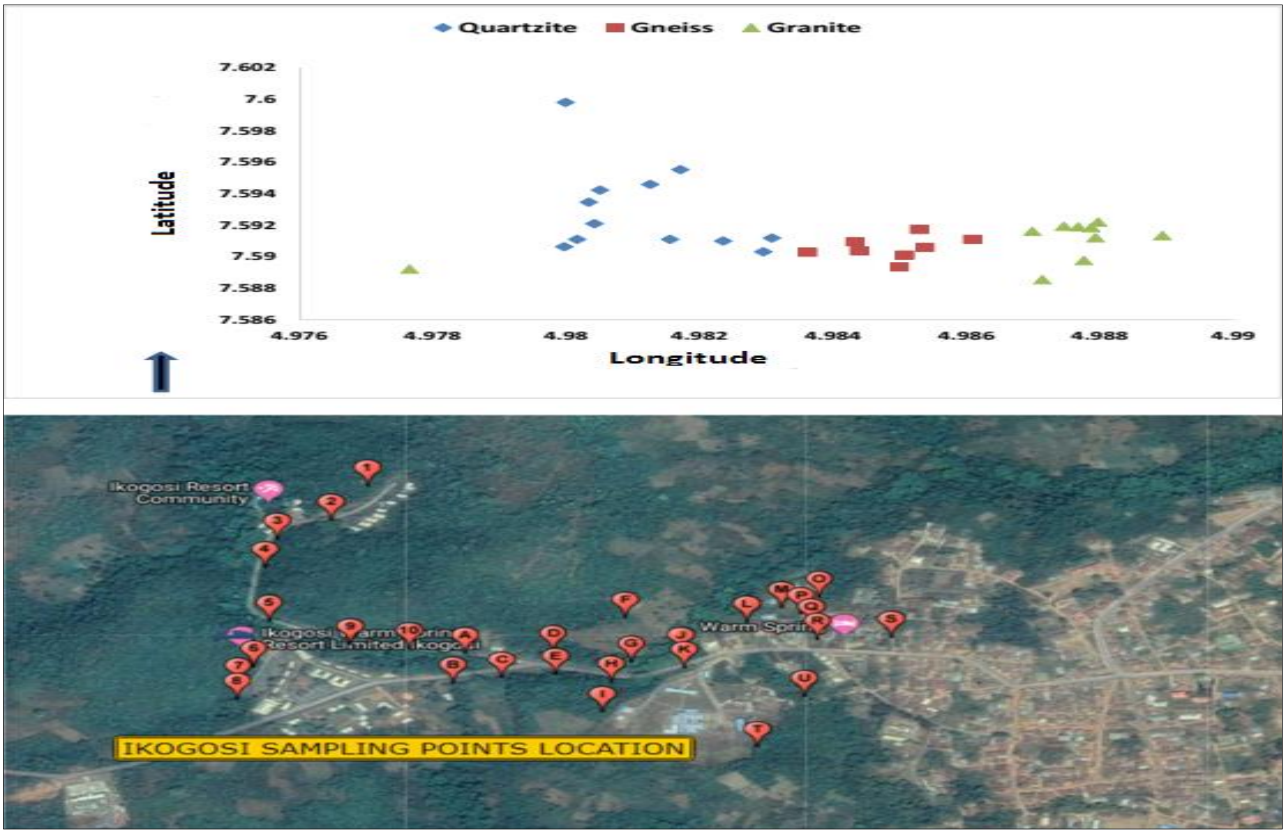

Figure 2. The sampling points and location of study area

2.2. The Thermal Conductivity Measurements and Estimations

There are two methods of measuring the thermal conductivity of materials which are direct (laboratory) and indirect (computational). The thermal conductivity of rock samples in this work was measured using Thermal conductivity meter. Before taking measurements, the thermal conductivity meter was standardized and calibrated using reference specimens. Ten rock samples comprising of three Quartzite, three Gneiss and four Granite series were broken from fresh outcrops of IKGWS. The samples were dressed, cut and refined into cylinder-shaped discs of diameter 25 mm and thickness between 10 and 25 mm which is dependent on rock sample variety and grain size.

The dressed rock discs are pulverized and refined till the thickness variant is less than 0.01 mm. Then the samples are placed inside the stack one after the other and readings were taken. Each measurement takes about 30-40 min to attain steady state condition. Readings (upper voltage V_U, lower voltage V_L, heat sink V_{HS} and reference voltage V_{REF}) are noted and recorded. Using the above readings and calibration, thermal conductivity values of the rocks are determined. To minimize loss of heat to the environs, the rock stack is sheathed and insulated and the entire system is bounded within a shielded case and measurements taken after the stack reaches in steady-state or equilibrium condition and finally the readings taken are inserted into a processing software to get the values of Thermal Conductivity of the respective rock samples.

2.3. Measurement of Density, Porosity and Surface Spring Temperature

The rock samples were weighed up in water and in air on established law of Archimedes principle. The rock sample density (ρ_{sample}) was gotten by the equation 2 by weightiness of the rock sample in air, water and density of water (W_{air}, W_{wate} and ρ_{water}).

$$\rho_{sample} = \frac{W_{air}*\rho_{water}}{W_{air}-W_{water}} \tag{2}$$

Also the porosity (V_p) is divided by volume of rock (V_r) (solid + space or holes) given by equation 3:

$$Porosity = \frac{Volume\ of\ voids(V_P)}{Total\ volume(V_r)} * 100\% \tag{3}$$

The cylinder-shaped disc containing the rock samples are oven dried and the measurements of the dry rock samples (W_{dry}) taken. The samples are placed inside a desiccator to take away the air from the rock pores and later saturated with tap water under vacuum for almost 20 hours to permit water into the pores and then the water-saturated rock sample weight (W_{sat}) is measured. The porosity can be expressed as equation 4:

$$Porosity = \frac{W_{sat} * W_{dry}}{\pi * R * R * H} * 100 \qquad (4)$$

Where: R=radius of the rock sample disc, H=thickness of the rock sample disc.

The values of density and porosity of the rock samples are tabulated in next section.

2.4. Heat Flow Estimations

Two unconventional computational methods (Turcotte and Schubert, 2002; Beardsmore and Cull, 2001; Faweya, 2008; Sedara, 2020) was used to get the values of heat flow for the rock samples given in equations (5) and (6) as:

$$H_f = \frac{H_{RT}(Mm+Cr)}{S} \qquad (5)$$

$$H_f = \frac{\partial T}{\partial x}\lambda \qquad (6)$$

Where: H_f=heat flow in (mWm^{-2}), H_{RT}= total heat production from radioactive decay in the rock, Mm + Cr= the mass of mantle plus crust given as ≈ 4 × 10^{24} kg, S= total surface area of the earth given as ≈ 5.1 × 10^{14} m^2, $\frac{\partial T}{\partial x}$=Temperature gradient, λ=Thermal conductivity.

The reason why this is done is because direct measurements of heat flow are very less in basement complex terrains of Nigeria. The only existing records of heat flow is found in the results of Brigaud et al., (1985) of the Western part of Africa Shield of Ghana, Liberia, and Nigeria with values fluctuating between 30 and 40 mWm^{-2} and also results from Verheijen and Ajakaiye, (1979) with mean value of 38.5 mWm^{-2}. There have been no bottom hole or borehole data in the southwestern part of Nigeria. The estimation of heat flow in Southwestern part of Nigeria has been through Curie Point Depth (CPD) estimation from aeromagnetic data which assumed constant values of Curie temperature and Thermal conductivity. The heat flow gotten from equation 5 was use to get the temperature gradient for the rock samples using the measured TC values of each rock samples from equation 6. But going by the approach applied in this work, the heat flow data estimated for IKGWS varied from 14 to 27 mWm^{-2} with mean value of 19 mWm^{-2}.

3. RESULTS and DISCUSSION

3.1. Deductions from Measured Parameters

The granitic rocks have the highest heat production while the gneiss and quartzite samples are characterized by variable abundances in K and Th. Uranium, however is almost at the same level in rocks in the area. K content ranged from 1.65 to 5.70 % with average of 3.24 %. Th content is highly variable from as low 9.4 to 25.20 ppm while U content varied from 1.07 to 3.75 ppm with an average of 2.31 ppm. Th concentration has large variability compared to U and K respectively (Table 1). The values of the heat production varied from 1.8 to 3.5 μWm^{-3} with an average of 2.5 μWm^{-3}. The plots show that HP values correlates well with Th abundances for most of the samples whereas no such prominent correlation are observed with K and U (Figure 3). The granite (IKGL3) samples has larger amount of K, U, and Th concentrations than the two other samples and it produces the largest amount of heat production. The present study is limited on data around IKGWS but detailed study in the Southwestern part of Nigeria is needed to characterize radio elemental and heat production for the whole region which will be useful for constraining thermal structure of the region. This study also showed that the various thermal properties vary from the different samples from the different points of the study area (Figure 4).

For the individual rock contribution, the quartzite heat flow value is the highest which varies from 14-27 mWm^{-2} with a mean value of 18 mWm^{-2}. The heat flow values for gneiss varies from 16-23 mWm^{-2} with a mean value of 20 mWm^{-2} while for granites, the heat flow varies from 17-25 mWm^{-2} with a mean of 21 mWm^{-2}. The Uranium contribution to the heat production of the area is higher in the quartzite series compared to other rock series likewise, for the heat flow (Figure 8 and 9).

However, the study area and its environs is assumed to be tectonically stable so the interference of magma to the subsurface such that it will cause earthquake is limited. The high heat flow in many geothermal provinces is based on induced magmatic and tectonic activities (Espinosa-Cardeña, and Campos-Enriquez, 2008). Also, the existence of active lineaments may as well be liable for the surface expressions of hot and cold springs in IKGWS area. The density and porosity values of ten rock samples have been given and summarized in Table 2. The three rock series showed slight difference in density (narrow range with): Quartzite range between 2.79 to 2.85 gcm^{-3} with an average of 2.81 ±0.03gcm^{-3}. Gneiss range from 2.68 to 2.85 gcm-3 with an average value of 2.76 ± 0.09 gcm^{-3}. Granite series varies from 2.67 to 2.72 gcm^{-3} with a mean density of 2.7±0.03 gcm^{-3} as shown in Figure 5 even when compared with granitoids of the other countries (Chopra et al., 2020; Ozdemir et al., 2021).

Table 1. Radiogenic heat production (RHP) estimation results for the rock types in IKGWS

Latitude	Longitude	Lithology			K%	U(ppm)	Th(ppm)	A (μWm^{-3})	HF (mWm^{-2})
7.595528	4.981714	Quartzite (IKGL1)	QUI	N=12	5.7	1.38	11.2	2.79	22
7.594592	4.981263		QUII		4.06	1.42	9.65	2.19	17
7.59423	4.980512		QUIII		2.71	1.79	15.1	2.39	19
7.593465	4.980341		QUIV		2.66	1.14	10.22	1.84	14
7.592103	4.980427		QUV		5.01	2.02	19.51	3.48	27
7.591104	4.980169		QUVI		2.32	2.11	15.44	2.34	18
7.590636	4.979976		QUVII		2.35	1.74	20.02	2.78	22
7.599806	4.979997		QUVIII		2.24	3.01	15.11	2.35	18
7.591104	4.981564		QUIX		1.65	1.07	12.23	1.76	14
7.590997	4.982358		QUX		3.02	2.77	9.4	1.98	16
7.591189	4.983087		QUXI		1.78	2.86	14.02	2.1	16
7.590317	4.982959		QUXII		2.08	3.12	11.49	1.95	15
				Min	1.65	1.07	9.4	1.76	14
				Max	5.7	3.12	20.02	3.48	27
				average	2.97	2.04	13.62	2.33	18
				SD	1.29	0.74	3.58	0.49	4
7.590295	4.983624	Gneiss (IKGL2)	GNI	N=8	2.14	1.5	20.11	2.71	21
7.590955	4.984332		GNII		2.75	2.55	16.21	2.57	20
7.59038	4.984396		GNIII		1.93	1.66	14.27	2.08	16
7.591742	4.985297		GNIV		5.41	3.46	10.02	2.75	22
7.590593	4.985383		GNV		3.31	1.23	19.04	2.91	23
7.590104	4.985083		GNVI		3.01	2.04	17.04	2.68	21
7.589359	4.984997		GNVII		2.87	3.04	11.66	2.18	17
7.591104	4.986091		GNVIII		2.81	3.68	10.24	2.07	16
				Min	1.93	1.23	10.02	2.07	16
				Max	5.41	3.68	20.11	2.91	23
				average	3.03	2.4	14.82	2.49	20
				SD	1.06	0.93	3.91	0.33	3
7.591614	4.986993	Granites (IKGL3)	GRI	N=10	2.21	2.56	16.82	2.3	18
7.591933	4.987465		GRII		3.87	2.61	14.2	2.48	19
7.59221	4.98798		GRIII		4.64	2.11	20.11	3.19	25
7.591891	4.987679		GRIV		2.81	1.87	25.2	3.18	25
7.591848	4.987872		GRV		3.32	3.23	22.11	3.12	24
7.59121	4.987937		GRVI		4.04	3.75	10.21	2.23	17
7.591338	4.988945		GRVII		5.05	2.68	11.71	2.56	20
7.588551	4.987143		GRVIII		3.46	2.78	16.67	2.62	21
7.589764	4.987765		GRIX		2.82	2.61	18.52	2.61	20
7.589211	4.977659		GRX		5.3	1.62	12.44	2.61	20
				Min	2.21	1.62	10.21	2.23	17
				Max	5.3	3.75	25.2	3.19	25
				average	3.75	2.58	16.8	2.69	21
				SD	1.02	0.62	4.81	0.35	3

The porosity of the three rock series showed that: Quartzite range between 0.91 to 1.15 % with a mean value of 1.05±0.11 %. Gneiss series have a range between 0.21 to 0.35% with an average value 0.27 ±0.07 %. Granites porosity varied from 0.25 to 0.5% with mean of 0.38 ±0.13%. Here the porosity values of the granite and gneiss series is very low compared to the quartzite porosity values (Figure 5 and 6).

The thermal conductivity values for the three rock series showed a wide range. The TC for: Quartzite ranged between 3.22 and 4.11 $Wm^{-1}K^{-1}$ with mean value of 3.81±0.4 $Wm^{-1}K^{-1}$. Gneiss ranged from 2.95 to 3.65 $Wm^{-1}K^{-1}$ with mean value of 3.21±0.38 $Wm^{-1}K^{-1}$. Granite series ranged between 2.98 to 3.62 $Wm^{-1}K^{-1}$ with mean value of 3.34±0.33 $Wm^{-1}K^{-1}$. Hence Gneiss and Quartzite had higher values than the Granite series (Figure 6 and 7).

In absence of conventional heat flow data, it is difficult to reach a conclusion on the variations of reported heat flow from the actual heat flow of the regions. But in this work, I have determined the thermal conductivity and some other thermal and physical properties of the area in order to characterize the rocks and their influence for geothermal energy prospect in the area.

Table 2. Thermal Conductivity, Density and Porosity values from IKGWS rock samples

	Quartzite			Gneiss				Granite		
	IKGL1	**IKGL1**	**IKGL1**	**IKGL1**	**IKGL2**	**IKGL2**	**IKGL2**	**IKGL3**	**IKGL3**	**IKGL3**
Thermal Conductivity	3.22	3.89	4.02	4.11	3.65	3.04	2.95	2.98	3.42	3.62
Porosity	1.12	1.15	1.01	0.91	0.35	0.21	0.25	0.4	0.5	0.25
Density	2.8	2.81	2.85	2.79	2.68	2.85	2.75	2.7	2.67	2.72

Rock Type	**N**	**Thermal Conductivity Wm^{-1}K^{-1}**			**Density gcm^{-1}**			**Porosity %**		
		Range	Average	SD	Range	Average	SD	Range	Average	SD
Quartzite	4	3.22-4.11	3.81	0.4	2.79-2.85	2.81	0.03	0.91-1.15	1.05	0.11
Gneiss	3	2.95-3.65	3.21	0.38	2.68-2.85	2.76	0.09	0.21-0.35	0.27	0.07
Granite	3	2.98-3.62	3.34	0.33	2.67-2.72	2.7	0.03	0.25-0.5	0.38	0.13

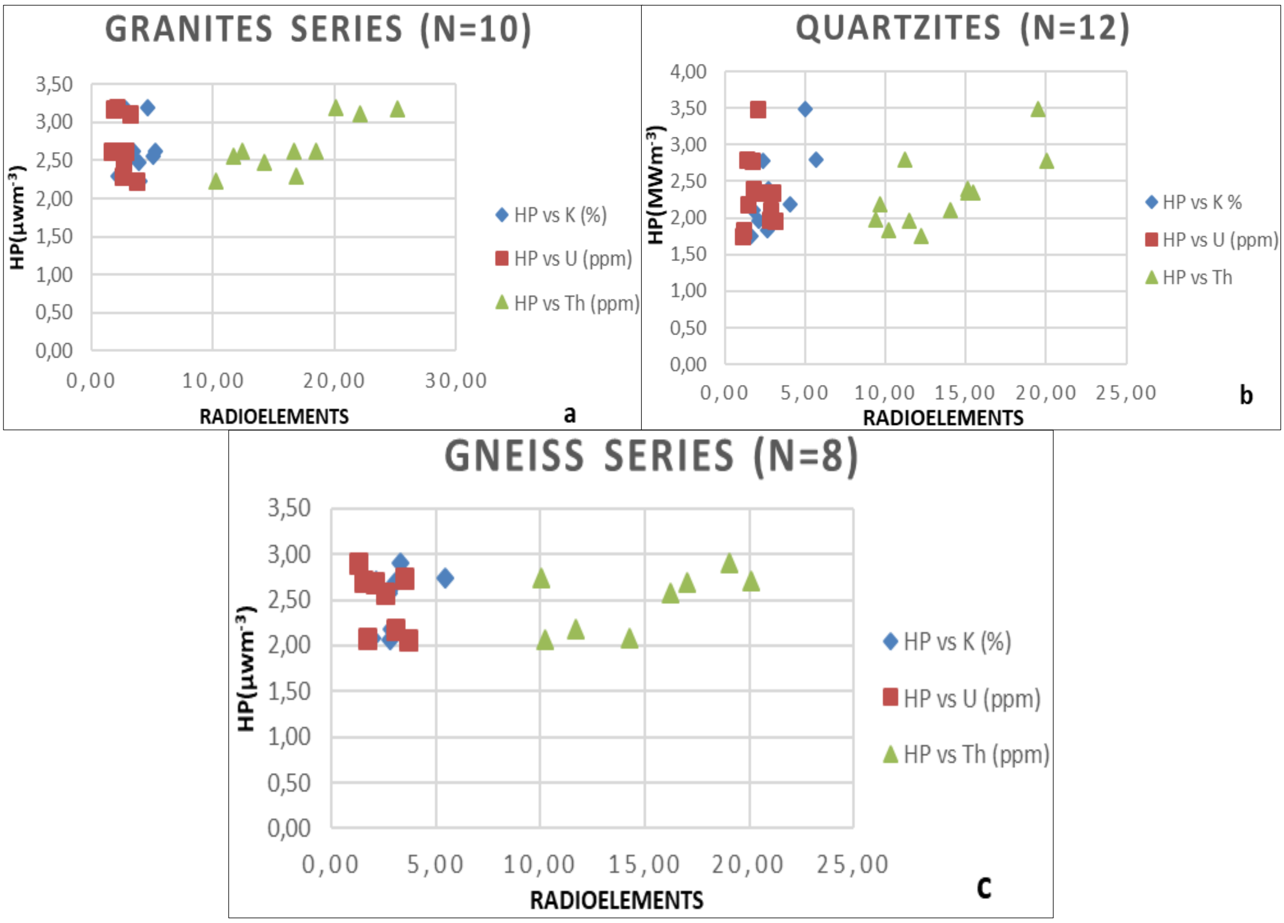

Figure 3. Heat Production vs radioelements distribution in a: Granite series; b: Quartzite series; c: Gneiss series of IKGWS

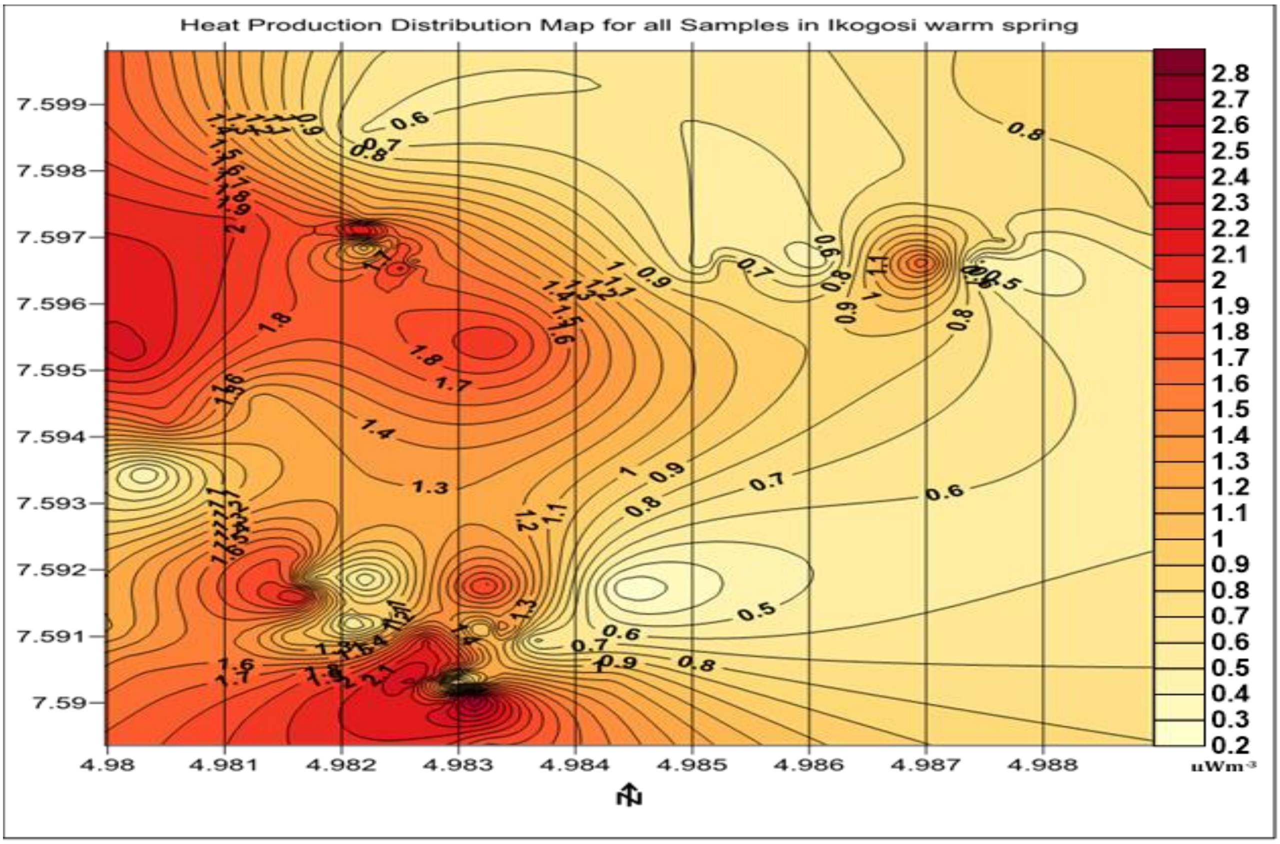

Figure 4. Radiogenic Heat Production Distribution Contour map for all samples in IKGWS

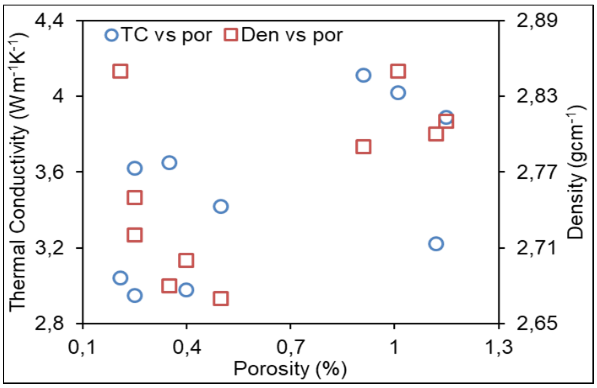

Figure 5. Distribution plot of Thermal conductivity, porosity and Density of all rocks

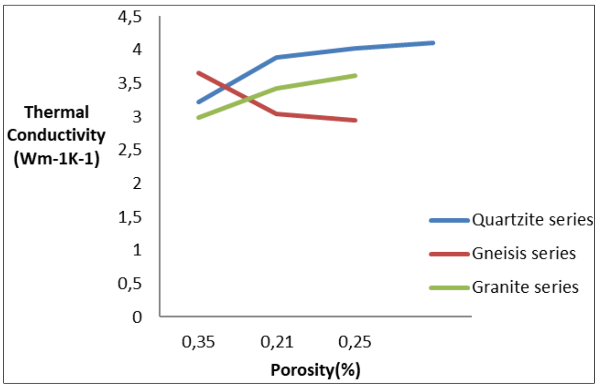

Figure 7. Distribution of each rock series from Thermal conductivity and Porosity

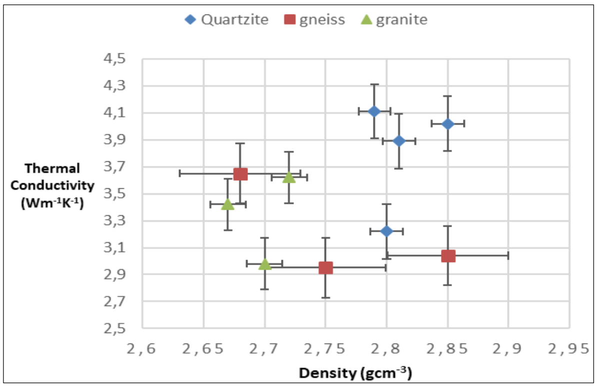

Figure 6. Bivariate plot showing Mean Thermal conductivity and Density of all rocks with SE

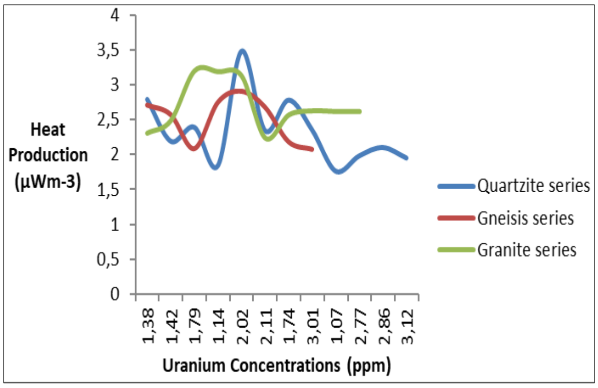

Figure 8. Contribution of Uranium concentration to RHP of each rock series

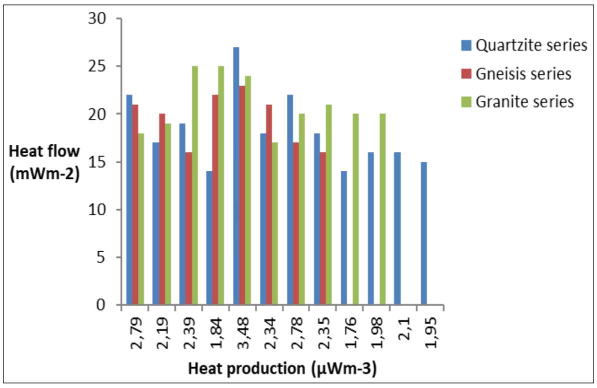

Figure 9. Heat flow and RHP distribution of each rock series

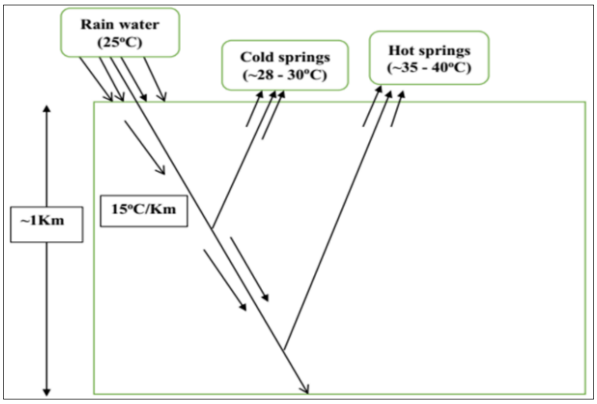

Figure 10. Typical activities of hydrothermal model of IKGWS

Meanwhile there is no defined data for heat flow in the southwestern part of Nigeria so I computed heat flow by using the measured thermal conductivity of comparable rocks in IKGWS area and compared the average heat flow and heat production values of IKGWS (27 mWm^{-2} and 3.3 μWm^{-3} respectively) with other geothermal potential regions of the world like Tattapani, India which is of the order of 290± 50 mWm^{-2} (Shanker et al., 1987, 1991; Ozdemir et al., 2017; Ozdemir and Palabiyik, 2019). The deviation in value is obvious which makes the IKGWS area far less in potential for geothermal energy exploration. The maximum heat flow computed in the crustal areas of the Indian shield is in the order of 75 ± 15 mWm^{-2}. Therefore, it is proven that the Tattapani geothermal variance and anomaly is a very robust one and could be higher than it appears at the moment. However, we cannot conclude that the IKGWS area is strong for geothermal anomalies since there have been no comprehensive research that can ascertain and characterize its geothermal potential perfectly. So, well logging or Borehole techniques, Magnetotellurics (MT) should be carried out and more rocks samples analyzed within the region.

If the water is not juvenile but meteoritic then the observed temperature can be obtained by the following procedure. If surface temperature is between 20-30 °C and rainwater/surface water go to the subsurface up to 1 km with normal gradient (~15 mK/m), then temperature attained by water will be between 35 to 45 °C. When this water comes up through some fault/fracture, it can provide a temperature of ~30-40 °C. When the water comes up by some fracture after going few hundred meters then temperature will be lower than the temperature above. The temperature will depend on the depth of penetration of the water in the sub-surface (Figure 10).

4. CONCLUSIONS

The radiometric survey showed the distribution of radio-nuclides and heat production in rocks. The radiogenic heat production study revealed that the contribution of heat from the different rock samples is dependent on the type of rocks (results from the radioactive decay of U238, Th232, and K40). The quartzite series contributes the highest followed by the granites and gneiss series. Since most of these rock samples were collected from surface outcrops, there is an uncertainty about the concentration of the radioactive elements with depth. The heat production value varied between 0.21 and 3.3 μWm^{-3}. The thermal conductivity results also indicated varied widely from 2.41 to 5.07 Wm^{-1}K^{-1} which implies a heterogeneous characteristic of the subsurface. This thermal conductivity of rocks is basically controlled by chemical composition of the rocks samples. The distribution of temperature within the earth is mainly controlled by the thermal conductivity and heat production of the geological material. The heat flow value estimated for IKGWS is 27 mWm^{-2}. This falls within the range of the regional value of 30-40 mWm^{-2} but the best method to arrive at a good value is through well logging of the area. This possibly could have affected the value for the heat production which is moderately low compared with regional heat production of Nigeria which varied between 4.0 and 4.8 μW/m^3. Therefore, from the approach of thermal assessment, the region is made of diverse rocks with huge inconsistency in thermal properties.

Clearly, no comprehensive deductions can be made from limited measurements as done in this work so it is essential to get more data from other geophysical techniques like well logging in IKGWS area to get a precise geothermal prospective assessment of the area. This will also give a perfect indication to the mechanism of heat flow and geothermal potential in the area.

Author Contributions

Samuel Sedara: Conceptualization, Methodology, Software, Data curation, Writing- Reviewing and Editing.

Conflicts of Interest

The authors declare no conflict of interest.

REFERENCES

Abraham, E.M., & Alile, O.M. (2019). Modelling subsurface geologic structures at the Ikogosi geothermal field, southwestern Nigeria, using gravity, magnetics and seismic interferometry techniques. *Journal of Geophysics and Engineering*, 16(4), 729-741.

Abraham, E.M., Lawal, K.M., Ekwe, A.C., Alile, O., Murana, K.A., & Lawal, A.A. (2014). Spectral analysis of aeromagnetic data for geothermal energy investigation of Ikogosi Warm Spring-Ekiti State, southwestern Nigeria. *Geothermal Energy*, 2(1), 1-21.

Abubakar, A.J.A., Hashim, M., Pour, A.B., & Shehu, K. (2017). A review of geothermal mapping techniques using remotely sensed data. *Science World Journal*, 12(4), 72-82.

Adegbuyi, O., Ajayi, O.S., & Odeyemi, I.B. (1996). Prospects of hot-dry-rock (HDR) geothermal energy spectrophotoresource around the Ikogosi warm spring in Ekiti state, Nigeria. *J. Renew. Energy*, 4, 58-64.

Adepelumi, A.A., Ako, B.D., Ajayi, T.R., Olorunfemi, A. O., Awoyemi, M.O., & Falebita, D.E. (2008). Integrated geophysical mapping of the Ifewara transcurrent fault system, Nigeria. *Journal of African Earth Sciences*, 52(4-5), 161-166.

Beardsmore, G.R., & Cull, J.P. (2001). Crustal heat flow: a guide to measurement and modelling. Cambridge university press.

Birch, F. (1954). Heat from radioactivity. *Nuclear geology*, 148, 174.

Brigaud, F., Lucazeau, F., Ly, S., & Sauvage, J.F. (1985). Heat flow from the West African shield. *Geophysical Research Letters*, 12(9), 549-552.

Chopra, N., Ray, L., Dey, S., & Mitra, A. (2020). Thermal conductivity, density, petrological and geochemical characteristics of granitoids from Singhbhum Craton, eastern India. *Geothermics*, 87, 101855.

Espinosa-Cardeña, J.M., & Campos-Enriquez, J.O. (2008). Curie point depth from spectral analysis of aeromagnetic data from Cerro Prieto geothermal area, Baja California, México. *Journal of Volcanology and Geothermal Research*, 176(4), 601-609.

Faweya, E.B. (2008). Radiogenic heat production in pebble from rocks in Ekiti State, Nigeria. *Journal. Fiz. Malaysia*, 29(1&2), 21-24.

Gao, P., Zhang, Y., Yu, Z., Fang, J., & Zhang, Q. (2015). Correlation study of shallow layer rock and soil thermal physical tests in laboratory and field. *Geothermics*, 53, 508-516.

Huenges, E., & Ledru, P. (2011). Geothermal energy systems: exploration, development, and utilization. *John Wiley & Sons*.

Liu, S., & Currie, C.A. (2016). Farallon plate dynamics prior to the Laramide orogeny: Numerical models of flat subduction. *Tectonophysics*, 666, 33-47.

McKenzie, D., & Priestley, K. (2016). Speculations on the formation of cratons and cratonic basins. *Earth and Planetary Science Letters*, 435, 94-104.

Ojo, J.S., Olorunfemi, M.O., & Falebita, D.E. (2011). An appraisal of the geologic structure beneath the Ikogosi warm spring in south-western Nigeria using integrated surface geophysical methods. *Earth Sciences Research Journal*, 15(1), 27-34.

Olorunfemi, M.O., Adepelumi, A.A., Falebita, D.E., & Alao, O.A. (2013). Crustal thermal regime of Ikogosi warm spring, Nigeria inferred from aeromagnetic data. *Arabian Journal of Geosciences*, 6(5), 1657-1667.

Ozdemir, A., & Palabiyik, Y. (2019). A new method for geological interpretation of 3D MT (Magnetotelluric) depth maps of high-temperature and deep geothermal fields: A case study from Western Turkey. *In 2nd International Congress on Applied Sciences*, 28-30 October 2019, Ankara, Turkey (Vol. 28, p. 30).

Ozdemir, A., Palabiyik, Y., & Arabaci, F. (2021). Geological structure and geothermal potential of the southeastern Alaşehir, Gediz Graben (western Anatolia, Turkey). *International Journal of Earth Sciences Knowledge and Applications*, 3(3), 190-207.

Ozdemir, A., Yasar, E., & Çevik, G. (2017). An importance of the geological investigations in Kavaklıdere geothermal field (Turkey). *Geomechanics and Geophysics for Geo-Energy and Geo-Resources*, 3(1), 29-49.

Ozgener, O., & Kocer, G. (2004). Geothermal heating applications. *Energy Sources*, 26(4), 353-360.

Popov, Y., Beardsmore, G., Clauser, C., & Roy, S. (2016). ISRM suggested methods for determining thermal properties of rocks from laboratory tests at atmospheric pressure. *Rock Mechanics and Rock Engineering*, 49(10), 4179-4207.

Popov, Y. A., Pribnow, D.F., Sass, J.H., Williams, C.F., & Burkhardt, H. (1999). Characterization of rock thermal conductivity by high-resolution optical scanning. *Geothermics*, 28(2), 253-276.

Salawu, N. B., Fatoba, J.O., Adebiyi, L.S., Eluwole, A.B., Olasunkanmi, N.K., Orosun, M.M., & Dada, S.S. (2021). Structural geometry of Ikogosi warm spring, southwestern Nigeria: Evidence from aeromagnetic and remote sensing interpretation. *Geomechanics and Geophysics for Geo-Energy and Geo-Resources*, 7(2), 1-16.

Sedara, S.O. (2020). Modeling Heat flow from Radiogenic Heat properties of some common rock samples and its significance to geothermal modeling. *Science & Technology*, 6(22), 71-82.

Sedara S.O., & Alabi O.O. (2021) Geothermal prospect scaling of Ikogosi warm spring using combined geophysical methods. *The Journal of Indian Geophysical Union*, 25(5), 55-70.

Shanker, R., Guha, S.K., Seth, N.N., Mathuraman, K., Pitale, U.L., Jangi B.L., Prakash, G., Bandyopadhyay, A.K., & Sinha, R.K. (1991) Geothermal Atlas of India. *Geological Survey of India special publication*, 19, 144.

Shanker, R., Thussu, J.L., & Prasad, J.M. (1987). Geothermal studies at Tattapani hot spring area, Sarguja district, central India. *Geothermics*, 16(1), 61-76.

Turcotte, D.L., & Schubert, S. (2002) Geodynamics John Wiley and Sons, Cambridge university press.

Verheijen, P.J.T., & Ajakaiye, D.E. (1979). Heat-flow measurements in the Ririwai ring complex, Nigeria. *Tectonophysics*, 54(1-2), 27-32.

Zhu, W., Su, X., & Liu, Q. (2021). Analysis of the relationships between the thermophysical properties of rocks in the Dandong Area of China. *European Journal of Remote Sensing*, 54(2), 122-131.